2015

DETERMINATION OF EXPLOSIVE ENERGY PARTITION VALUES IN ROCK BLASTING THROUGH SMALL-SCALE TESTING

Joshua Calnan
University of Kentucky, josh.calnan@gmail.com

STUDENT AGREEMENT:

I represent that my thesis or dissertation and abstract are my original work. Proper attribution has been given to all outside sources. I understand that I am solely responsible for obtaining any needed copyright permissions. I have obtained needed written permission statement(s) from the owner(s) of each third-party copyrighted matter to be included in my work, allowing electronic distribution (if such use is not permitted by the fair use doctrine) which will be submitted to UKnowledge as Additional File.

I hereby grant to The University of Kentucky and its agents the irrevocable, non-exclusive, and royalty-free license to archive and make accessible my work in whole or in part in all forms of media, now or hereafter known. I agree that the document mentioned above may be made available immediately for worldwide access unless an embargo applies.

I retain all other ownership rights to the copyright of my work. I also retain the right to use in future works (such as articles or books) all or part of my work. I understand that I am free to register the copyright to my work.

REVIEW, APPROVAL AND ACCEPTANCE

The document mentioned above has been reviewed and accepted by the student's advisor, on behalf of the advisory committee, and by the Director of Graduate Studies (DGS), on behalf of the program; we verify that this is the final, approved version of the student's thesis including all changes required by the advisory committee. The undersigned agree to abide by the statements above.

Joshua Calnan, Student

Dr. Braden T. Lusk, Major Professor

Dr. Braden T. Lusk, Director of Graduate Studies

DETERMINATION OF EXPLOSIVE ENERGY PARTITION VALUES IN ROCK BLASTING THROUGH SMALL-SCALE TESTING

DISSERTATION

A dissertation submitted in partial fulfillment of the
requirements for the degree of Doctor of Philosophy in the
College of Engineering
at the University of Kentucky

By

Joshua Thomas Calnan

Lexington, Kentucky

Director: Dr. Braden T. Lusk, Professor of Mining Engineering

Lexington, Kentucky

2015

ABSTRACT OF DISSERTATION

DETERMINATION OF EXPLOSIVE ENERGY PARTITION VALUES IN ROCK BLASTING THROUGH SMALL-SCALE TESTING

Blasting is a critical part of most mining operations. The primary function of blasting is to fragment and move rock. For decades, attempts have been made at increasing the efficiency of blasting to reduce costs and increase production. Most of these attempts involve trial and error techniques that focus on changing a single output. These techniques are costly and time consuming and it has been shown that as one output is optimized other outputs move away from their optimum level. To truly optimize a blasting program, the transfer of explosive energy into individual components must be quantified. Explosive energy is broken down into five primary components: rock fragmentation, heave, ground vibration, air blast, and heat. Fragmentation and heave are considered beneficial components while the remaining are considered waste. Past energy partitioning research has been able to account for less than 30% of a blast's total explosive energy.

The purpose of this dissertation was to account for a greater percentage of the explosive energy available during a blast. These values were determined using measurement techniques not previously applied to energy partitioning research. Four small-scale test series were completed, each designed to isolate individual energy components. Specific energy components measured include borehole chambering, elastic deformation (ground vibration), translational and rotational kinetic energy (heave), and air overpressure (air blast).

This research was able to account for 73% of the total explosive energy. Borehole chambering (13%), rotational kinetic energy (25%), translational kinetic energy (5%), and air overpressure (28%) were determined to be the largest components. Prior research efforts have largely ignored rotational kinetic energy and have only been able to offer predictions for the values of borehole chambering and air overpressure energies.

This dissertation accounted for a significantly higher percentage of total available explosive energy than previous research efforts using novel

measurement techniques. It was shown that borehole chambering, heave, and air blast are the largest energy components in a blast. In addition to quantifying specific energy partitions, a basic goal programming objective function was proposed, incorporating explosive energy partitioning and blasting parameters into a framework that can be used for future energy optimization.

KEYWORDS: Rock Blasting, Energy Partitioning, Optimization, Explosives, Goal Programming

Joshua Thomas Calnan

12/11/2015

DETERMINATION OF EXPLOSIVE ENERGY PARTITION VALUES IN ROCK BLASTING THROUGH SMALL-SCALE TESTING

By

Joshua Thomas Calnan

Dr. Braden T. Lusk
Director of Dissertation

Dr. Braden T. Lusk
Director of Graduate Studies

12/11/2015

Acknowledgements

I would like to thank my wife, Courtney, for her love, support, and patience throughout this process. Without her encouragement I would not have made it through this process. Thank you to parents, Cori and Tom, for their continued support, emotionally and financially, through all of these years of college. I would also like to thank my brothers, Todd and Adam, for providing their sarcastic comedic relief when I needed it most. A big thanks goes to my grandparents, Roger and Ann, and Tom and Doris, for their phone calls to see how things were going and to offer words of encouragement.

Thank you to all of the members of the University of Kentucky Explosives Research Team (UKERT), especially Paul Sainato, Brendan McCray, Lizzie Maher, and Kylie Larson-Robl. Without the long hours that they put in helping me, my research would never have gotten done.

I would like to thank the facility and stuff of the University of Kentucky Mining Engineering Department, especially Ed Thompson and Megan Doyle for lending a helping hand over the past few years.

Finally, I would like to thank my advisor, Dr. Braden Lusk, and the rest of my dissertation committee, Dr. Kyle Perry, Dr. Jhon Silva, Dr. Chad Wedding, and Dr. Sebastian Bryson. Their knowledge and support was vital to the completion of this dissertation.

TABLE OF CONTENTS

LIST OF TABLES

LIST OF FIGURES

Chapter 1. Introduction

For decades the mining industry has worked to increase efficiency in blasting applications, commonly through costly and time consuming methods. As computer modeling technology has advanced, some guesswork has been removed from the trial and error fieldwork and is instead completed in the office by varying blast design parameters in a computer model until the results resemble what is considered acceptable blast performance. This approach is often less expensive and less time consuming, but the results must still be validated and refined in the field.

Many times these trial and error processes seek to modify one output, usually rock fragmentation in production environments and vibration in urban areas. Drilling and blasting costs are also a major decision making factor. It is a long standing problem that when modifying a blast design to optimize an output, the other outputs move away from their optimum point. For example, when trying to increase fragmentation, other factors such as ground vibration, air blast, and cost generally increase and can reach unacceptable levels.

To truly begin to optimize a blast design, the use of explosive energy must be understood. Explosive energy is transferred into five primary components during blasting: fragmentation, heave, air blast, ground vibration, and heat (Sanchidrian et al., 2007; Lusk, 2014). This concept is represented in Figure 1.1. A blasting engineers' goal is to maximize explosive energy utilization in fragmentation and rock movement (heave) and minimize energy loss to air blast, ground vibration,

and heat. Optimizing explosive energy use will result in better performing blasts (i.e. increased fragmentation and acceptable air blast), in addition to cost reduction and increased profits.

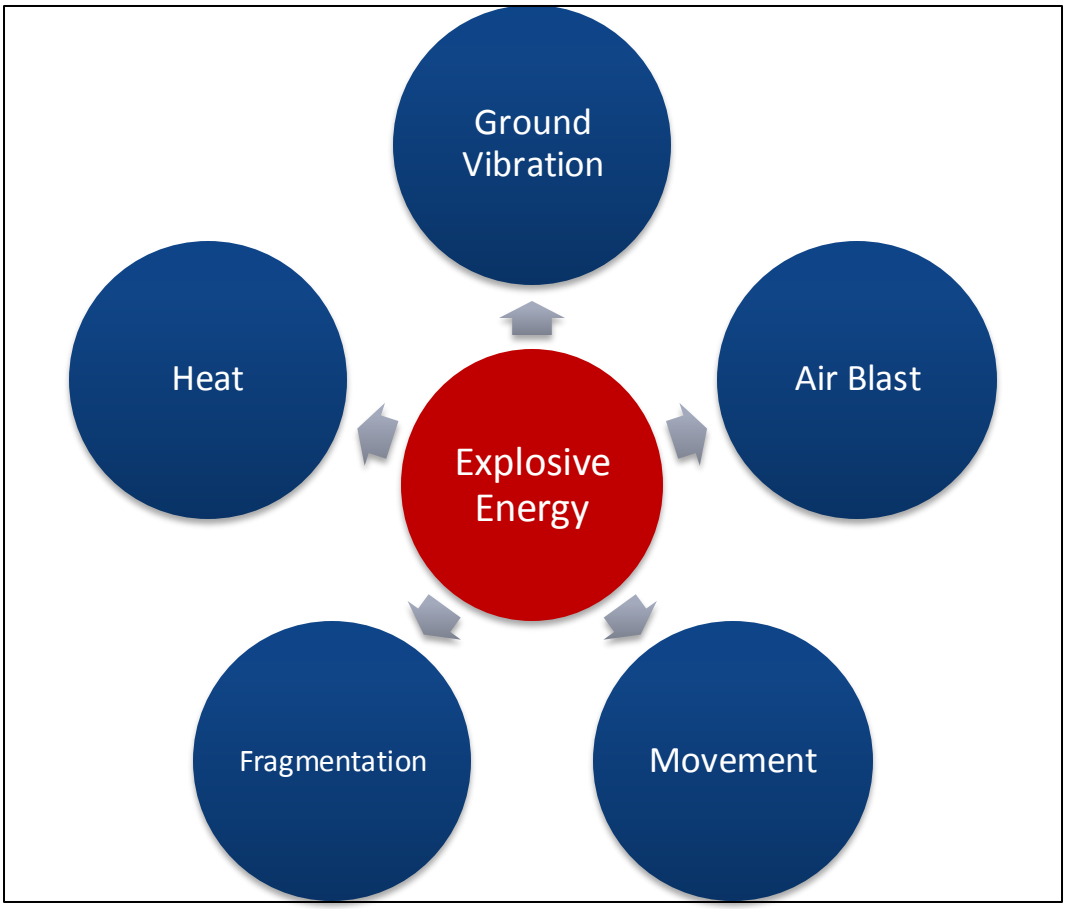

Figure 1.1: Explosive Energy Components

Although explosive energy partitioning has been studied in the past (Berta, 1990; Spathis, 1999; Ouchterlony et al., 2003; Sanchidrian et al., 2007) a significant portion of the total explosive energy has not been accounted for. These past studies have examined full-scale blasts, relying primarily on traditional blast instrumentation equipment such as seismographs which, although ideal for documenting a blast for regulatory compliance, are not well suited for a refined

assessment of explosive energy components. Components such as rotational kinetic energy, air blast, and permanent deformation of the borehole have largely been ignored during these past research efforts.

The problem of optimizing one output or goal without adversely affecting other variables is not limited to the explosives industry. In fact, this problem can be found in almost every industry. To deal with this problem, a form of computer programming was developed called goal programming. Goal programming (GP) is a programming technique used to find an optimum solution for complex problems containing many variables and conflicting objectives.

The primary focus of the research presented in this dissertation is to examine each of the explosive energy components more closely, with the goal of accounting for greater portions of the total explosive energy. This is accomplished through a number of small-scale test series designed to isolate specific components, using laboratory equipment better suited to collect data at the necessary level of fidelity. This dissertation also introduces the concept of using goal programming as a means of explosive energy optimization in the rock blasting environment.

Chapter 2. Review of Literature

2.1 Introduction to Blasting and Key Terms

The primary function of blasting is to fragment and move rock so that it can be efficiently handled by equipment such as loaders, shovels, haul trucks, etc. Good blasting practices effectively fragment and move rock while also limiting ground vibration, air overpressure, fly rock, and toxic gas emissions. The blasting program must maintain production rates and remain cost effective.

Fragmentation requirements vary from mine to mine based on haulage equipment and use of the blasted material. In the Appalachian Region, blasted overburden is typically hauled to dump sites via haul truck to be used as fill for reclamation activities. Other effects, including cost and environmental impact, must also be considered (Johnson et al., 2013).

Since this dissertation will focus heavily on blast design and variation of parameters, a brief overview of key terms and general blasting guidelines is provided.

One of the most critical terms to understand in blasting is powder factor. Powder factor is a ratio of the amount of explosives used to break a given amount of rock. The definition of powder factor varies based on the function the explosive serves.

When mining ore, the definition of powder factor is given as:

$$PF = \frac{lb\ of\ explosive}{tons\ of\ ore} \tag{2.1}$$

When removing waste rock (overburden) powder factor is defined as:

$$PF = \frac{lb\ of\ explosive}{cubic\ yards\ of\ rock} \tag{2.2}$$

For the remainder of this dissertation, the second definition of powder factor will be used. Other key terms are defined below and in Figure 2.5.

Face Height (L) – the height of the free face.

Burden (B) – the distance from a row of holes to the free face. This is the amount of material that must be moved by a row of loaded holes.

Spacing (S) – the distance between holes in a row.

Hole Depth (H) – the depth of the hole below the surface, including subdrill (J).

Stemming Height (T) – the amount of material, usually drill cuttings or gravel, placed in the borehole to contain the explosive energy.

Powder Column (PC) – the height of the explosive column within the borehole. The powder column is generally the face height + subdrill depth – stemming height.

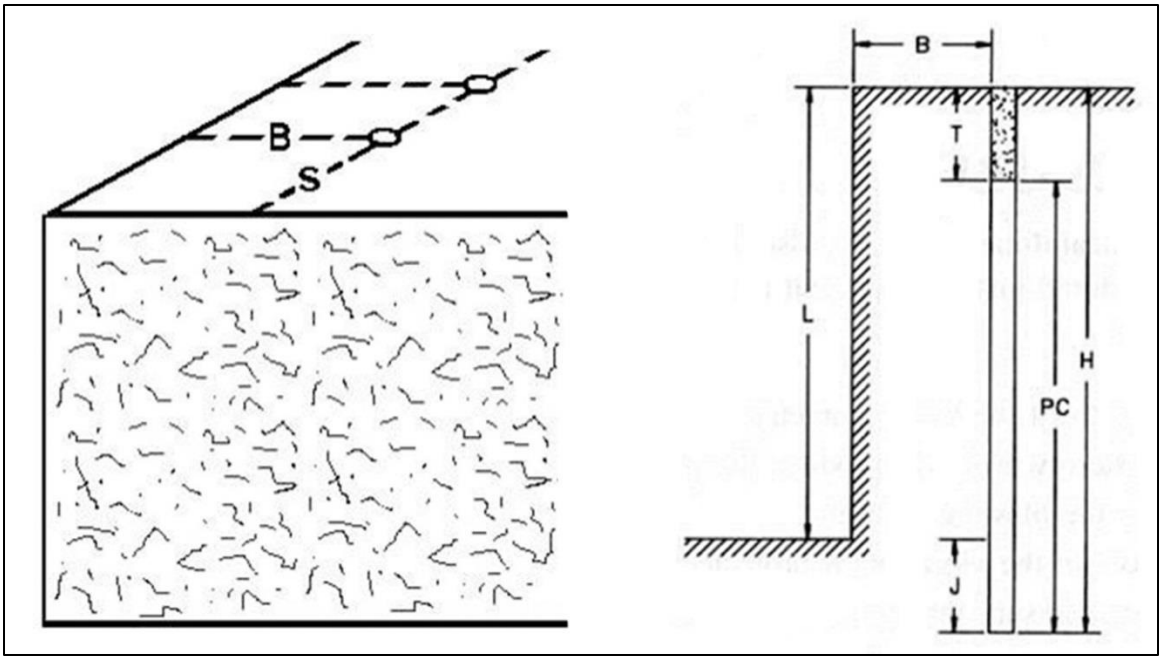

Figure 2.1: Key blasting parameters (Lusk, 2011)

Boreholes are typical laid out on one of three patterns; square, rectangular, and staggered. These patterns are illustrated in Figure 2.6. Square patterns have equal burden and spacing while in a rectangular pattern the spacing is generally greater than the burden. In a staggered pattern, each row of holes is offset relative to the row of holes in front of it.

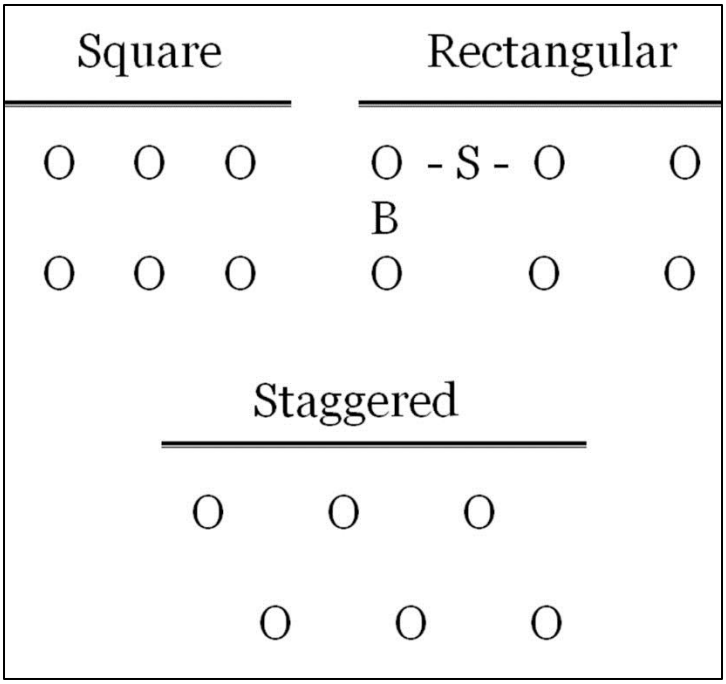

Figure 2.2: Typical hole pattern layouts (Lusk, 2011)

2.1.1 General Blasting Guidelines

The first step in any basic blast design is determining the desired powder factor. A good starting point for bench blasting in most surface mining applications is 1 lb/yd^3. The powder factor varies based on site specific geological conditions and fragmentation needs. Factors such as joints, discontinuities, voids, weathering, and rock strength must be taken into account. A higher powder factor typically results in smaller, more uniform rock fragments and increased heave. Figure 2.7 presents typical powder factor ranges based on application.

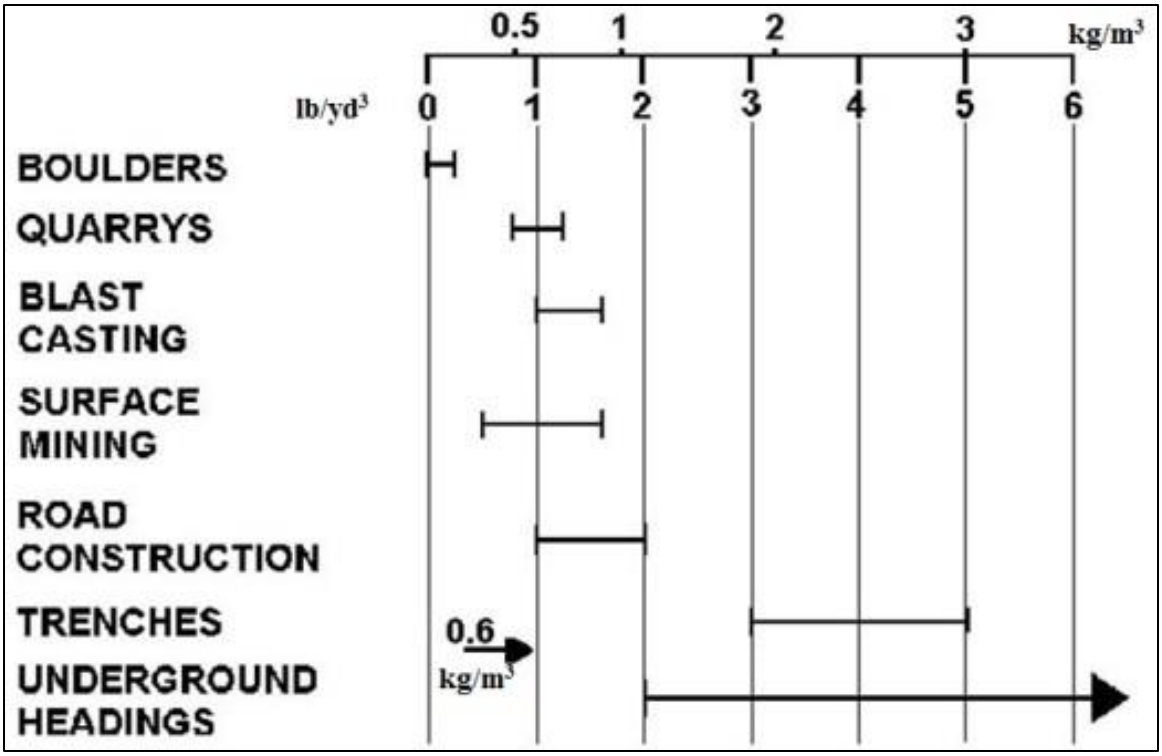

Figure 2.3: Typical powder factor ranges based on application (Lusk, 2011)

Ash's Burden Factor Equation (2.3) is used as a starting point to determine the optimal burden, taking into account the type of explosive being used and the density of the rock being blasted.

$$K_B = 30(SG_{ex}/1.4)^{1/3}(160/Wt_{rk})^{1/3} \tag{2.3}$$

$$SG_{ex} = Specific\ gravity\ of\ explosive\ (\frac{g}{cc}) \tag{2.4}$$

$$Wt_{rk} = Unit\ weight\ of\ rock\ (\frac{lb}{cubic\ ft}) \tag{2.5}$$

After determining the burden factor (K_B), the burden is calculated using the diameter of the explosive (d_x). For packaged products, the diameter of the explosive is the diameter of the package, and for bulk products, such as

ammonium nitrate/fuel oil (ANFO), the diameter is taken as the diameter of the borehole.

$$B = d_x \times K_B \quad (2.6)$$

Ash's Spacing Relationship serves as a guideline for determining the hole to hole spacing of a pattern in relation to the burden.

$$S = B \times (1.4\ to\ 2) \quad (2.7)$$

As a generalized rule of thumb, when utilizing ANFO as the explosive product, it can be assumed that:

$$B = 24 \times hole\ diamter \quad (2.8)$$

$$S = 36 \times hole\ diamter \quad (2.9)$$

Emulsions and emulsion/ANFO blends have a higher specific gravity than ANFO and therefore do not require as tight of a pattern to achieve the required powder factor. As a result, the generalized rule of thumb for burden and spacing when using these products is:

$$B = 30 \times hole\ diamter \quad (2.10)$$

$$S = 42 \times hole\ diamter \quad (2.11)$$

A general rule of thumb for determining face height is 100 to 120 times the hole diameter.

Scaled distance must be taken into account when determining the maximum amount of explosives that can be detonated within a single delay period. This is done in an effort to limit ground vibrations that could cause damage to nearby structures. Table 2.1 summarizes the scaled distance equations based on distance from the blasting site to the nearest structure. As shown in this table,

the scaled distance equation varies based on distance and becomes more stringent as distance increases. The primary reason for this is that as blast induced ground vibrations travel through the earth their frequency decreases. Built structures have a low resonance frequency and are more susceptible to damage caused by these lower frequency ground vibrations.

Table 2.1: Scaled Distance Equations (adapted from Lusk, 2011)

Distance (D) from the blasting site in feet	Scaled Distance Equation
0 to 300	$W = \left({}^{D}/_{50}\right)^2$
301 to 5,000	$W = \left({}^{D}/_{55}\right)^2$
5,001+	$W = \left({}^{D}/_{60}\right)^2$
W = the maximum weight of explosives that can be detonated within any eight (8) millisecond period.	
D = the distance, in feet, from the blasting site	

2.2 Energy Partitioning

Explosive energy is transformed into five primary components in a rock blasting environment. Two of these components, kinetic energy (rock movement) and fracture energy (fragmentation) are beneficial, while explosive energy transferred to seismic energy (ground vibration), air blast, and heat can be considered waste.

Extensive work has been completed in recent years in an attempt to better understand energy partitioning. Spathis (1999) calculated the amount of energy being transformed into kinetic energy, fracture energy, and seismic energy. He also recommended the use of energy balance in blast designs to increase efficiency as future work. The idea of energy balance involves optimizing the use

of the explosive energy available to achieve desirable results, rather than simply increasing the total amount of explosive energy. Ouchterlony et. al. (2003 and 2004), and Sanchidrian et al., (2007) have also conducted work similar to that of Spathis (1999). Their works will be discussed in more detail throughout this chapter.

While a significant amount of information has been uncovered through these publications, many questions are left unanswered. One of the largest obstacles is the number of variables that must be considered in an experiment. Below are examples of some of the components where energy is absorbed in the blasting process. By no means is this list complete, but it serves as a useful starting point (Berta, 1990; Lusk, 2014; Ouchterlony et al., 2004; Sanchidrian et al., 2007; Spathis, 1999).

Immediately In and Around Borehole

- Chambering of the borehole
- Crushing (fines)
- Friction
- Heat

In the Surrounding Rock Mass

- Elastic and Plastic Deformation from tensile and compression forces
- Micro-cracks
- Macro-cracks
- Formation of large fragments (greater than 1mm)
- Formation of fines (smaller than 1mm)
- Backbreak
- Friction and impact between fragments
- Movement of fragments

Lost into the atmosphere (outside immediate blasting zone)

- Heat
- Fumes
- Airblast
- Ground Vibration

Fracture and kinetic energies are relatively easy to measure because the end result can be seen through rock fragmentation and movement. However, energy transferred into elastic and plastic deformation of the rock, heat transfer to the rock, and enthalpy of the venting gases are not as easily measured (Sanchidrian et al., 2007).

Sanchidrian et al. (2007) conducted extensive work in an attempt to quantify the energy components in rock blasting. In doing so, a number of useful equations were identified. The first equation, and likely the most important, is the energy balance equation expressed as:

$$E_E = E_F + E_S + E_K + E_{NM} \tag{2.12}$$

where E_E is the explosive energy, E_F is the fragmentation energy, E_S is the seismic energy, E_K is the kinetic energy, and E_{NM} is energy forms not measured such as air blast and heat.

Fragmentation energy can be calculated using the equation:

$$E_F = A_F G_F \tag{2.13}$$

where G_F is the specific fracture energy calculated from experimental fragmentation tests and A_F is the surface area of the fragments created by the

blast. The surface area of the fragments can be approximated based on the muckpile size distribution using the simplified equation:

$$A = 6V \int_0^\infty \frac{f(x)}{x} dx \tag{2.14}$$

where x is the diameter or edge length of the particles, V is the volume of the fragmented rock, and $f(x)$ is the density function of the fragment size distribution.

The calculation of seismic energy is more complicated and requires a number of approximations and before finally reaching the following equation:

$$E_S = 4\pi r^2 \rho c_L \int_0^\infty v^2 dt \tag{2.15}$$

where r is the radius of the surface across which the total power is acting, ρ is the rock density, c_L is the longitudinal wave velocity, v is the magnitude of the vector sum of the velocities using a unique wave velocity.

The kinetic energy of rock displaced by a blast hole is given as:

$$E_K = \frac{1}{2} S B_h \int_0^H \rho(y) V_0^2(y) dy \tag{2.16}$$

where S is the spacing between holes, B_h is the burden, H is the bench height, $\rho(y)$ is the rock density (taking into account the variability throughout the height of the profile), and $V_0(y)$ is initial velocity of the rock face at different heights.

2.2.1 Explosive Energy Determination

There is no universally accepted way to assess explosive energy. Explosive energy determination can be separated into two categories: experimental testing, and thermodynamic detonation code modeling. Each method has its own intrinsic flaws.

The two most commonly utilized experimental tests are the cylinder test and the underwater test. During cylinder tests, a copper cylinder is packed with an explosive charge. Upon detonation, the velocity of the fragments are calculated and equated to useful work using the Gurney equation (Gurney, 1943; Nyberg et al., 2003). This test is particularily useful for energy determination related to munitions and to some extent energy transferred to a borehole, but it fails to fully capture the energy lost to heat and gas formation. The underwater test also has its own flaws. During these tests, an explosive charge is detonated underwater, resulting in a rapidly expanding gas bubble. The bubble expands until the pressure within falls below the equilibrium hydrostatic pressure of the surrounding water. The bubble then collapses until the pressure again rises above the equilibrium hydrostatic pressure. This process repeats until the gases vent to the atmosphere. The time between the initial expansion and the subsequent collapse is used to determine the explosive energy. The primary concern with this test methodology is that it fails to take into account the effects of confinement on the explosive (Mohanty, 1999).

A number of ideal detonation codes are commercially available for explosive energy modeling. In the work highlighted by Sanchidrian (2007), the W-Detcom code is used. Other thermodynamic codes include CHEETAH and its predecessor, TIGER (both developed by Lawrence Livermore National Laboratory). These codes predict the velocity of detonation and heat of detonation assuming an ideal, complete detonation of the product. For high explosives (i.e. PETN and RDX), the experimental values generally agree with the predicted values. However, for many commercial explosives (i.e. ANFO and emulsions), the predicted values are higher than the experimental values because the product does not detonate ideally. Partial reaction models are being implemented into thermodynamic code. In these models, the assumption is made that the explosive product is not ideally detonating. The results from these models are in better agreement with experimental results for commercial explosives (Sanchidrian and Lopez, 2006).

The advantage of using heat of detonation calculated by thermodynamic code versus useful work captured by experimental tests, is that heat of detonation fully accounts for all of the energy available during detonation, whereas experimental tests only account for a portion of the energy based on a specific detonation parameter.

2.2.2 Fragmentation Energy

Many blasting engineers view fragmentation as a simple process. The shock front caused by detonation of the explosive transmits compression waves through the rock mass until they reach the free-face where they are then

reflected, causing the pre-conditioned rock to fail in tension. The expanding gases further exploit the existing cracks and increase fragmentation. To an extent, this statement is true; however, the process is much more complex with different reaction zones, each having their own microscopic and macroscopic events taking place.

The fragmentation process is comprised of two processes taking place during the detonation of an explosive. First, the shock phase pressurizes a volume of rock, leading to the compression waves that are transmitted to the free-face before being reflected, causing the rock to fracture in tension. Next, the gas pressure caused by the detonation of the explosive increases in the borehole and is sustained until the point at which fractures open and allow for the expansion and venting of the gases.

Sellers (2013) states that in massive rock masses radial cracks are prevalent. However, in highly jointed rock masses, radial fracturing is not evident. Instead, the joints open. It is not surprising that in a massive deposit, fractures will form radiating away from the borehole, while in jointed rock, the expanding gases will exploit weaknesses already present. It is difficult to create a smaller mean particle size in highly jointed rock because the gases are able to vent through these joints rather than produce new cracks (Lusk, 2014).

Fragmentation energy can be broken down into a number of components. Not all of the fragmentation energy goes directly into creating new visible fragments. It is hypothesized that a great deal of energy is absorbed by the rock through

plastic and elastic deformation, both in compression and in tension. The exact amount of energy absorbed during this process is unknown. Most literature only considers the formation of macro-cracks, or the large cracks that lead to the formation of individual fragments. Work by Hamdi et al. (2001) introduces the idea of also considering the energy requirements for the formation of micro-cracks. Although these micro-cracks result in a very limited increase of the surface area individually, the large number of them results in a significant increase in surface area overall. Based on additional work completed by Hamdi et al. (2008), micro-cracks account for up to 11% of the explosive energy, whereas the macro-cracks account for only 6%.

Determination of the fragmentation energy is a rather intense process that requires a significant amount of pre-blast preparation. Calculation of the fragmentation energy relies solely on the amount of new surface area created within the rock. Therefore, it is critical to know the surface area of existing cracks and joints within the rock mass prior to blasting. This is completed through an extensive geological survey of the rock mass discontinuities. Joints are mapped and the block sizes and surface area calculated. After the blast, the fragment sizes are determined using image analysis software.

Fragmentation is measured using image analysis software such as Split Desktop (Split Engineering, 2001), Fragscan (Schleifer and Tessier, 2000); and WipFrag (Wipware, 2015). Each of these software packages is able to estimate the fragment size distributions by analyzing digital images of the rock in the muckpile, primary crusher hopper, or haul truck. These packages work well for

determining the size distribution of larger particles, but fall short when determining the amount of fines. Therefore, correction factors are often applied to account for the fines.

In the work completed by Hamdi et al. (2008), the fragments sizes were continually monitored as the fragments travelled along a conveyor. In a coal mining operation this is not possible, since muck is almost always transported via truck. Instead, extensive photography of the muckpile in various stages of removal is required.

After the fragmentation distribution curves have been created, the fragmentation energy can be determined using the surface area of the fragments, the volume of rock blasted, and the specific fracture energy (Sanchidrian et al.,2007).

Sanchidrian et al. (2007) uses Rittinger's law as the basis for specific energy calculations due to the large amount of fines in a blast. Rittinger's law states that the amount of energy required to mechanically crush fragments is directly proportional to the amount of new surface area created. Rittinger's law has commonly been used to calculate energy requirements for large mills, and the author is skeptical that this method is directly applicable to fragmentation energy. Sanchidrian et al. (2007) also fails to take into account the surface area of micro-cracks. The Rittinger coefficient may be applicable for calculation of the fines immediately around the borehole in the crush-zone.

Hamdi et al. (2008) utilizes Griffiths theory for the basis of his calculations. Griffiths theory is commonly associated with the fracture of brittle materials and is

used to determine the magnitude of tensile stress required to create new fractures. The equation presented by Hamdi et al. (2008) is:

$$E_{mf} = c_f DA \tag{2.17}$$

where E_{mf} is the macro-fragmentation energy, c_f is the specific fracture energy, and DA is the new blast-induced surface area.

Specific fracture energy (c_f) is a function of the fracture toughness (K_{IC}), the rock density (q), and the P-wave velocity (c). Specific fracture energy is calculated using the following formula:

$$c_f = \frac{{K_{IC}}^2}{2 * q * c^2} \tag{2.18}$$

Specific fracture energy is determined experimentally using the Wedge Splitting Test (Moser, 2003; Moser et al, 2003) or the Three-Point Bending Test (RILEM Committee FMC-50, 1985).

Back breakage is fracturing of the remaining rock mass immediately surrounding the blasted area and is not accounted for in any of these studies. Back break affects a relatively small volume of the rock mass on the backside of the blast in comparison to the blasted material. Therefore, if current results hold true (stating that fragmentation only accounts for a limited amount of energy, say 5%), then back break may be negligible and can be discounted.

2.2.3 Seismic Energy

Calculation of seismic energy is far from a simple and exact process as highlighted by Sanchidrian et al. (2007), Ouchterlony et al. (2004), and Silva (2015). To calculate seismic energy a significant number of simplifying assumptions are required to equate particle velocity to stress which is then used to calculate energy flow past a given point. To make these assumptions, wave velocities about the three primary axes (longitudinal, transverse, and vertical) must be know. This analysis is also dependent upon density of the rock material (Sanchidrian et al., 2007).

To further complicate matters, seismographs, which are commonly used to monitor ground vibrations, are not ideally suited for energy calculations. It is not uncommon for seismic energies to vary significantly from one seismograph to another (Sanchidrian et al., 2007). Ouchterlony et al. (2004) expands on this concern, stating that seismographs are ill-suited for energy calculations because content is filtered and surface mounting distorts the frequency. He recommends using triaxial accelerometers mounted in the bottom of boreholes.

2.2.4 Kinetic Energy

Kinetic energy can be calculated based on rock movement. This is done by tracking a target point as it moves using high-speed photography. The displacement and subsequent velocity can be tracked manually through a frame-by-frame visual analysis, or by using a software package such as Motion Tracker 2D (Blasting Analysis International, 2001). Once the movement of the rock is

known, the kinetic energy can be calculated using basic physics (Sanchidrian et al., 2007).

The methods for determining energy absorption in movement are based on the fact that explosive energy is converted to kinetic energy within the rock mass. However, calculations for energy lost to movement have been greatly oversimplified to this point. Current methods rely on the face velocity as a means of determining the kinetic energy of the rock mass using the classic physics equation $KE = \frac{1}{2}mv^2$. The problem with this approach is that the rock mass does not have a constant velocity from the face to the borehole. Ouchterlony et al. (2004) proposed that the velocity is highest at the face and falls to near zero at the borehole. The author strongly disagrees with this theory and believes that the velocity is nearly constant throughout the profile with slightly higher velocities at the face than near the borehole due to collisions.

Another major problem with this simplification is that inelastic collisions are constantly taking place between fragments. Although momentum is conserved in an inelastic collision, kinetic energy is not. This energy is lost to additional fragmentation, heat, friction, and sound.

Finally, only translational kinetic energy has been considered to this point. Rotational kinetic energy has largely been ignored during previous work. Based on field experience and video analysis of previous blasts, the author believes that for many typical bench blasting scenarios using short delays, rotation of fragments is small in comparison to translation of fragments. However, during

blasts utilizing slower timing, fragment rotation is prevalent and should be considered.

2.2.5 Air Blast Energy

Typically, air blast magnitude and frequency is only considered for limiting damage to nearby structures and regulatory compliance. The author could not find any instances where the portion of energy lost to air blast has been directly measured in a blasting environment. However, the energy of open air explosions has been studied significantly in the past using the principle of shock front velocity. It is most famously demonstrated by Enrico Fermi, who used falling paper carried by the blast wave to approximate the nuclear yield of the United States' first nuclear bomb at the Trinity Test in 1945. The technology used to measure the change in pressure and time of arrival has been improved since Fermi's effort, but the theory and application remain unchanged as shown in Hoffman's (2009) work. Pairs of pressure sensors mounted collinearly are used to measure the peak overpressure and shock wave velocity as it passes a given point. This data is then be used to calculate the volume of air compressed by the shock front. From this, the energy of the blast can be calculated.

2.2.6 Energy Measurement Values

In the work conducted by Sanchidrian et al. (2007), the measured energy values varied significantly. All energy values were expressed as a percentage of the total estimated explosive energy. Fracture energy accounted for 3-7%, seismic energy 1-4%, and kinetic energy 5-16%. From this, it was determined that only

8% to 26% of the explosive energy was measured. It was hypothesized that 30% of the explosive energy was lost to gasses venting to the atmosphere with the remaining 40-60% being transferred to rock deformation and heat transfer.

Ouchterlony et al. (2003) determined that 60-70% of the total explosive energy is transferred to the rock mass, with the remaining percentages transferred to the atmosphere and not performing useful work. They found that seismic energy varied from 3-12% and kinetic energy varied from 3-16%.

Hamdi (2008) states that 11% of the energy is transmitted to formation of micro-cracks and 6% is transmitted to formation of macro-cracks.

2.3 Borehole Physics and Cavity Expansion Analysis

Traditionally, energy partitioning analysis has modeled the response of rock to blasting as elastic. It has been known for some time that this model is incorrect, but no better models existed (Cunningham et al., 2007). Work by Cunningham et al. (2007) has significantly changed the way energy partitioning in blasting is viewed through the application of Cavity Expansion Analysis (CEA) and hyper-velocity penetrators to blasting.

During detonation of a borehole, permanent enlargement of the hole, (called chambering) results from the shock-driven, non-elastic deformation of the surrounding rock. This chambering effect has been documented on many occasions where the blast has failed to sufficiently create fragmentation (Cunningham et al., 2007; Szendrei and Cunningham, 2003). However, most

blasting engineers never witness this phenomenon, as a result of the complete destruction of the borehole during the blast.

To an extent, the fundamentals of blasting are not understood. There is still debate as to whether or not VoD of an explosive plays a significant role in the fragmentation and heave of the rock. It is also unknown how energy is transferred from the explosive to the rock mass immediately surrounding the borehole, as the failure mode in the rock mass varies based on whether the explosive VoD is higher or lower than the sound velocity (C_p) and shear wave velocity (C_s). It is possible that CEA may provide a means of definitively answering these questions.

2.3.1 Borehole Physics

Commercial explosives detonate in a non-ideal manner. A significant portion of the detonation reaction takes place after the Chapman-Jouguet (C-J), or sonic plane. This results in a lower detonation pressure and velocity, but a longer pressure duration in the borehole if the stemming holds and burden is competent. This detonation process can be broken down into two phases, the “Shock Energy” phase and “Heave Energy” phase. The reaction taking place ahead of the C-J plane which sustains the shock front is the Detonation Driving Zone (DDZ). The expanding reaction zone behind the C-J plane results in the shock phase of the detonation process. Chambering occurs during this stage. The borehole expands until the detonation pressure and borehole wall resistance are at equilibrium (Cunningham, 2003). This phase is energy intensive and not only enlarges the borehole, but also significantly weakens the nearby rock

(Cunningham et al., 2007). The energy associated with the elastic straining of the rock is also part of the Shock Energy phase. Following the equilibrium point is the heave phase. During this phase, no further expansion of the borehole takes place. Instead, the more commonly witnessed effects, fragmentation and movement, take place (Cunningham, 2003). Figure 2.4 illustrates this concept graphically.

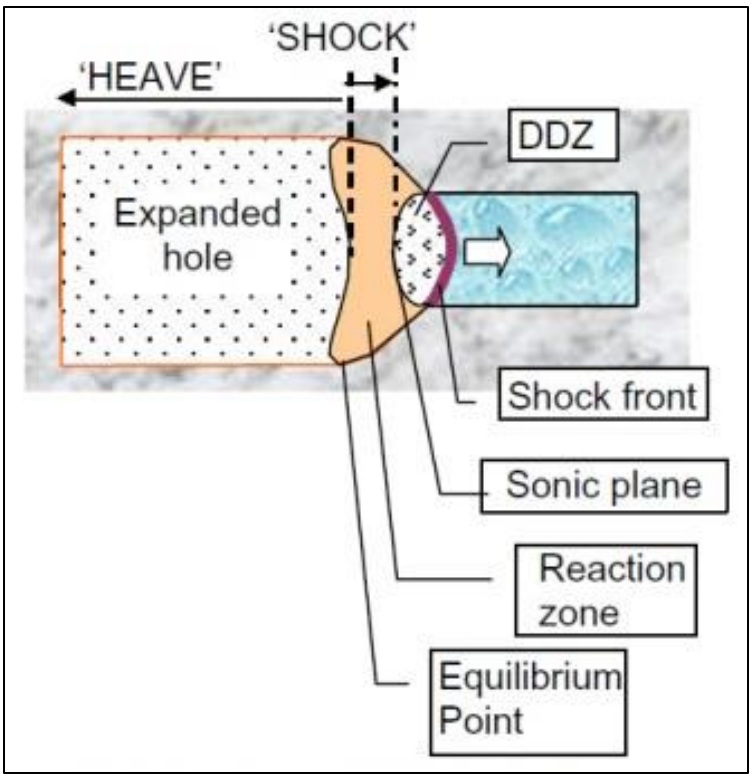

Figure 2.4: Non-ideal detonation and energy partitioning (from Cunningham, 2003)

Confinement plays a significant role in the non-ideal detonation process. It influences the detonation pressure by draining energy from the DDZ and the shock energy by dictating to what extent the borehole expands before the equilibrium point is reached. The effect that confinement and non-ideal detonation have on one another is very much a two-way reaction; therefore,

modeling the situation is complex. Cunningham (2003) had limited success modeling this reaction using Vixen_n detonation code. The most notable problem with creating a working model is the inability to gather data on the interaction between the detonation wave and the borehole wall as a result of the high rates at which the process occurs and its destructiveness.

As discussed by Ouchterlony et al. (2004), only a fraction of the explosive energy is transferred to the rock mass. The energy transferred to the rock mass is called the relative work capacity, or utilization ratio. Based on the work by Ouchterlony et al. (2004), its value varies from approximately 40-50% for ANFO and 60-70% for gassed emulsions, when compared to the total explosive energy. The rest of the energy is lost to heat, both in the rock and in the air, fumes, and airblast. Weight strength is based on the explosion pressure E_o (or possibly a lower value, based on the assumption that at some point the gas pressure stops doing useful work).

Velocity of Detonation (VoD) is often used in the field as a means of calculating borehole pressure, with the belief that higher borehole pressures are a result of higher energy values and more work will be done on the surrounding rock mass (Saharan, 2006). However, the theory behind this thought process is flawed because most commercial explosives do not detonate ideally. VoD is a function of the Detonation Driving Zone (DDZ) and is essentially only a snapshot of a piece of the detonation process. VoD fails to capture the energy release and sustained pressure behind the DDZ in a non-ideal detonation that ultimately leads to greater work being done (Cunningham, 2006).

2.3.2 Cavity Expansion Analysis Applied to Blasting

Cunningham (2003 and 2007) sought to work around the previously discussed uncertainties with high-velocity penetrators. The science behind high-velocity penetrators is heavily documented, in large part to military research, and the process of crater formation is well understood. Although on the surface explosive detonation and high-velocity penetrators may seem rather different, the fundamentals are common. Both result in the rapid expansion of a cavity through the introduction of a dynamic energy source. The science behind the development of high-velocity penetrators will not be discussed in detail here, as the end results are all that is of importance. For further information on high-velocity impact cratering, read Cunningham's work (2003 and 2007).

Cavity Efficiency, E_v, given in units of kJ/cm^3 or GPa (1kJ/cm^3 = 1GPa) is defined as:

$$E_v = {}^{E}/_{\Delta V} \tag{2.18}$$

where E is the kinetic energy of the penetrator and ΔV is the change in volume of the cavity. This linear relationship is similar to the Livingston Theory of Cratering in blasting which relates the mass of explosives required to create a crater of a given volume. However, in this case, no free-face is required.

Cavity Efficiency can be further defined as:

$$E_v = {}^{E}/_{\Delta V} = \sigma * \left[\sqrt{\frac{\rho_p}{\rho_t}} + 2 + \sqrt{\frac{\rho_t}{\rho_p}} \right] \tag{2.19}$$

where σ is the yield strength (Unconfined Compressive Strength, UCS) of the target material around the expanding cavity, ρ_p is the density of the penetrator, and ρ_t is the density of the target. In all cases, the yield strength of the target material is found to be constant at around 25% of the energy/volume content (Cunningham, 2003). Based on these results, it can be concluded that the pressure needed to open a cavity is approximately four times larger than the UCS of the material.

The maximum radius of expansion for a cavity can be defined as:

$$\frac{a_{max}}{r_p} = \sqrt{\frac{\rho_t}{2\sigma}} \left(\frac{V_p}{1 + \sqrt{\rho_t / \rho_p}} \right) \tag{2.20}$$

where a_{max} is the maximum cavity radius as a result of a penetrator with a given radius (r_p), ρ_p is density, and V_p is volume. ρ_t is rock density and σ is rock strength as before.

Cavity Efficiency is characteristic of the target material, with very little dependency on the density of the projectile or the velocity at which is impacts the target. Cunningham has stated that crater blasting in a monolithic block of concrete requires a powder factor of about 0.5 kg/m^3, which is equivalent to an energy factor of approximately 0.0015 kJ/cm^3. Cavity expansion in the same block would require an energy factor of 0.3 kJ/cc (or about 200 times that required to fragment a mass to the free faces). This indicates that a significant portion of energy is used close to the borehole.

After a thorough review of past hyper-velocity penetrator effects on rock, Cunningham (2003) concluded that the energy required to expand a cavity in massive rock is about 1 kJ per cubic centimeter of volume created, and therefore boreholes undergoing expansion by detonation pressures must absorb similar amounts of energy. This can account for up to 25% of energy.

According to Satapathy and Bless (2000), there are four response zones surrounding an expanding cavity.

1. Cylindrical borehole cavity (expanded borehole)
2. Zone of failed material (crush zone)
3. Zone of radial cracking
4. Zone of elastic deformation

The size of each zone and the cavity expansion pressure are dependent upon rock properties readily found in the lab, including Young's Modules (E), Poisson's ratio (v), Uniaxial Compressive Strength (Q), Tensile Strength (T), Mohr-Coulomb parameters, and cohesion and friction angles.

2.4 Optimization Methods

There are numerous optimization methods used within the mining industry, but very few have been applied to blasting. The methods that have been applied to blasting fail to consider all of the applicable variables and none of these methods consider using explosive energy partitioning as a means of optimizing blasting. The optimization methods most applicable to optimization of blasting practices

are goal programming, Mine Scheduling Optimization (MSO), coupled expert system, and the Mine-to-Mill method.

2.4.1 Goal Programming

Goal programming is a multi-objective programming technique. It is an extension of linear programming, used to resolve complex decision-making problems that contain a number of variables and conflicting objectives or goals. Goals are certain desirable conditions that must be met as closely as possible. Each goal has a specific value or range of acceptable values (Charnes & Cooper, 1977).

Goal programming was first introduced in a paper by Charnes et al. (1955). Their publication considered the compensation of executives. Goal programming is the most widely used multi-objective decision-making technique. The primary difference between linear programming and goal programming is that linear programming attempts to solve for one objective, while goal programming solves for many objectives (Tamiz et al., 1998).

Interactive goal programming algorithms are becoming more common, allowing for greater flexibility in goal programming models. These algorithms allow the decision maker to set target values and weights that produce the best solution based on the decision maker's preferences (Tamiz et al., 1998).

Goal Programming problems begin as a mathematical program with a number of inequalities stating the required goals or objectives. The function being maximized or minimized is called the objective function. Constraints are added to place restrictions on the variables. For example, the price of a product cannot be

negative. All constraints and the objective function must be linear in nature (Miller, 2007).

The general form of a mathematical program is:

$$\text{optimize: } z = f(x_1, x_2, \dots, x_n)$$

$$\text{subject to: } \left.\begin{matrix} g_1(x_1, x_2, \dots, x_n) \\ g_2(x_1, x_2, \dots, x_n) \\ \vdots \\ g_m(x_1, x_2, \dots, x_n) \end{matrix}\right\} \begin{matrix} \leq \\ = \\ \geq \end{matrix} \left\{\begin{matrix} b_1 \\ b_2 \\ \vdots \\ b_m \end{matrix}\right.$$

The terms $g_1, g_2, \dots, g_m$ are functions of the variables $x_1, x_2, \dots, x_n$. On the right hand side $b_1, b_2, \dots, b_m$ are all constraints. The objective function, f, is subject to *m* constraints and there are *n* variables (Grayson, 2005).

The mathematical program can be re-written in matrix form for simplification. The standard matrix form is:

$$\text{optimize: } z = \boldsymbol{C}^T \boldsymbol{X}$$

$$\text{subject to: } \boldsymbol{AX} = \boldsymbol{B}$$

$$\text{with: } \boldsymbol{X} \geq \boldsymbol{0}$$

where,

$$\boldsymbol{C}^T \boldsymbol{X} = c_1 x_1 + c_2 x_2 + \cdots + c_n x_n$$

A is an *m x n* matrix, **X** is an *n x 1* matrix consisting of *n* variables, and **B** is an *m x 1* matrix.

If *x* satisfies the constraints **AX** = **B** and $x \geq 0$, then *x* is considered a feasible solution. When *x* achieves the goal of maximizing or minimizing the objective function, it is then considered an optimal solution (Miller, 2007).

Linear programming and goal programming have long been applied to problems in the mining industry, as demonstrated by Hewlett (1961). Since 1961, models have improved efficiency in the mining of a wide variety of materials including: copper, coal, diamonds, gold, iron, lignite, limestone, potassium, and zinc. In addition, LP and GP have seen extensive use in blending problems in oil refining, food processing, paper manufacturing, and cement producing industries (Gershon, 1982). Optimization models have also been used to meet the BTU, sulfur, and ash content requirements for coal shipments (Kim et al., 1981; Gershon, 1981; Hooban & Camozzo, 1981).

There has been significant work in the area of production planning and scheduling, but most models are site specific and do not provide enough generality to be useful in other applications (Gershon, 1982). This work includes determination of optimum cut-off grades by Redenno (1979), refining and process control by Nelle (1962) and Sarmiento and Delgado (1979), ultimate pit limit by Johnson (1969) and Meyer (1969), and strategic planning by Albach (1967) and Jordi and Currin (1979).

2.4.2 Mine Scheduling Optimization (MSO)

Many aspects of mining have previously been modeled independently using linear programming. Since optimization of one aspect of mine operation may result in a negative effect on another, independent models often conflict. Work presented by Gerson (1982) sought to change this, with introduction of the Mine Scheduling Optimization (MSO) concept. MSO uses a mathematical model to optimize the mining process as a whole, from mine to plant to market. It also

incorporates long, intermediate, and short range planning. MSO considers ultimate pit limit, blending, transportation, and production scheduling in one model. The concept emerged following the request of a major copper producer that required a linear programming scheduler. The MSO model was tested using data from the previously mentioned copper producer, a coal company, and a cement producer. In the case of the coal company, data from six of its mines were modeled using MSO. The goal of the modeling was to produce as many BTU's as possible with minimum operating costs, while still meeting sulfur and ash content requirements.

Unlike previous models, MSO is designed to be applied to any kind of open-pit mining operation. This is accomplished using a "core model" that remains mostly unchanged between applications. The core model includes the ultimate pit limit, production scheduling, and transportation problems; however, one exception is the lack of blending considerations, since blending requirements can vary significantly. As a result, the blending portion may need to be reconstructed for each application. Different assumptions and restrictions are fed into the core model for short and long term planning. The short-term model is linked to the long-term model to ensure long-term optimization (Gershon, 1982).

2.4.3 Coupled Expert System

The concept of linking multiple smaller linear programming models together to optimize the entirety of the mining process has continually developed. One example of model linking is provided by Smith and Hautala (1991) in their publication on a blasting coupled expert system at the University of Idaho. A

coupled expert system combines the reasoning power and knowledge of a blasting engineer with mathematical calculations to minimize cost. The goal of this was to optimize all mine operations influenced by blasting. This modeling couples quantitative numeric optimization, used for minimizing cost, and qualitative symbolic modeling, used to define "trouble-free" blasting. Smith and Hautala (1991) recognized the importance of blasting on the down-stream costs of mining including the following: loading, hauling, cleanup, crushing, and grinding.

According to Smith and Hautala (1991), an optimal blast is one that produces good fragmentation and is also trouble free, meaning it has acceptable back break, vibration, oversize, and flyrock. Their work considered a number of ways to model fragmentation, including physics-based models like BLASPA, finite difference models by Sandia and Los Alamos National Labs, and empirical models such as the Kuz-Ram equations. Ultimately, Smith and Hautala (1991) chose to incorporate the fragmentation distributions provided by the Kuz-Ram equations into the model.

The goal of the optimization model by Smith and Hautala (1991) is to find the fragmentation distribution resulting in the lowest drilling, blasting, loading, hauling, and crushing costs. The objective function of this model is as follows:

$$Min\ Z = C_d(D,B,S) + C_b(W,P) + C_l\big(F(d,0)\big) + C_h\big(F(d,0)\big) + C_m(F(d,t))$$

$$\text{such that } h_j(x) + U \geq 0$$

where $x = \{D,B,S,W,P\}$ is the vector of blast design variables which are constrained to lie within acceptable limits defined by constant U.

$F(d,0)$ is the fragmentation distribution as determined using the Kuz-Ram equations as identified in constraint form

$C_d(D,B,S)$ is the drilling cost as a function of borehole diameter (D), burden (B), and spacing (S)

$C_b\ (W,P)$ is the blasting cost which is primarily a function of weight of explosive (W) and price of explosive (P)

$C_l\big(F(d,0)\big), C_h\big(F(d,0)\big), C_m$(F(d,t)) are the loading, hauling and crushing costs which are primarily influenced by the fragmentation as that point in the milling circuit

Input data for these variables, such as costs and fill factors, come from a variety of reference manuals including the Mine Engineers Handbook and a surface mining manual, both of which are generic in nature.

2.4.4 Mine-to-Mill Methodology

One of the most well-known holistic optimization systems currently used in the mining industry is the Mine-to-Mill process developed at the Julius Krutschnitt Mineral Research Centre (JKMRC) in Queensland, Australia. This methodology aims to reduce energy consumption by optimizing all steps of the particle size reduction process (Adel et al., 2005). Mine-to-Mill optimization has been applied to gold, copper, and lead/zinc operations. Operations have seen increases in throughput from 5-18% and cost reductions of approximately 10% (Atasoy et al., 2001; Grundstrom et al., 2001; Hart, et al., 2001; Karageorgos et al., 2001; Paley and Kojovic, 2001; Valery et al., 2001).

The Mine-to Mill optimization methodology includes a number of critical steps as highlighted by Adel (Adel, et al., 2005) below.

- Characterization of appropriate in-situ ore properties
- Modeling and simulation of the performance of each step
- Simulation of the conditions to achieve overall optimum performance
- Implementation of a strategy to achieve optimum performance
- Tracking and measurement of the ore and its properties throughout the various processes

As has been stated previously, trial-and-error techniques are difficult and expensive in a mining environment. The use of modeling and simulation is often quicker and cost effective. The Mine-to-Mill methodology applies JKSimBlast for blasting simulation. JKSimBlast has the ability to analyze and evaluate energy, scatter, vibration, fragmentation, damage and cost (Adel, et al., 2005). This simulation software uses the Crush Zone Model (CZM) (Kanchibotla et al., 1999) to model blast fragmentation. CZM uses a semi-mechanistic approach to calculate the volume of crushed material around each borehole, thus estimating the amount of fines in the fragment size distribution. The Kuz-Ram model is used to predict the coarse material in the size distribution (Adel et al., 2005). JKSimMet is a mineral processing simulation package used by the Mine-to-Mill methodology to track particle break-down throughout the processing plant.

Using this methodology, a detailed site survey is conducted to collect data about a specific mining operation. Blasting related data includes blast design, rock characteristics through core sample testing, and explosive characteristics including determination of velocity of detonation (VoD). Collected data is fed into

JKSimBlast. The blasting parameters are varied to create differing fragmentation size distributions. These fragment size distributions are then input into JKSimMet, along with processing plant parameters. The information is processed and analyzed to construct improved operating strategies.

The operating strategies are then implemented and re-analyzed to quantify improvements. Improvements are typically quantified using a side-by-side comparison, first using the old blasting method and standard operating procedures (SOPs), then followed by the new blasting method and SOPs established using the Mine-to-Mill optimization methodology. The energy consumption and throughput can be directly compared in this manner. (Adel et al., 2005; Adel et al., 2006).

Chapter 3. Test Rationale and Methodology

Small-scale testing was conducted at the University of Kentucky Explosives Research Team's (UKERT) underground laboratory located in Georgetown, KY. The purpose of this testing was to better define energy partition component values by isolating specific components for measurement. The main energy components considered for testing in this dissertation include air overpressure (air blast), fragmentation, kinetic energy (heave), elastic deformation (ground vibration), and borehole enlargement.

Section 2.2.1 discusses the various ways that explosive energy is calculated. In energy partitioning research, all of the energy released during a confined detonation much be considered. Therefore, it would not be appropriate to use values gained from underwater or cylinder testing. Instead, heat of detonation is appropriate for use here because it encompasses all of the energy released during detonation. The explosive product used for this testing is PETN, a commercially available high explosive. The assumption will be made that the PETN is detonating close to ideally. This assumption is discussed more in Section 4.3 where the explosive charge makeup is detailed.

Significant work has been done in the past to determine the amount of energy required to fragment rock as shown in Section 2.2.2. Where this work falls short is in the measurement of the new surface area created during a blast, mostly due to the inability to accurately capture fines through photographic analysis. This testing uses small-scale tests coupled with a low powder factor to produce a

manageable number of fragments. The new surface area created by these fragments can then be directly measured.

The current methodology used to estimate energy to ground vibration is full of simplifying assumptions and approximations. This, coupled with the known limitations of seismographs discussed in Section 2.2.3, leads to results that are likely imprecise. A new methodology using strain measurement is proposed. By definition, strain is change in length (deformation) over length. Deformation can be thought of as the displacement of particles. The derivative of displacement with respect to time is velocity. Particle velocity is commonly the metric used for measurement of ground vibration. Following this line of thought, it is possible to measure the energy commonly associated with ground vibration by measuring the deformation of the rock mass using strain gauges. This thought process is further supported by the work of Sanchidrian et al. (2007) where they state that shock waves propagate as plastic and elastic waves. These waves are witnessed as ground vibrations. In solid mechanics, elastic deformation (strain) energy is the potential energy of an elastic object undergoing deformation caused by an applied load. In this case, the applied load is the compression and tension waves caused by the detonation of a charge in the borehole, the elastic object is the rock mass, and the energy transmitted to the rock mass is measured through deformation. Based on this reasoning, there is sufficient evidence to say that ground vibration energy and elastic deformation energy are equivalent and can be measured using strain gauges.

The current methodologies for calculating translational kinetic energy discussed in Section 2.2.4 are considered adequate. One area of concern is the velocity profile of the fragmented particles from the free face to the borehole. In an optimized situation, the velocity would be highest at the face and be near zero at the borehole. This would indicate that energy was not wasted on excessive heave of the material. However, this is rarely the case as shown by the "power trough" commonly witnessed along the backside of a muckpile. Because very few blast act ideally, the assumption will be made for this dissertation that the translational velocity profile is consistent from the face to the borehole.

There is no methodology currently in place to calculate rotational kinetic energy of fragments. To accurately calculate rotational kinetic energy, the angular velocity and the moment of inertia about the axis of rotation must be known. For this testing, high-speed video is used to determine the angular velocity and the moment of inertia for each fragment will be calculated using 3D modeling software.

The methodology used to calculate explosive energy yield from an open air blast was discussed in Section 2.2.5. This methodology has been proven reliable over the years and will used in this testing to calculate the explosive energy transmitted to air overpressure. For the sake of clarity, this dissertation will use air overpressure rather than air blast to describe the energy transmitted to the air. Air blast only includes the audible portion of energy transmitted, while air overpressure encompasses all of the energy transmitted to the air.

The information gained from cavity expansion analysis (CEA) discussed in Section 2.3 is used to calculate the amount of energy transmitted to deformation of the rock mass in the immediate vicinity of the borehole. According to CEA, the amount of energy absorbed during borehole enlargement is directly proportional to the change in borehole volume.

The testing for this dissertation consisted of four individual test series: fully confined chambering, stemming, strain mapping, and block tests. During the first three test series, heave and fragmentation were eliminated from the energy partitioning equation (Eq. 2.12) by conducting the tests in massive limestone. Therefore, a substantial portion of the explosive energy was transferred to air overpressure and elastic deformation. During the last test series, heave and fragmentation were reintroduced into the equation by conducting the tests in concrete blocks.

The primary purpose of the fully confined chambering test series was to measure borehole enlargement. To do this, four holes were drilled in the massive limestone floor of the test arena. The volume of each hole was measured before and after an explosive charge was detonated in the hole. The secondary purpose of this series was to test the air overpressure measurement methodology.

The stemming and strain mapping tests reused two of the four holes. The purpose of the stemming test series was to show a correlation between air overpressure and elastic deformation when the type of stemming material was

varied. The strain mapping tests consisted of a strain gauge sensor array to illustrate how strain levels decay with respect to distance. It also served to help explain the strain measurement anomalies found in the stemming tests.

The concrete block testing series was a small-scale effort to measure a significant portion of the energy partitioning components minus heat. Three tests were conducted on 4’ x 4’ x 4’ concrete blocks. Four pressure sensors were positioned around the block to capture air overpressure. A velocity screen and high-speed camera were used to calculate translational and rotational kinetic energy. Three strain gauges were adhered to the top of the block to measure elastic deformation. Finally, the fragments were collected and the new surface area was measured to calculate fragmentation energy.

At the completion of these tests series a significant portion of the total explosive energy could be accounted for. The test methodologies developed during this dissertation are shown to be sensitive enough to capture changes in the balance between the four primary energy components measured and this methodology can be applied to full-scale testing with some slight changes.

Chapter 4. Fully Confined Chambering Tests

4.1 Methodology

The purpose of the chambering tests and subsequent fully confined test series was two-fold. First, it allowed for the measurement of borehole enlargement, or chambering. Second, by conducting the tests in massive limestone, fragmentation and heave (to an extent) were removed from the partition equation. Therefore, all explosive energy must then be transferred into deformation of the surrounding rock mass, air overpressure, and stemming ejection.

Four holes, labeled 1-4, were drilled in the floor of the test arena at a radius of 10.33 feet from a central point. Holes were placed at a 90 degree angle from one another. The central point would later serve as the geophone mounting location. This layout is shown in Figure 4.1.

Holes were drilled using a hammer drill with a 7/8 inch bit to a depth of approximately 30 inches. A 7/8 inch diameter bit was chosen to allow adequate space for insertion of multiple strands of detonating cord, a detonator, and VoD probe cable. The volume of each hole was measured before testing and then again after to check for borehole enlargement. Compressed air was used to remove any drill cuttings from the hole prior to the initial volume measurement, and then again after the test to remove any fine material created by the blast. Dry sand and water were used to measure the volume of the holes.

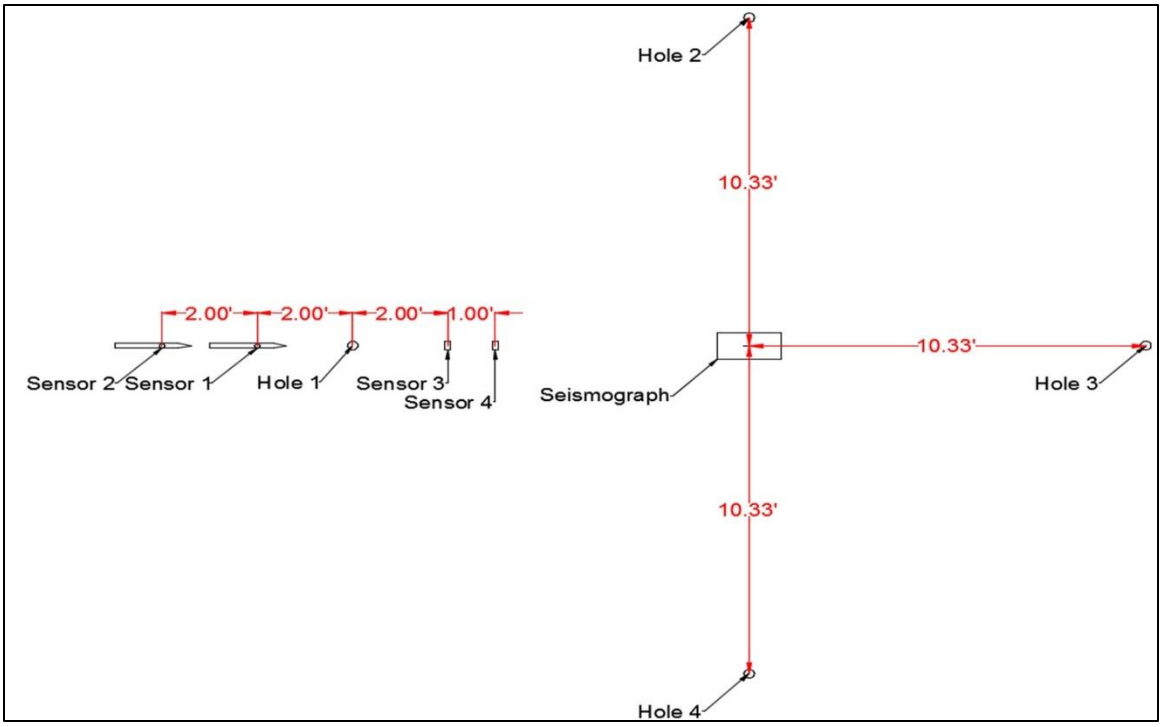

Figure 4.1: Plan view of setup for chambering test series

Testing was conducted in a sequential fashion, with Hole 1 being instrumented and tested first. The test equipment was broken down and then redeployed for Hole 2. This process continued for Holes 3 and 4, ensuring that the sensor position relative to the borehole was the same for each test.

4.2 Instrumentation

To accurately capture as many variables as possible, a wide array of sensors were deployed for data collection during the blast event. Instrumentation included the following components: MREL ProbeCable for velocity of detonation (VoD) measurement, two PCB Model 740B02 piezoelectric strain sensors, two PCB Model 137B23B free-field piezoelectric pencil sensors, one MREL Blaster's Ranger high speed camera, and one White Model MS-2G seismograph.

The PCB free-field pressure sensors used are capable of reliably measuring blast overpressures of up to 50 psi. They were mounted linearly on a frame at a distance of 2 feet and 4 feet from the borehole collar. The frame was positioned at a 45 degree angle to the borehole based on the assumption that the air overpressure shell would expand hemispherically, as is commonly witnessed with explosive charges detonated at ground level. The setup is shown below in Figure 4.2.

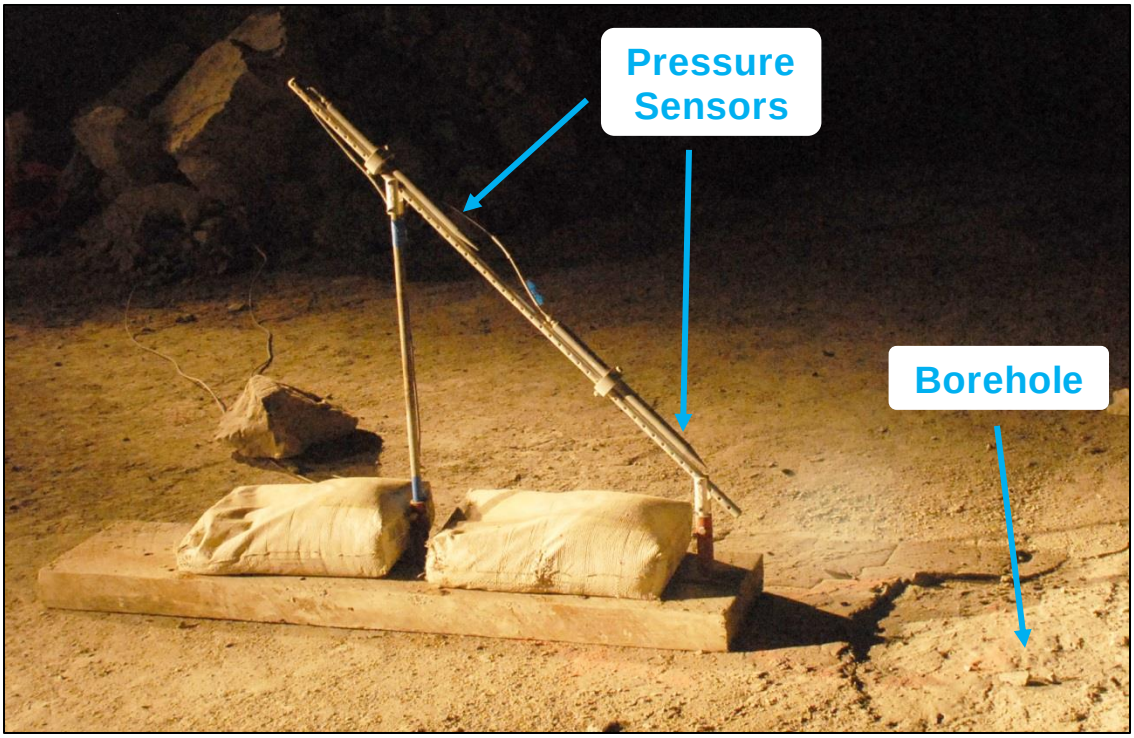

Figure 4.2: Typical free-field pencil sensor setup

The strain sensors were placed transversely at a distance of 2 feet and 3 feet from the borehole. The sensors were adhered to the rock surface using Loctite brand cyanoacrylate glue (as recommended by the sensor manufacturer). An attempt was made to attach a film strain gauge 1 foot from the borehole. This proved difficult, in part due to collar flaking and ejected material; therefore, strain

measurements close to the hole were not recorded for this series. A PCB strain sensor adhered to the rock surface is shown in Figure 4.3.

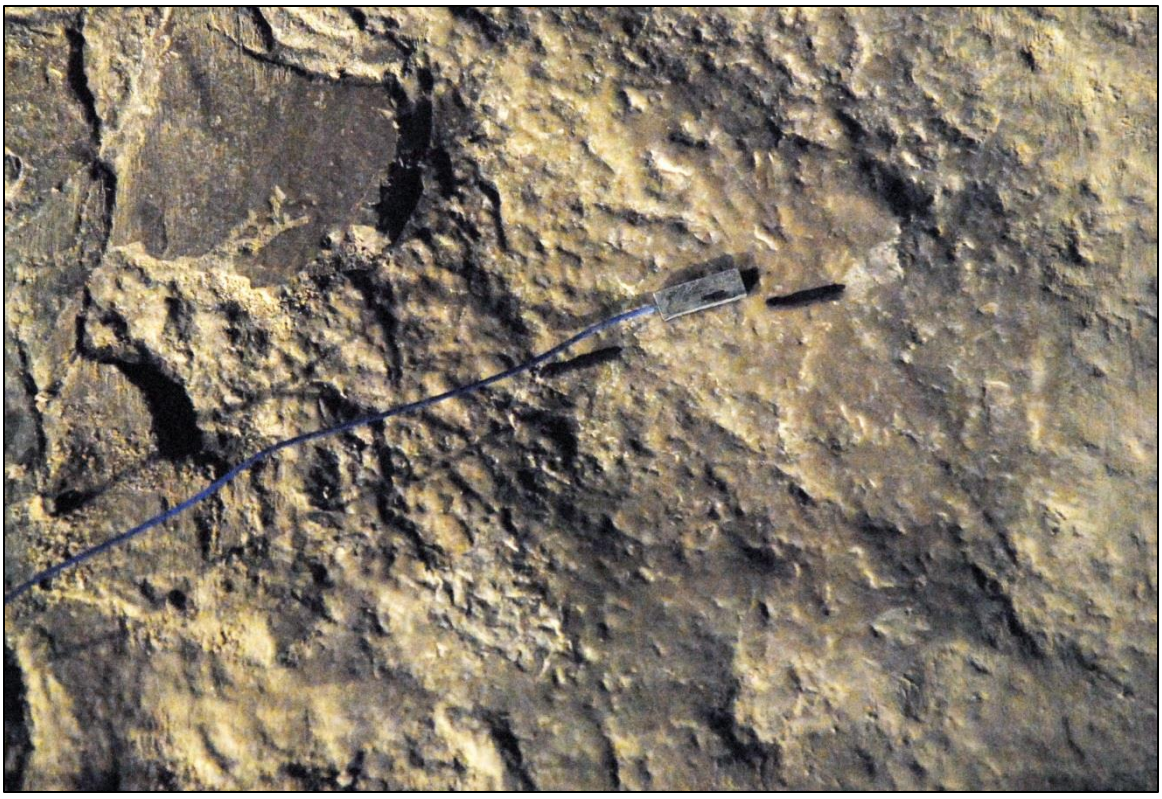

Figure 4.3: PCB strain sensor adhered to the rock surface

The White seismograph was positioned at the center of the test arena, 10.33 feet from the borehole. A scaled distance of 50 was calculated using the following equation:

$$SD = \frac{D}{\sqrt{W}} \tag{4.1}$$

where SD is scaled distance, D is the distance from the charge to the seismograph, and W is the weight of the charge.

A scaled distance of 50 is used when the site is within 300 feet of a structure and was used to determine seismograph placement for this test series because of the close proximity from the charge to the seismograph.

The geophone was securely fastened to a 1/4 inch thick steel plate. This plate was then fastened to the rock surface using four masonry screws. This method of attachment has been used previously by UKERT and provided good geophone coupling. The microphone was attached to the lid of the seismograph's storage box. The seismograph remained at the center of the test arena for all trials. When necessary, the geophone and microphone were rotated 90 degrees to remain pointed toward each of the four blasts. Figure 4.4 shows the positioning and mounting of the seismograph equipment.

MREL Green ProbeCable was taped to the length of detonating cord before the charge was placed down the bore hole. Due to the very short length of the powder column, accurate VoD data was not collected.

Data collection was accomplished through the use of an MREL Datatrap II. The Datatrap II is capable of recording eight channels at sampling rates of up to 10 Mhz. For this test series, five channels were recorded at a sampling rate of 1 Mhz. A PCB 481A signal conditioner provided the necessary power regulation to the sensors and served as the interface between the sensors and the Datatrap. The signal conditioner protects against voltage and current overloads and also warns of any sensor faults.

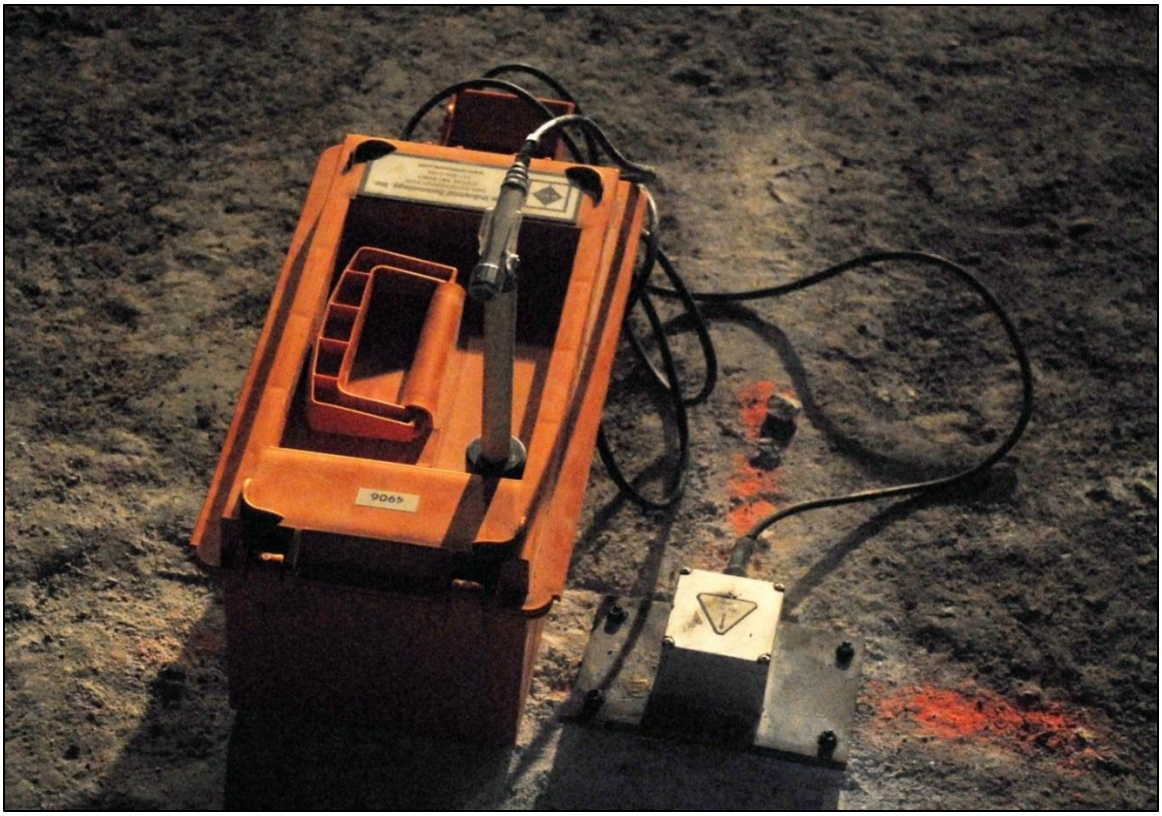

Figure 4.4: Seismograph setup

The MREL Blaster's Ranger high-speed camera was used to collect video of the experiment. In the past, high-speed video has proven useful in documenting explosive tests, especially when unexpected problems arise. The frame rate was set to 250 frames per second. This rate provided a good balance of speed and image quality given the lighting available.

Figure 4.5 provides an overview of the test arena and instrumentation setup. The data acquisition equipment is placed inside of a steel pipe to protect it from possible flying material. The high speed camera is placed adjacent to the data acquisition equipment. Also shown are the three high intensity lights needed to illuminate the test arena for high-speed video.

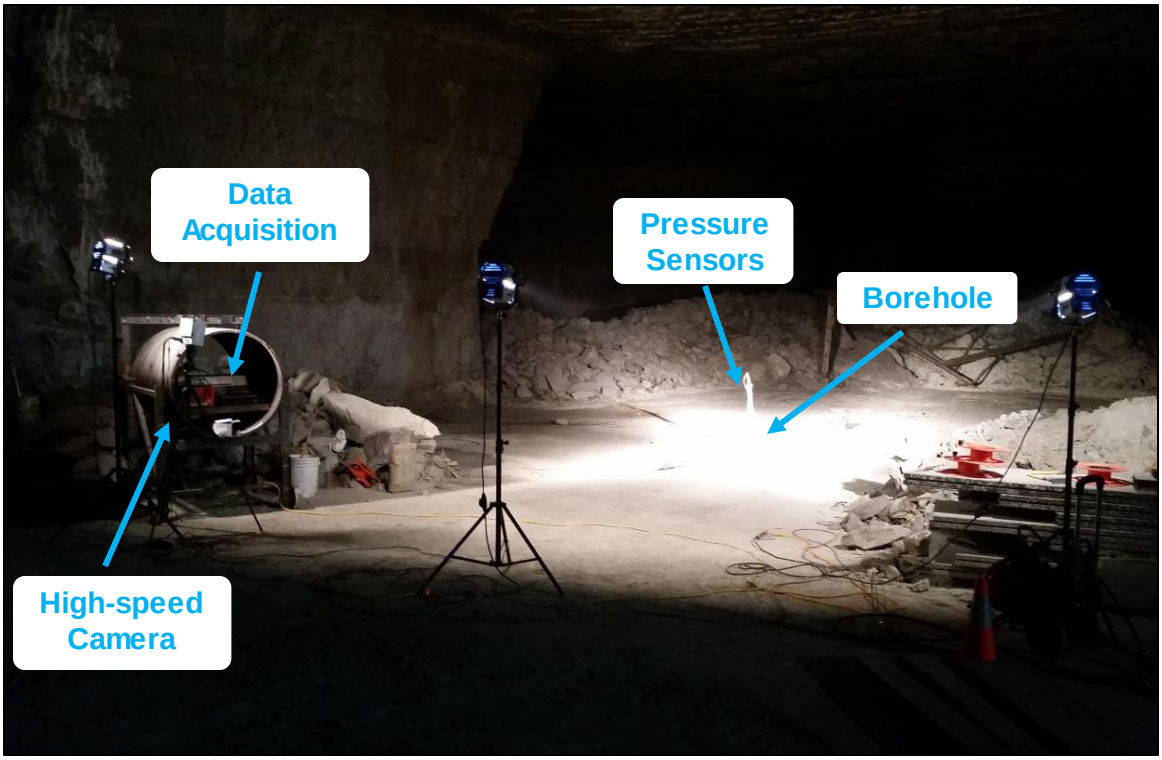

Figure 4.5: Test arena and instrumentation setup for chambering test series

4.3 Explosive Charge

All tests were conducted using 18 inches of 200 grain detonating cord and an electric detonator, yielding 0.043 pounds of PETN high explosive. For the first two tests, the detonating cord was left as a single 18" strand. The charge was coupled using moist sand and stemmed using 10 inches (Hole 1) and 11.5 inches (Hole 2) of 1/4 inch gravel. This stemming method proved to be ineffective, with significant flaking occurring around the collar of the borehole. This result was not completely unexpected. The general rule of thumb for stemming size states that the material should be no greater than 1/8 of the hole diameter, and the stemming height should be at least 24 times the hole diameter. In this case, the stemming should be no greater than 1/8 inch in size and stemming height should be 21 inches.

For the remaining two tests, the test procedure was modified to more closely following the general rules of thumb for blasting. Detonating cord was cut into two, nine-inch lengths, thereby decreasing the powder column height, increasing the amount of stemming, and keeping the overall explosive charge weight constant. These changes increased the stemming height to 19.75 (Hole 3) and 20.5 inches (Hole 4). In addition to the increased stemming height, dry, general purpose sand was used as a stemming material, instead of the fine gravel. While the stemming was still ejected for these two tests, damage to the borehole collar during the blast was significantly reduced, indicating that less of the energy was escaping the borehole through stemming ejection, and was being contained deeper within the hole.

Reported experimental heat of detonation values for PETN vary from 5,730 kJ/kg (Scilly, 1995) to 6,404 kJ/kg (Meyer, 1987). As a result, the expected detonation energy ranges between 114.6 kJ and 128.1 kJ for this test series. For this test series and subsequent test series, the available detonation energy value used for calculation of percentages will be at the low end of published values. This assumption is made because individual strands of detonating cord were bundled together, resulting in a less energetic event when compared to using a bulk product.

4.4 Chambering Test Results

Data analysis of the chambering test series provided useful information. Based on the data collected, it is possible to analyze borehole enlargement and

calculate energy loss to air overpressure. When directly compared there does not appear to be an association between air overpressure and strain. However, when taking into account other factors, such as stemming type and borehole condition, a trend does appear. This trend is discussed later in Section 4.4.5 “Conclusions.”

Experts in the field of ground vibration have previously discussed their apprehension towards using seismographs to accurately measure ground vibration at a level needed for calculating energy because of the content filtering and distortion of frequency along the ground surface (Ouchterlony, 2004; Lusk, 2014). For thoroughness, a seismograph was used during this test series. However, the seismographs inherent limitations coupled with a small charge size yielded inconclusive ground vibration results for this test series.

4.4.1 Chambering Calculations

The primary purpose of the initial test series was to determine the amount of energy transferred to borehole enlargement or chambering. As discussed previously, this was accomplished by measuring the before and after volumes of the borehole using sand and water.

Table 4.1 summarizes the volume data collected. The initial hole depths are within a narrow range of 29.75 inches to 30.25 inches. The hole depths after testing varied considerably more, from 27.75 inches to 29.63 inches. This change can be attributed to flaking of the borehole collar and highly compacted debris in the bottom of the borehole. In all instances, the borehole depth

decreased (most notably on Holes 1 and 2, a result of severe collar damage). For comparison purposes, the theoretical volume of each hole is calculated, using the before and after depths while assuming a consistent diameter of 7/8 inch. In all cases, the measured volume is approximately 10% greater than the calculated volume. This is due to slight variations in hole diameter incurred during the drilling process.

Table 4.1: Summary of volume data for borehole chambering tests

	Before			After			Calculated	
Hole	Depth (in)	Sand Volume (mL)	Water Volume (mL)	Depth (in)	Sand Volume (mL)	Water Volume (mL)	Before Volume (mL)	After Volume (mL)
1	29.75	-	320	28.50	340	350	293	281
2	30.25	330	330	27.75	290	300	298	273
3	30.00	320	325	29.63	330	330	296	292
4	30.13	330	330	29.50	320	325	297	291

As a result of the change in borehole depth, it is incorrect to directly compare the before and after volumes of each hole. Therefore, the data is normalized by dividing the measured volume in mL by the hole depth in inches. The normalized data is now presented in terms of mL/inch, allowing for direct comparison. Normalized data is shown in Table 4.2.

Table 4.2: Normalized before and after volume data

	mL/inch (Sand)			mL/inch (Water)		
Hole	Before	After	% Diff	Before	After	% Diff
1	10.76*	11.83	9.47*	10.76	12.39	14.11
2	10.91	10.45	-4.29	10.91	10.81	-0.90
3	10.67	11.14	4.33	10.83	11.14	2.78
4	10.95	10.85	-0.98	10.95	11.02	0.57

*Assuming an initial volume of 320mL

The percent difference between the before and after normalized values range from -4.29% to 9.47% for sand and -0.90% to 14.11%. for water. The presence of negative normalized volume changes indicates that experimental error is present. A likely source of this error is the precision of the measuring devices used. In this case, a standard tape measure and wooden dowel rod were used to measure the hole depth and a 1000mL graduated cylinder was used to measure the volume of material (sand or water) being poured in the hole.

The higher percent difference realized for Hole 1 is not believed to be completely accurate. The hole did not hold water, unlike the other three holes. Lack of water retention is a strong indication that a void or fracture in the rock mass was exploited during the test.

To minimize the effect of experimental error, the average change in volume/inch was calculated. This change was determined to be 0.24 mL/in and 0.48 mL/in when using the sand measurement and water measurement, respectively, resulting in an overall average volume change of 0.36 mL/in. This value was multiplied by the original hole depth to calculate total change in volume per hole.

The assumption that 1 kJ is required to expand a borehole one milliliter (1 cc) was used. Therefore, the change in volume in mL is equivalent to the energy lost to borehole chambering in kJ. The results are summarized in Table 4.3.

Table 4.3: Summary of borehole chambering energy values

Hole	Depth (in)	Change in Volume (mL)	Energy (kJ)
1	29.75	10.71	10.71
2	30.25	10.89	10.89
3	30.00	10.80	10.80
4	30.13	10.85	10.85

The average energy lost to borehole chambering was determined to be 10.81 kJ or 9.4% of the total available energy. The highest reliable value (Hole 1 measured using sand) was 30.04 kJ or 26.2%.

4.4.2 Supplemental Borehole Chambering Testing and Calculations

After completing the original set of borehole chambering tests, additional testing was completed using a larger charge size. The intent of this testing was to determine what effect charge size had on borehole enlargement and provide additional data for analysis, considering the wide spread of measurements gathered during the original set of tests. Like the previous tests, borehole volume was measured before and after using sand. Due to the likelihood of cratering caused by the much larger charge size, no additional instrumentation was implemented for this testing. An equipment failure limited this test series to two useable holes.

For this testing, 0.375 pounds (0.17 kg) of an ammonium nitrate based emulsion was used rather than PETN. The expected heat of detonation for this product is 6712 kJ/kg (Buczkowski & Zygmunt, 2011) yielding 1141 kJ of total available energy for this series.

The original and post-blast borehole depths and volumes are presented in Table 4.4. Hole 6 remained intact following the test. Hole 5 experienced significant cratering and fragmentation to a depth of approximately 11.5 inches leaving the bottom 18.25 inches with no visible damage.

Table 4.4: Summary of Supplemental Borehole Volumes

	Before			After		
Hole	Depth (in)	Volume (mL)	Normalized Volume (mL/in)	Depth (in)	Volume (mL)	Normalized Volume (mL/in)
5	31.875	346	10.85	18.25	308	16.87
6	31.75	338	10.64	32.75	572	17.47
Average	31.81	342	10.75	25.50	440	17.17

The normalized volume change for Hole 5 was 6.02 mL/in resulting in a net volume change of 192 mL. Hole 6 normalized volume change was slightly higher at 6.83 mL/in, netting a volume change of 217 mL. Applying the same assumption that 1 kJ is required to create 1 mL change in volume, it was determined that 192 kJ or 16.8% of the total available energy was transferred to borehole chambering for Hole 5. 217 kJ or 19.0% of the total available energy was transferred to chambering for Hole 6.

4.4.3 Pressure Shell Energy Calculations

Calculating explosive energy based on pressure front velocity is not a novel idea as shown by the work of Hoffman et al. (2009). Using pairs of sensors placed around a blast, the velocity and duration (or thickness) of the expanding pressure shell can be calculated. Each pair of sensors is a known distance from the blast allowing for the determination of the radius, surface area, and volume of the

shell. Using this information, it is then possible to calculate the associated energy.

For data collection and calculations, it is assumed that the expanding pressure shell is hemispherical in nature, originating at the collar of the borehole. At greater distances this assumption is likely correct. However, at close in distances, the shell is likely more cylindrical or conical in shape because of venting directly above the borehole. Without evidence to substantiate this theory, the assumption that the shell is hemispherical in shape remains for this section. Figure 4.6 illustrates the expanding shell in relationship to the borehole. Also shown are pressure sensor locations.

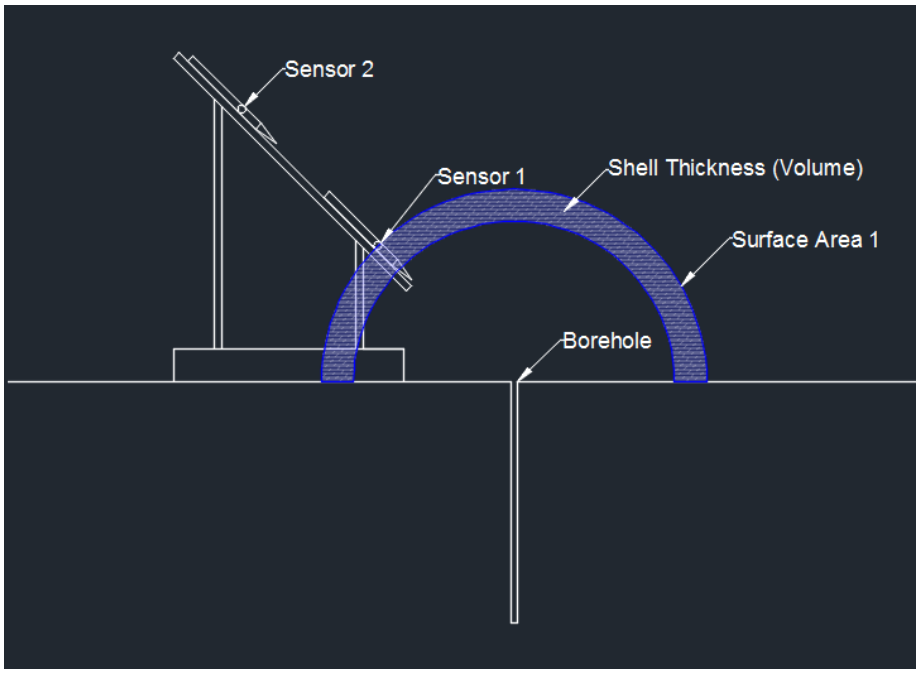

Figure 4.6: Illustration of pressure shell radius, surface area, and volume

The first step for pressure shell calculations is to download the raw data from the data acquisition device. Data collected from the Datatrap is displayed in a

voltage versus time format. A sensor specific calibration factor is applied to the data to convert the voltage readings to pressure (PSI). The maximum pressure and time at which the peak pressure occurred is recorded for both sensors. From this information, the time necessary for the pressure wave to travel from Sensor 1 to Sensor 2 can be determined. Since the distance between the two pencil sensors is a known distance of 2 feet, it is then possible to calculate the wave velocity. Table 4.5 provides a summary of the maximum pressure, time of arrival (TOA), time difference, and wave velocity for each hole. For this test series, the TOA was taken as the time at which the maximum pressure was reached. Note that wave velocity is presented in English and Metric units to facilitate future calculations. Figure 4.7 shows a typical Pressure vs. Time plot for this test series. For simplicity, pressure data is converted from PSI to kPa and calculations are completed using metric units.

Table 4.5: Summary of maximum pressure and time of arrival (TOA)

	Sensor 1 (2 ft.)			Sensor 2 (4 ft.)			Wave		
Hole	Pressure (PSI)	Pressure (kPa)	TOA (ms)	Pressure (PSI)	Pressure (kPa)	TOA (ms)	Time Diff (ms)	Velocity (fps)	Velocity (m/ms)
1	2.125	14.65	3.77	0.759	5.481	5.67	1.90	1052	0.3205
2	4.864	33.54	2.90	2.548	17.57	4.55	1.65	1208	0.3683
3	4.351	30.00	4.82	1.875	12.93	6.68	1.86	1075	0.3277
4	3.283	22.63	4.75	1.529	10.54	6.46	1.71	1171	0.3569

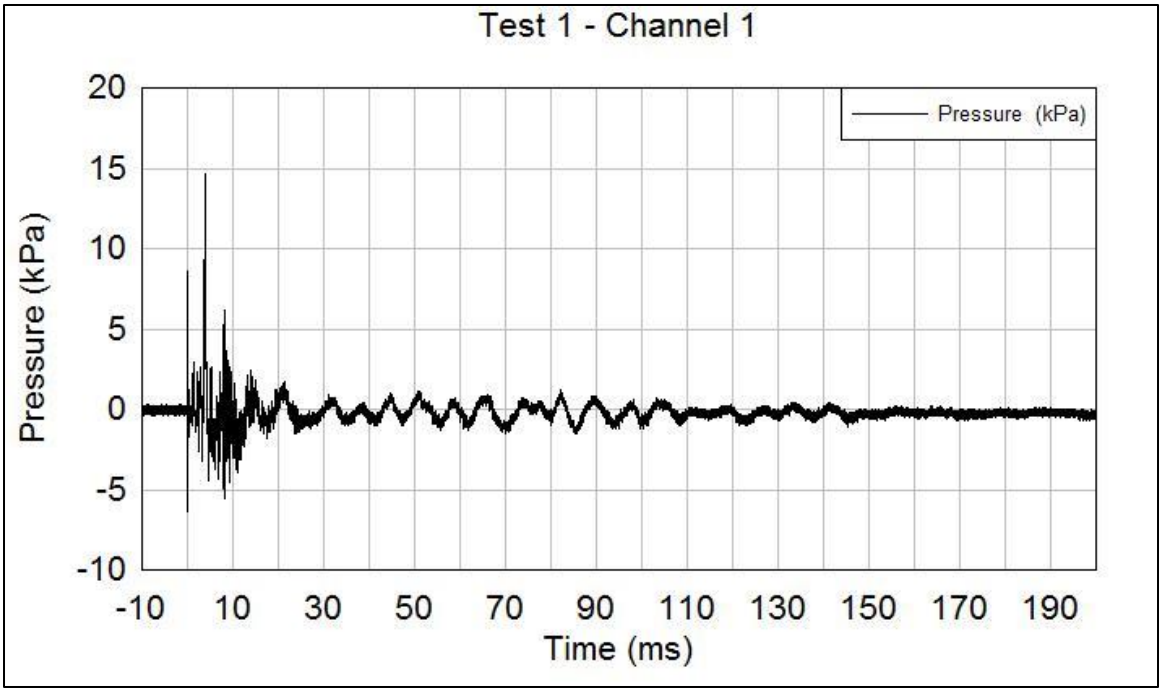

Figure 4.7: Pressure versus time data for energy calculations

After the wave velocity is calculated, time (ms) is converted to distance (m). This is done by multiplying the time scale and the calculated wave velocity. This conversion is necessary to determine the thickness of the pressure shell. Figure 4.8 shows the converted plot.

The pressure data is next multiplied by the surface area of the pressure shell. In this case, it is the surface area of a hemisphere, with a radius equal to the distance from the borehole collar to the sensor. This distance is 2 feet (0.61 m) for Sensor 1 and 4 feet (1.22 m) for Sensor 2. These conversions result in a Pressure-Area (kPa-m^2) versus Distance (m) plot, as shown in Figure 4.9.

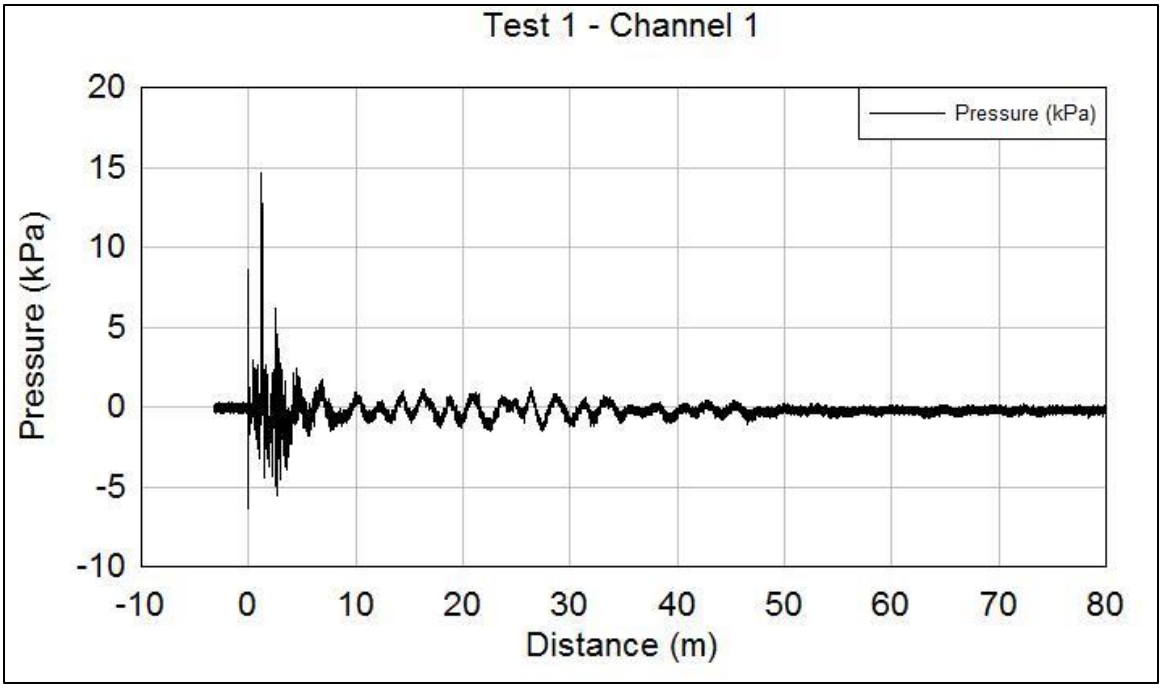

Figure 4.8: Time scale converted to distance plot

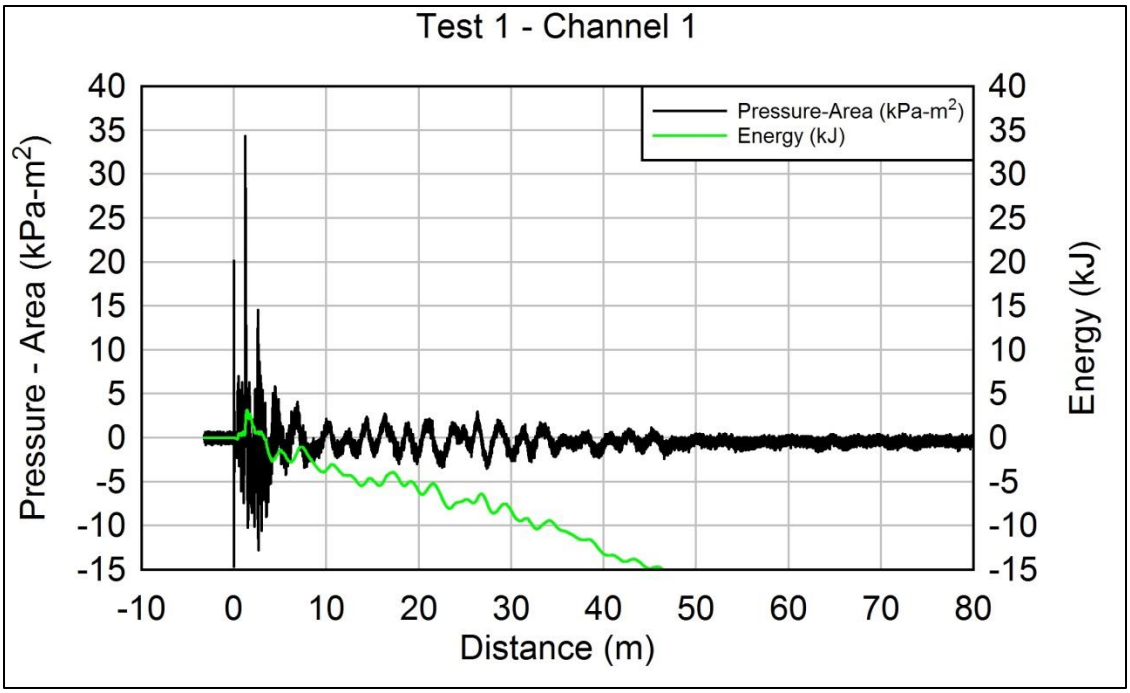

Figure 4.9: Final data plot after conversion to Pressure-Area vs. Distance

The plot is then integrated and the maximum value taken as the pressure shell energy. This procedure is repeated for the data recorded at both sensors, with the assumption that the wave velocity is the same at Sensors 1 and 2. Table 4.6 summarizes the data and energy calculations. Area 1 is the area of the hemisphere as the pressure shell approaches Sensor 1, and Energy 1 represents the calculated energy based on the data provided by Sensor 1. Area 2 and Energy 2 represent the same conditions for Sensor 2.

Table 4.6: Summary of pressure shell energy calculations for initial test series

Hole	Time Diff (ms)	Velocity (m/ms)	Area 1 (m^2)	Energy 1 (kJ)	Area 2 (m^2)	Energy 2 (kJ)
1	1.902	0.3205	2.335	3.148	9.340	7.321
2	1.655	0.3683		3.508		26.732
3	1.860	0.3277		8.341		17.080
4	1.708	0.3569		6.855		15.580

Hole to Hole differences in energy can be explained by variations in the effectiveness of the stemming and borehole condition. However, differences in energy from between sensors indicate that the assumption of the hemispheric pressure shell expansion is not completely correct. In order for this assumption to hold true, Energy 1 and Energy 2 should be roughly equivalent, with Energy 2 being slightly less due to other environmental losses. Although the overpressure decreases from Sensor 1 to 2, the area being affected increases significantly. Without additional data to further refine the shape of the pressure shell, future calculations will use the assumption that the pressure shell created by venting gases is hemispherical in shape. Peak pressure values are shown in Appendix A and air overpressure energy plots from Tests 1 – 4 are in Appendix B.

4.4.4 Conclusions

Borehole chambering results varied significantly. Using normalized values to mitigate experimental error, the average energy transferred to borehole chambering for Holes 1-4 was 9.4%. For the larger charge size in Holes 5 and 6, the energy transfer was determined to be roughly 18%.

This test series demonstrated that there is merit to the methodology used for calculating energy transferred to air overpressure. At first glance, the energy values summarized in Table 4.5 appear to be sporadic. However, when analyzing the test series as a whole, by taking into account stemming material and borehole condition, patterns emerge.

Following testing, Hole 1 would not retain water, indicating that cracks were present. Cracks allowed the expanding gases to vent into the surrounding rock mass, rather than into the atmosphere. Hole 2 was stemmed using fine gravel, which held poorly, allowing the gasses to quickly vent to the atmosphere. Holes 3 and 4 used wet sand, which provided more resistance to venting, thus transmitting more energy to the surrounding rock mass. These observations are further reinforced by the strain data results, summarized in Table 4.7. Hole 1 had the lowest strain values and Holes 3 and 4 had the highest.

Table 4.7: Summary of strain results from chambering tests

	Sensor 3 (2 ft.)	Sensor 4 (3 ft.)
Hole	Strain (με)	Strain (με)
1	49.82	23.62
2	71.70	16.67
3	99.46	26.29
4	90.89	29.36

The total available explosive energy for this test series is 114.6 kJ. Energy transferred to air overpressure ranged from a minimum of 6.39% (Hole 1) to a maximum of 14.9% (Hole 2). These values are understated because of the positioning of the free-field pressure sensors, which failed to capture a portion of the higher overpressures venting vertically from the borehole. Future tests will feature pressure sensors mounted directly above the borehole.

Chapter 5. Stemming Tests

The purpose of this test series was not to calculate the explosive energy transmitted to each energy partition component. Instead, the goal was to determine if there is correlation between measured air overpressure (air blast) and measured elastic deformation (ground vibration).

5.1 Methodology

The decision was made to reuse a single borehole multiple times for the stemming tests. This significantly sped up the testing process because no additional holes were drilled and instrumentation remained stationary following each test. Hole 4 was chosen for this test series. After inspection, it appeared to be the most robust with no damage present.

Six coupling and stemming combinations were chosen to vary the amount of energy transferred to the rock mass versus vented out of the borehole. The first combination used dry sand as a coupling material with non-Newtonian fluid stemming. The non-Newtonian fluid was a cornstarch/water mixture. A half-inch thick rubber plug was used to separate the dry sand from the fluid. The second combination used no coupling material. Instead, a rubber plug was placed above the charge, and the remainder of the hole was stemmed using dry sand. The third and fourth combinations used all sand and all non-Newtonian fluid, respectively. The fifth combination used non-Newtonian fluid as a coupling material and sand as stemming material. The sixth combination was left as an open borehole and did not use any material for coupling or stemming.

Using a variety of coupling/stemming combinations allowed for the comparison of many different parameters. For example, it is known that an air coupled charge will transfer less energy into the surrounding rock mass when compared to a charge that has been fully coupled using materials such as sand, gravel, or water. Given this knowledge, it can be assumed that the overall energy partitions will be skewed based on the type of coupling material. The same assumption can also be made when varying the integrity of the stemming material.

5.2 Instrumentation

The instrumentation setup for the stemming tests was similar to that of the initial confined test series, with a few additions and modifications. The most notable change was the addition of two PCB free-field pressure sensors directly above the borehole. A specially designed sensor stand was constructed to hold the sensors above the borehole and protect the delicate cabling from stemming ejection. The sensors were held at a height of 4 feet and 6 feet above the borehole collar. A velocity screen was also attached to the base of the stand. This velocity screen provided a 1 foot by 1 foot square grid for high speed video analysis of the stemming ejection. The sensor stand with pencil sensors and velocity screen are shown in Figure 5.1.

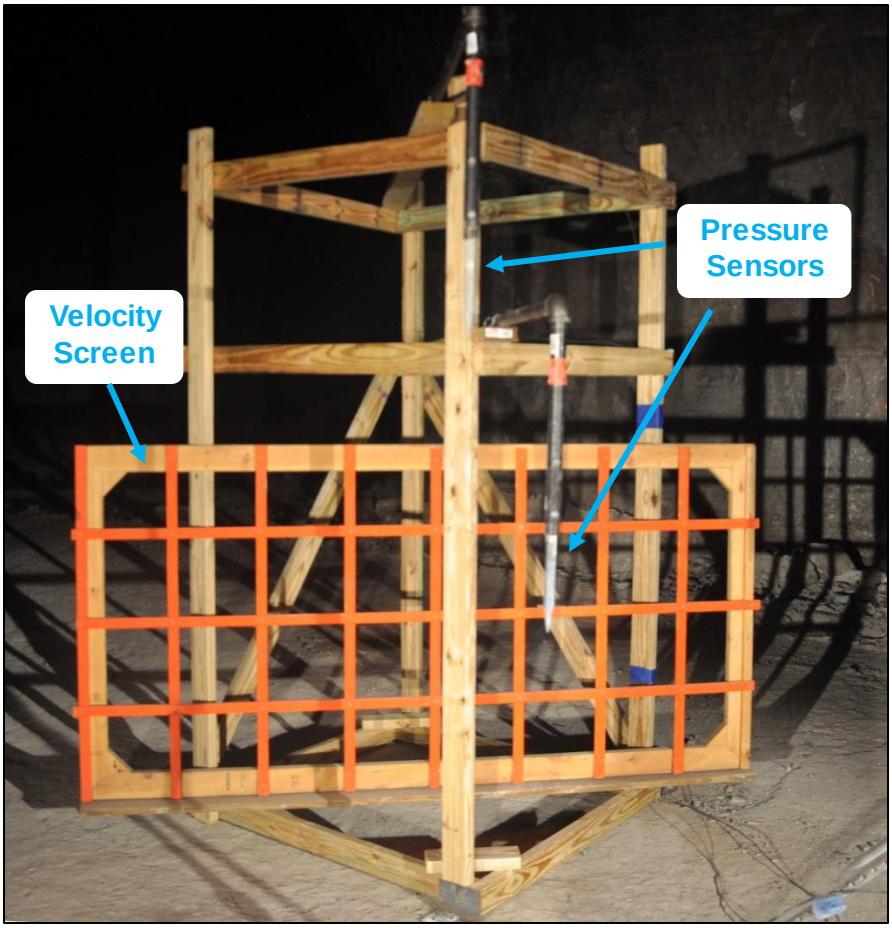

Figure 5.1: Free-field pencil sensor stand with attached velocity screen

Two film strain gauges were added to the setup as well. These gauges were adhered to the rock surface, following the manufacturer's recommendations in transverse and longitudinal orientations. The distance from the borehole to the center of these strain gauges was 1 foot. The two PCB strain sensors remained at 2 feet and 3 feet. The strain gauge setup is shown in Figure 5.2, with the film strain gauges highlighted by a yellow circle and the two PCB strain sensors highlighted by smaller red circles. Figure 5.3 illustrates the instrumentation setup in plan view.

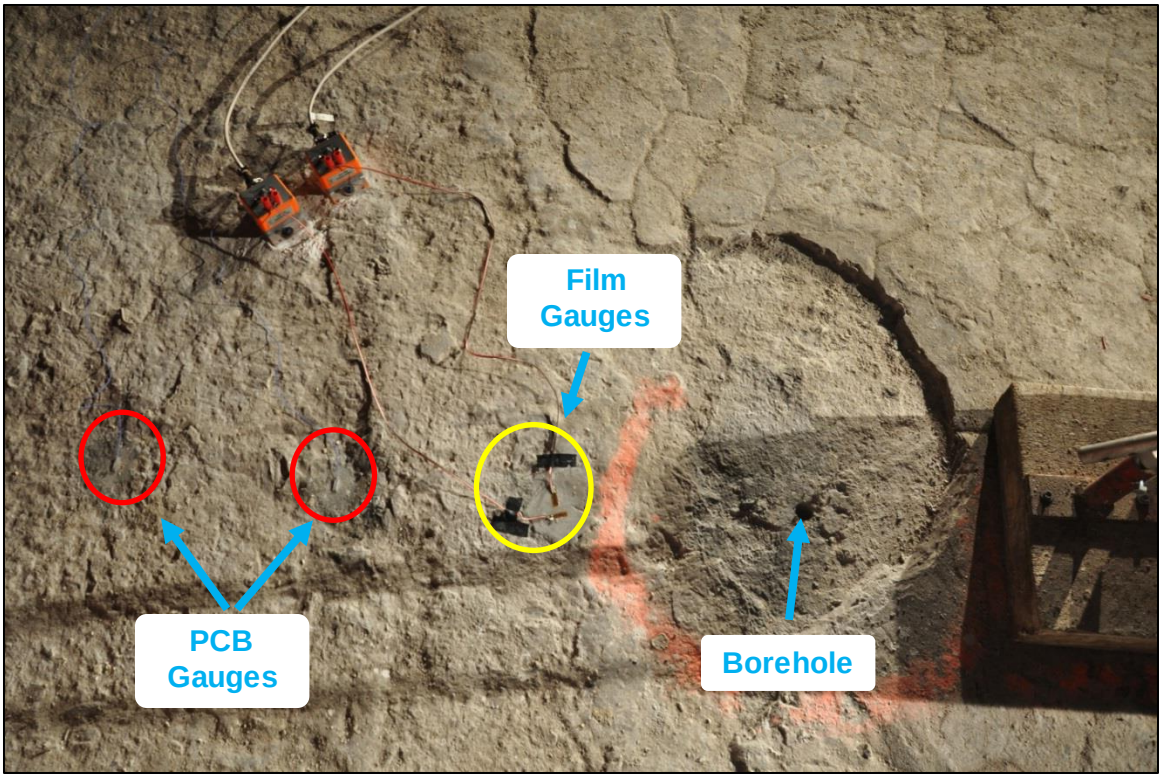

Figure 5.2: Strain gauge setup for stemming tests

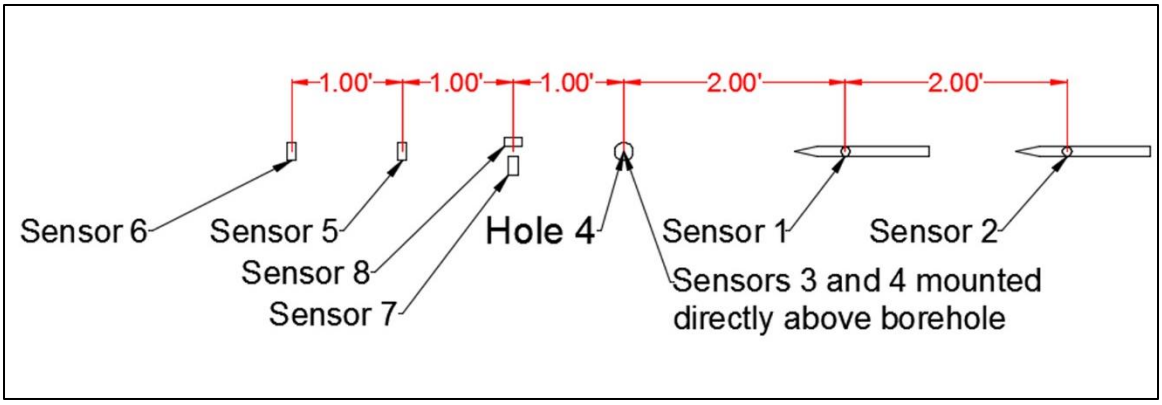

Figure 5.3: Plan view of sensor configuration for stemming tests

The seismograph was moved to a distance of 5 feet from the borehole to maintain a scaled distance of 50, consistent with the initial confined test series.

5.3 Explosive Charge

The first round of stemming tests (five tests) was conducted using 18 inches of 25 grain detonating cord cut into two, nine-inch lengths. This resulted in a charge weight of 0.0053 pounds. The detonating cord was initiated using an electric detonator. Following this round of tests, the charge size was increased to 16 inches of 50 grain detonating cord, cut into four, four-inch lengths for a charge weight of 0.0095 pounds (including detonator). This decision was made after reviewing the data from the first round of tests. On many instrumentation channels, the signal to noise ratio was very low, making it difficult to discern useable results from noise. By increasing the charge size, the magnitude of the results (strain, overpressure, and vibration values) was also increased. This improved the signal to noise ratio, facilitating data analysis and greater measurement accuracy. The charge size was not increased substantially, in order to prevent the explosive energy from overwhelming any differences that would otherwise be noticed between coupling/stemming combinations.

Referencing the published values, the total explosive energy expected for this test series is 28.83 kJ.

5.4 Stemming Test Results

A total of 18 stemming tests were conducted, three for each of the six coupling/stemming material combinations. The average values recorded for each of the combinations is summarized in Table 5.1. The performance of each combination will not be discussed in detail because that is beyond the scope of

this dissertation. Instead, this section will focus on the correlation between measured air overpressure and measured elastic deformation.

Strain gauges on channels 5-7 were positioned perpendicular to the borehole (transverse) and the strain gauge on channel 8 was positioned longitudinally. Analysis of the data from gauges closest to the borehole (7 and 8) indicated a flaw in the test methodology. Poisson's ratio was calculated to range from 0.78 to 1.04 (well above the upper limit of 0.5 and accepted values of 0.2-0.3 for limestone). These results are a strong indication that the strain gauges in close proximity to the borehole were not oriented correctly. This belief is that at distances less than one borehole length, the waves are propagating primarily in the vertical (Z) direction and are not accurately captured using surface mounted strain gauges. Additional tests in Chapter 6 support this belief.

Table 5.1: Summary of stemming test results

Sensor Number	**1 (2 ft)**	**2 (4 ft)**	**3 (4 ft)**	**4 (6 ft)**	**5 (2 ft)**	**6 (3 ft)**	**7 (1 ft)**	**8 (1 ft)**	**Seismo (5 ft)**
Coupling/Stemming Material	Pressure (PSI)				Strain (με)		Trans. (με)	Long. (με)	Acoustic (dB)
Sand/Cornstarch	0.89	0.49	1.74	1.13	12.88	2.88	172.45	186.75	139
Air/Sand	0.77	0.48	2.19	1.28	14.16	2.14	107.78	103.19	141
Sand	0.57	0.67	2.31	1.58	16.13	2.41	93.93	113.59	133
Cornstarch	0.28	0.32	0.36	0.40	54.25	10.75	125.88	161.34	130
Air	2.94	1.21	2.64	1.36	8.72	1.54	235.97	248.74	146
Cornstarch/Sand	0.08	0.13	0.08	0.08	43.69	19.36	--	--	NV

The data collected during this test series shows that the test methodology described provides a high enough fidelity to detect shifts in the air overpressure and elastic deformation balance. The air overpressure from sensors 1-4 and strain from sensors 5 and 6 are summed and compared. Strain data from

sensors 7 and 8 for the Cornstarch/Sand combination is not available, and therefore was not used for the other summations. Figure 5.4 shows the strong linear correlation (R^2 = 0.81) between the measured air overpressure and strain data. To further illustrate this correlation, data from the most distant pressure sensor (Sensor 4 at six feet above borehole) and strain sensor (Sensor 6 at three feet from borehole) are compared in Figure 5.5. This comparison results in a stronger linear correlation (R^2 =0.90). Appendix C contains the peak pressure and strain values for each of the 18 tests conducted.

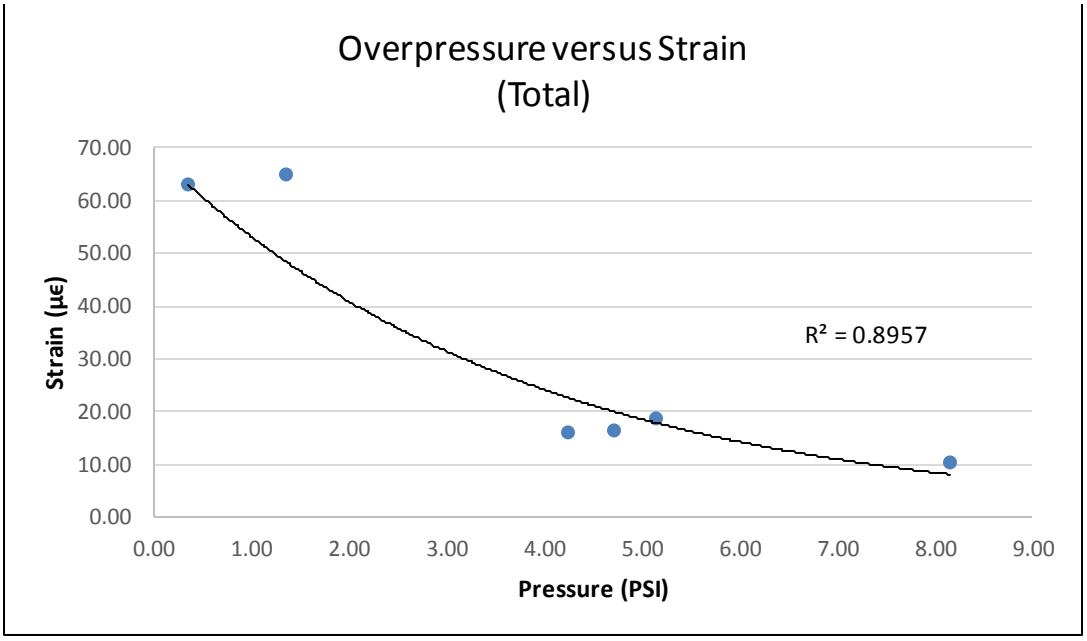

Figure 5.4: Air overpressure versus elastic deformation

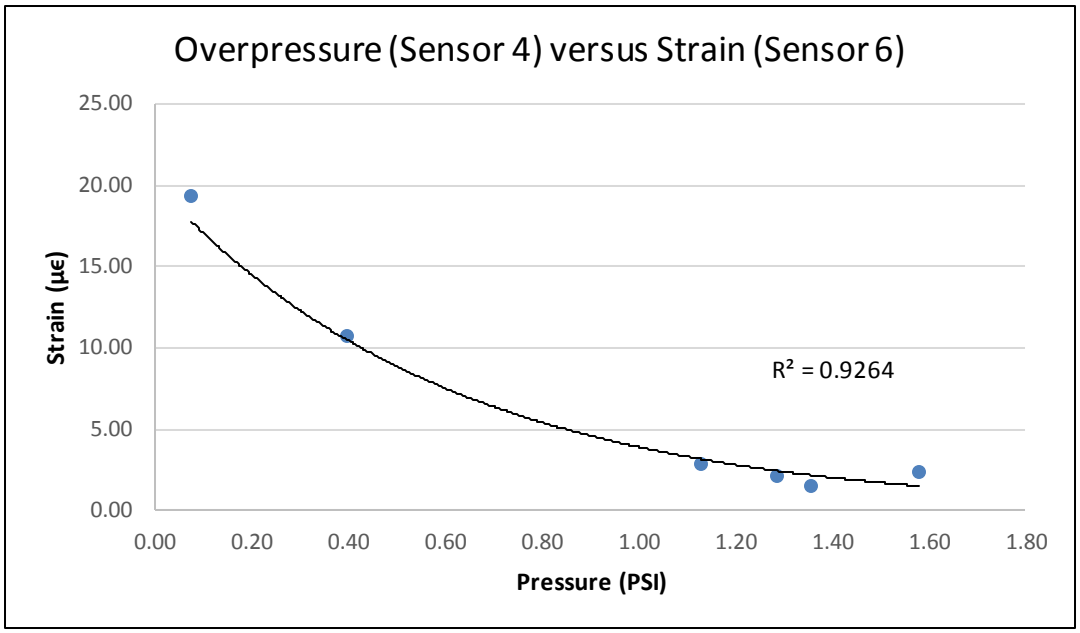

Figure 5.5: Air overpressure at sensor 4 versus strain measured at sensor 6

Comparison of air blast measured using the seismograph unit at five feet versus the strain recorded at sensors 5 and 6 does not show as strong of a correlation as previous comparisons. This is shown in Figure 5.6

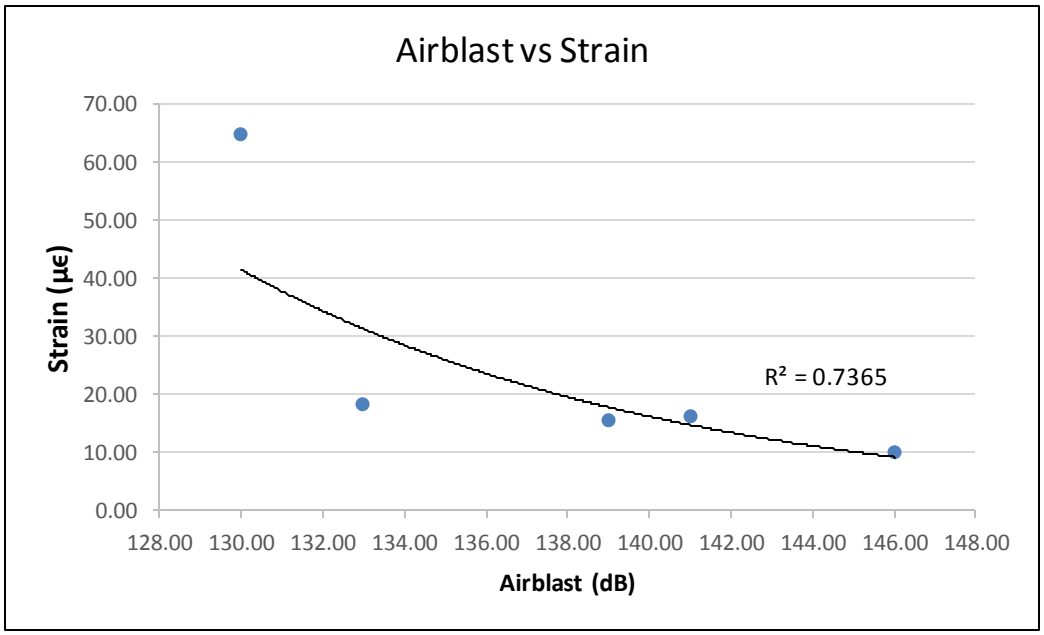

Figure 5.6: Air blast versus strain plot

Chapter 6. Strain Mapping and Strain Energy

6.1 Methodology & Instrumentation

Following the stemming test series previously completed, another test series was needed to determine at what distance the waves transition from propagating primarily in the vertical direction to propagating primarily in the axial (longitudinal) direction, making it acceptable to use surface mounted strain gauges for energy measurement. The instrumentation used for this test series was similar to the stemming tests, with the addition of two PCB strain gauges to the sensor array.

Following the extensive number of tests conducted using Hole 4, the decision was made to conduct the strain testing on Hole 3. Like Hole 4, Hole 3 was drilled in competent rock. Strain sensors were adhered to the rock surface at distances of 1 foot, 2 feet, 4 feet, and 6 feet from the center of the borehole. The sensors were first mounted transversely, and then after five test re-oriented longitudinally.

Free-field pencil sensors were again positioned at a 45 degree angle to the borehole and directly above the borehole. The high-speed camera, set at 500 frames per second, and velocity screen were used to determine stemming ejection velocity. Figure 6.1 shows this instrumentation setup. The orange hash marks on the rock floor demarcate 1 foot intervals, and the blue circles highlight the location of the PCB strain sensors. Figure 6.2 shows the setup in plan view.

Again, 16 inches of 50 grain detonating cord was initiated using an electric detonator, yielding a theoretical heat of detonation value of 28.83 kJ.

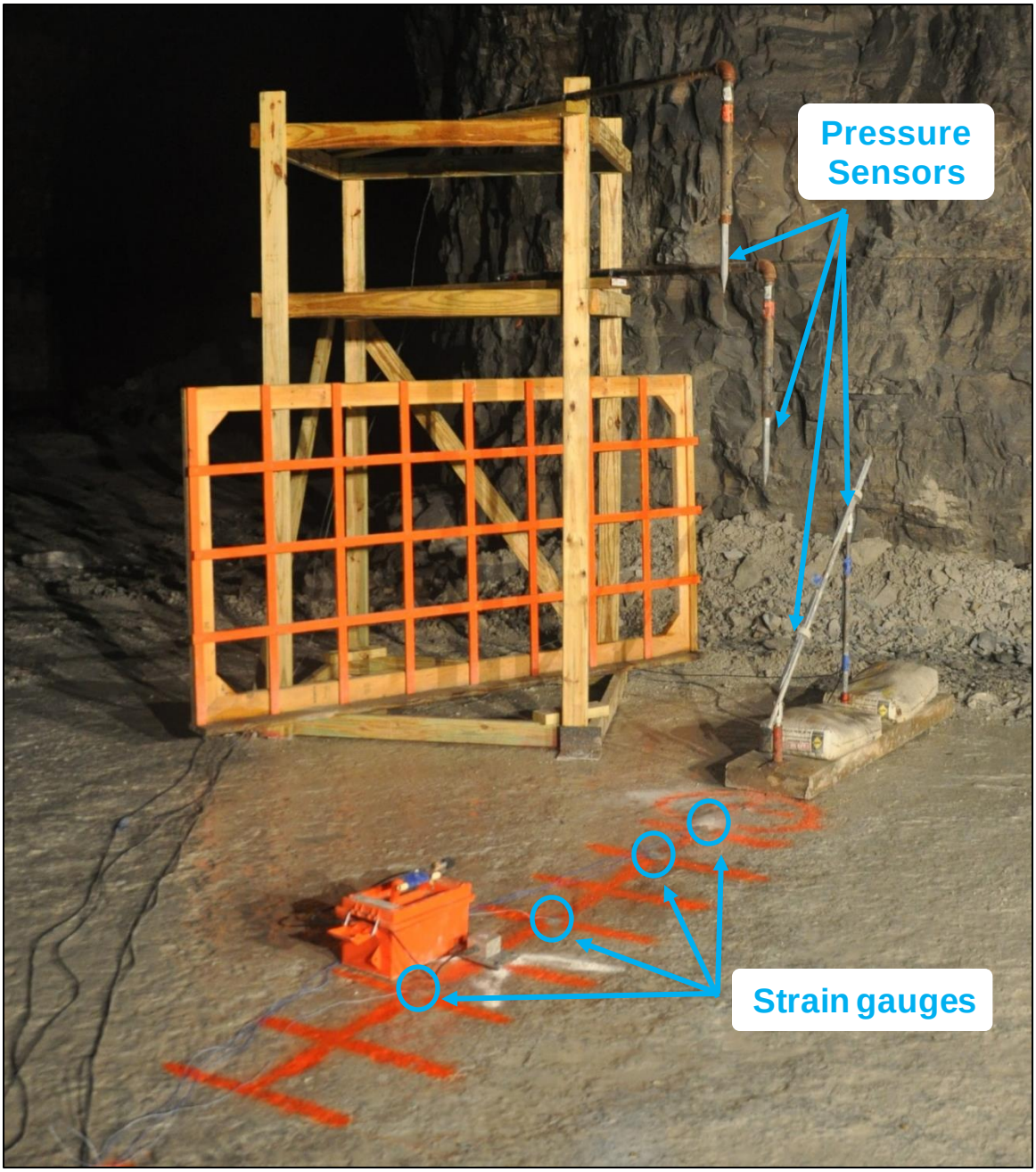

Figure 6.1: Instrumentation setup for strain mapping

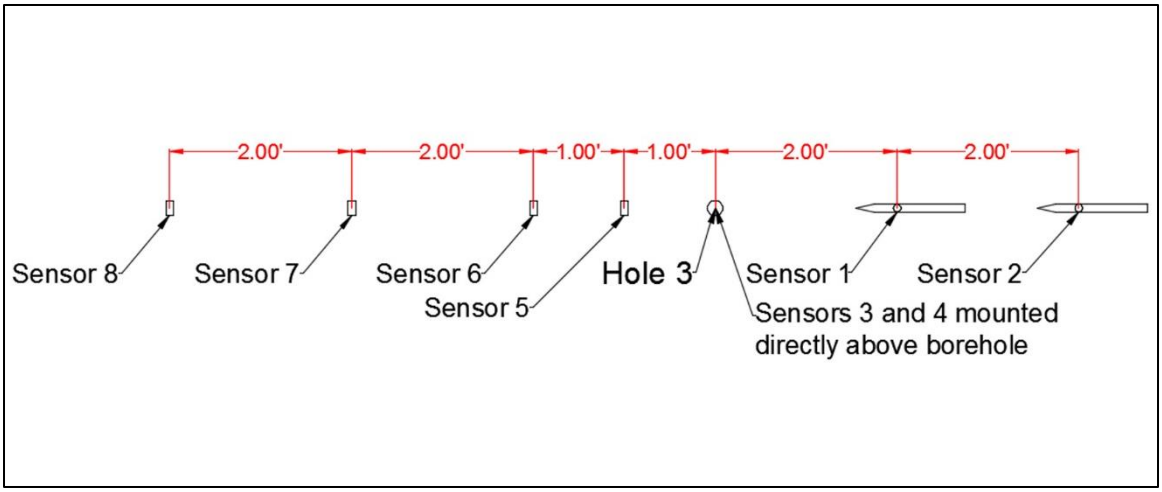

Figure 6.2: Plan view of strain mapping test setup

6.2 Strain Mapping Results

Five tests for each strain gauge orientation were conducted. The averages for each location and orientation are summarized in Table 6.1. The calculated Poisson's ratio for each location is also shown. Like the stemming test results in the previous chapter, the calculated ratio for the sensors closest to the borehole (1 ft. and 2 ft.) are well outside the conventional limit of 0.5. This is a strong indication that compression and tension waves are propagating primarily in the vertical direction at these distances. Poisson's ratio at the 4 ft. and 6 ft. points level out at reasonable values of 0.33 and 0.34, respectively. This indicates that the waves are moving primarily in the longitudinal direction. It should be noted that this is a dynamic reading and therefore, Poisson's ratio is expected to be higher than in static tests.

Table 6.1: Summary of strain mapping results

	Distance from Borehole			
Orientation	1 ft	2 ft	4 ft	6 ft
Transverse (με)	29.24	18.36	4.63	3.62
Longitudinal (με)	31.96	9.15	14.13	10.50
Poisson's Ratio	0.91	2.01	0.33	0.34

It is believed that close to the borehole, the waves are moving outward from the point of origin in a spherical manner and intersecting the rock surface (and strain gauges) at steep angles. As the waves continue to move outward, they become more planar and the interaction with the surface becomes shallower. At this point, the primary wave direction is more accurately captured by the longitudinal strain gauges. For this test series, the transition zone from spherical to planar takes place between 2 ft. and 4 ft. from the borehole. This idea is shown graphically in Figure 6.3. The magenta line is propagation and intersection of the wave as it reaches the strain gauge at a distance of 1 ft. from the borehole. This is followed by the red line at 2 ft., green line at 4 ft., and blue line at 6 ft.

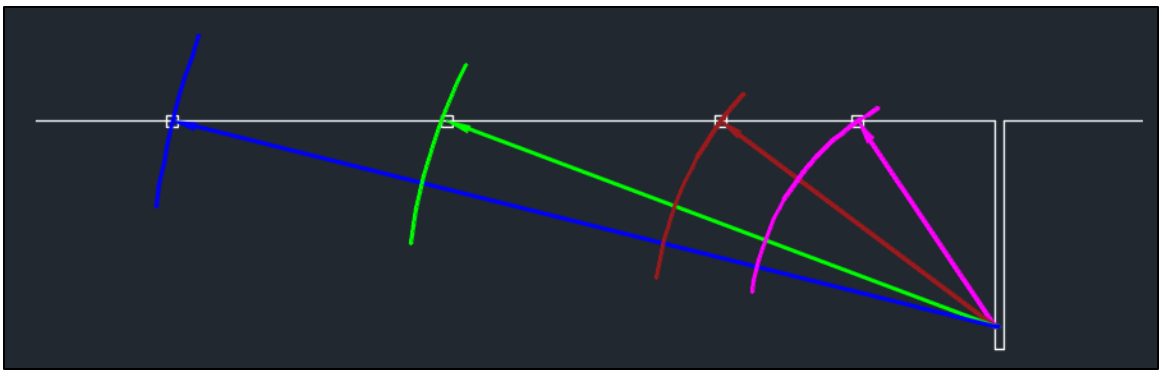

Figure 6.3: Shock waves intersecting strain gauges

With these findings in mind, the recommendation is made that for instrument mounting locations at a distance less than the borehole depth, the vertical component must be instrumented to accurately calculate the strain/ground vibration energy component. This can be accomplished one of two ways. The first is to use a triaxial accelerometer. The second method is to affix a strain gauge vertically to the side of a second borehole. For distances from the borehole exceeding the depth of the borehole, the use of strain gauges mounted transversely and longitudinally is advised. At these distances the vertical component can be estimated using basic solid mechanics principles.

The transverse strain measurements from each test were plotted with respect to distance to illustrate how strain decays with distance. Figure 6.4 illustrates the relationship between transverse strain measurement and distance. Strain is highest near the borehole and rapidly decays with distance, similar to air overpressure.

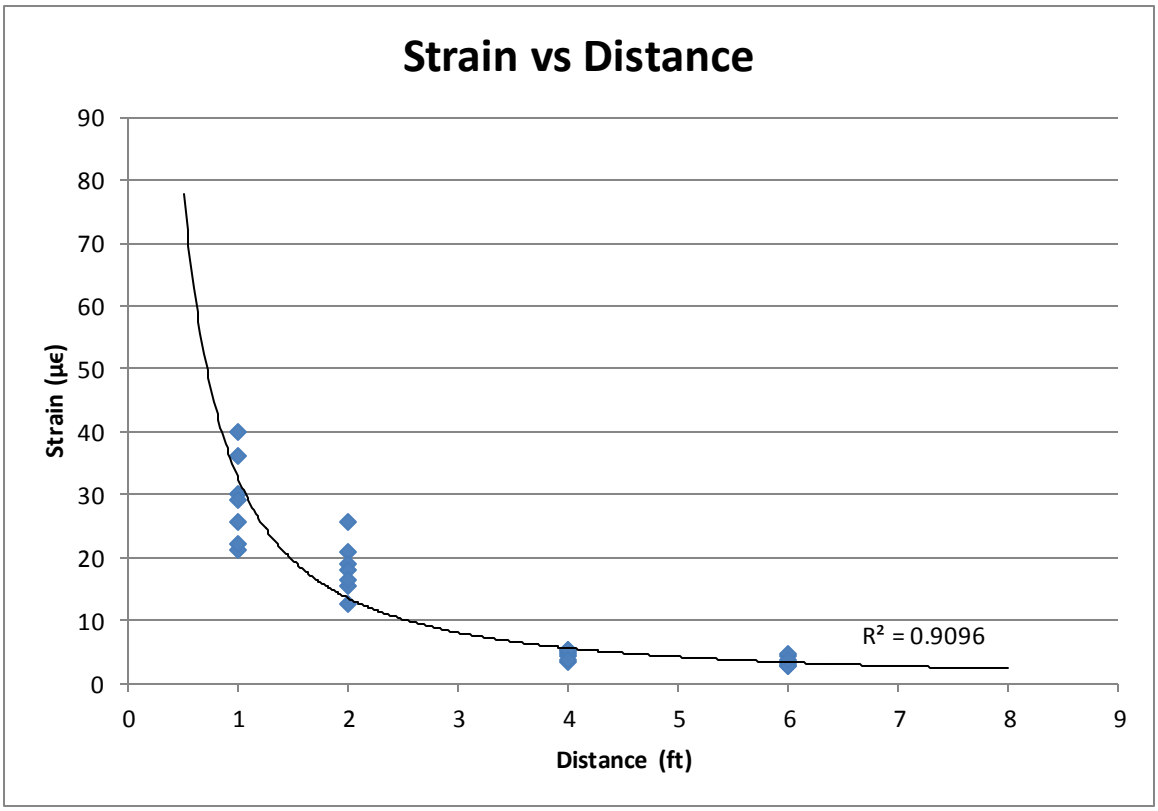

Figure 6.4: Strain with respect to distance from borehole

In addition to providing valuable data for mapping strain levels around the borehole, this test series also provided data that can be used for calculating energy lost to strain, air overpressure, and stemming ejection. For each of the five tests with transversely mounted strain gauges, the maximum strain level was plotted and a "Power" trend line fitted, similar to Figure 6.2. From this, the strain level at any distance could be estimated.

Strain energy is calculated using the following equation:

$$U = \frac{1}{2} V E \varepsilon^2 \tag{6.1}$$

where U is strain energy, V is volume, E is Young's Modulus, and ε is strain. For this Limestone material, Young's Modulus is 59.91 GPa and the dynamic

Poisson's ratio is 0.33, therefore the strain levels are assumed to be equal in the transverse and vertical directions and three times greater in the axial direction. The strain energy is assumed to propagate out from the borehole hemispherically. Therefore, the volume of rock affected by a given strain level is a hemispherical shell with an outer radius equal to the distance from the borehole to the point of interest and an inner radius equal to the distance from the borehole to the previous point of interest. Radii and their respective volumes from 0.1 ft. to 60 ft. were used for calculation of strain energy. The energies from each affected volume was summed and tabulated in Table 6.2.

Table 6.2: Summary of calculated strain energy for a confined borehole

Test	Transverse (J)	Axial (J)	Vertical (J)	Total (J)	Percentage of Total Energy
1	174.25	522.75	174.25	871.25	3.0%
2	111.16	333.48	111.16	555.8	1.9%
3	84.35	253.05	84.35	421.75	1.4%
4	232.01	696.03	232.01	1160.05	4.0%
5	91.47	274.41	91.47	457.35	1.6%

Strain energy values ranged from 456.35 J (1.6%) to 1160.05 J (4.0%) for individual tests. Using the values and resulting equation presented in Figure 6.4, the average strain energy for the entire test series is 514.74 J or 1.8% of the total explosive energy available. The values used for completion of this calculation are shown in their entirety in Appendix D.

Air overpressure energy was calculated using the same methodology previously discussed in Chapter 4. Two energy calculations were made for each test. One

using the pressures and wave velocities from the sensors mounted at a 45 degree angle, and the other using the data from the sensors mounted directly above the borehole. These energy values are shown in Table 6.3.

Table 6.3: Summary of air overpressure calculations for confined borehole

Side sensors					Top Sensors				
Test	Time Diff (ms)	Velocity (m/ms)	Surface Area (m^2)	Energy (kJ)	Test	Time Diff (ms)	Velocity (m/ms)	Surface Area (m^2)	Energy (kJ)
1	2.087	0.2920		2.466	1	1.771	0.3442		9.137
2	1.751	0.3481		1.084	2	1.781	0.3423		8.526
3	1.764	0.3456	2.335	1.022	3	1.789	0.3407	9.34	8.588
4	1.757	0.3470		0.914	4	1.760	0.3464		8.069
5	1.771	0.3442		1.429	5	1.731	0.3522		8.447

A significant portion of the air overpressure energy is being directed upward, rather than outward in a uniform hemispherical shape at the distances measured in these tests. This is supported by the higher wave velocities experienced at the sensors directly above the borehole and the gas cloud seen escaping the borehole after stemming ejection when reviewing the high-speed video data. Also, peak pressures seen at sensor 1 (2 ft. from borehole at 45 degree angle) and sensor 4 (6ft. directly above the borehole) were both around 0.5 psi. As a result, it would not be correct to equally weight the top and side values to find the average energy for each test. Instead, a weight of 25% will be assigned to the side and 75% to the top. Table 6.4 summarizes the weighted values. Figure 6.5 illustrates the predicted pressure shell shape in relationship to the borehole and pressure sensors.

Table 6.4: Weight total air overpressure energy for confined tests

Test	Side Weighted Energy - 25% (kJ)	Top Weighted Energy - 75% (kJ)	Total Energy (kJ)	Percentage of Total Available Energy
1	0.616	6.853	7.469	25.9
2	0.271	6.395	6.666	23.1
3	0.255	6.441	6.696	23.2
4	0.228	6.052	6.280	21.8
5	0.357	6.335	6.692	23.2

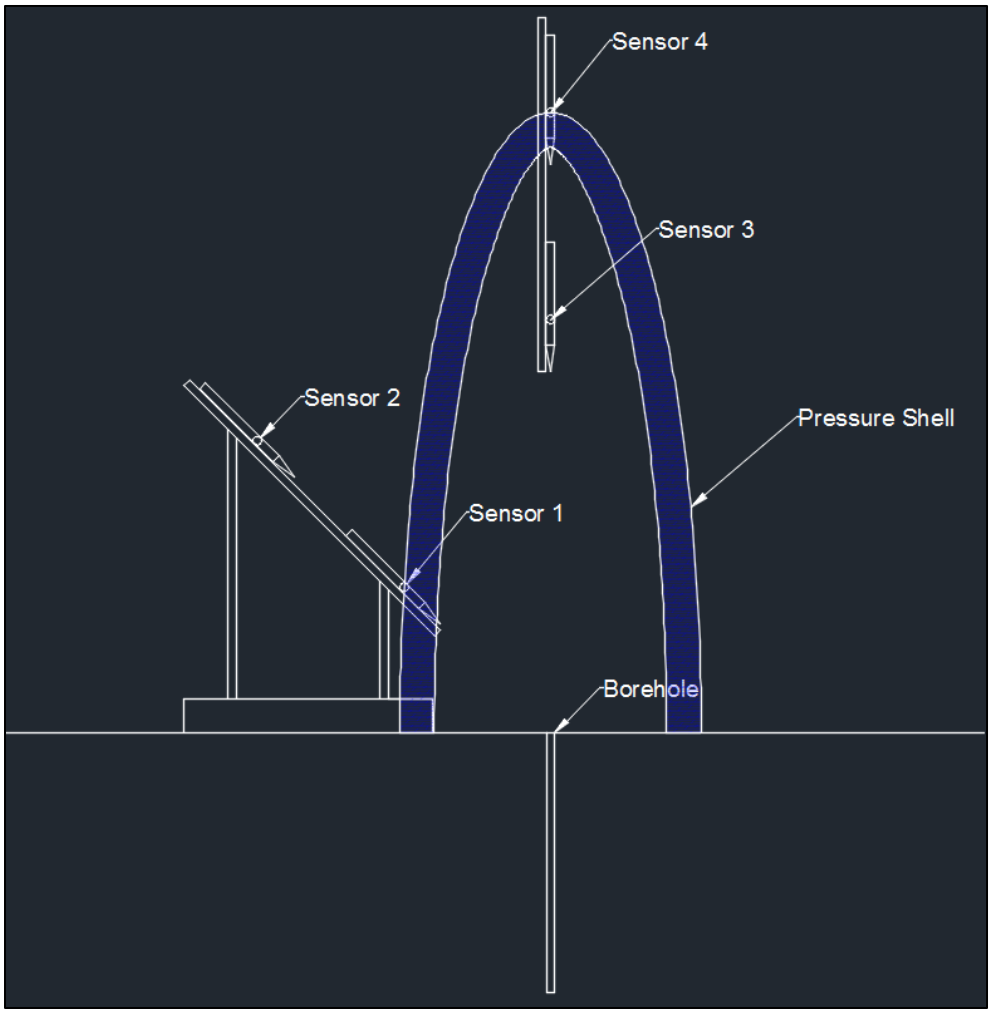

Figure 6.5: Revised pressure shell shape

Total air overpressure values were consistent using this methodology, ranging from 6280 J (21.8%) to 7469 J (25.9%). The overall average of the total energy lost to air overpressure is 6761 J or 23.5% of the total available explosive energy. Air overpressure energy plots for Tests 1-5 are presented in Appendix E.

Energy lost to stemming ejection was calculated using the basic physics equation:

$$KE = \frac{1}{2}mv^2 \tag{6.2}$$

Mass was taken as the mass of sand used to stem the hole during each test and velocity was calculated using high-speed video. The results of these calculations are show below in Table 6.5.

Table 6.5: Energy transferred to stemming ejection during confined test

Test	Velocity (m/s)	Mass (kg)	Energy (J)	Percentage of Total Energy
1	50.8	0.475	613	2.1
2	50.8	0.477	616	2.1
3	61	0.477	887	3.1
4	50.8	0.469	605	2.1
5	61	0.477	887	3.1

Calculated energy values ranged from 605 J (2.1%) to 887 J (3.1%). This amount of energy is significant considering the relatively small mass of the material being ejected.

The total amount of energy measured and the respective percentage of total available energy for each of the five tests is summarized below in Table 6.6.

Table 6.6: Total energy measured from confined borehole

Test	Deformation (J)	Air Overpressure (J)	Stemming Ejection (J)	Total (J)	Percentage of Total Energy
1	871	7469	613	8953	31.1
2	556	6666	616	7838	27.2
3	422	6969	887	8278	28.7
4	1160	6280	605	8045	27.9
5	457	6692	887	8036	27.9

Measured values ranged from 27.2% to 31.1% of the total, leaving over two thirds of the energy unaccounted for. A portion of this energy was lost to compaction of the sand stemming material. Following each test, a layer of very heavily compacted sand was left in the bottom half of the borehole. In many cases this layer could not be removed using compressed air or broken loose using a metal rod. Instead, the same hammer drill used to drill the holes had to be used to loosen the compacted material. A small amount of crushed limestone (fines) was also blown out of the hole after each test meaning some energy was lost to fragmentation.

More importantly, review of the high-speed video showed a significant amount of black gas escaping from the borehole after stemming ejection. This indicates that the reaction was oxygen deprived and the detonation was incomplete. Over the course of the block tests discussed in the next chapter, 58% of the total explosive energy was accounted for, versus the 28.5% accounted for in this test series. Colored gas was not evident during the block tests, meaning the

detonation was closer to ideal. Considering the same explosive products and similar test methodologies were used, the author believes that a considerable amount of the explosives total available energy was lost to incomplete detonation and not transferred to measureable components

Chapter 7. Concrete Block Testing

7.1 Methodology

The purpose of the concrete block testing was to reintroduce the fragmentation and movement components of energy partitioning into the test series. Concrete block testing more closely resembles scenarios typically encountered during rock blasting, by allowing the material to fragment towards three free-faces. The concrete blocks measured 4 feet in length, width, and height and were composed of a medium strength concrete mix containing no course aggregates.

Two blocks were available for testing purposes. For each test, a 7/8 inch hole was drilled to a depth of 10 inches with a burden of 10 inches from both side free faces. The first block was used for one test, and the second block was used for two tests, with holes being drilled and detonated on opposing corners.

7.2 Instrumentation

The same equipment used in previous tests was applied here also, but in a different configuration. In summary: a total of four PCB free-field pressure sensors, four PCB strain sensors, one MREL high-speed camera, one PCB signal conditioner, and one MREL data acquisition system were used.

Two PCB free-field pressure sensors were placed at a height of 4 feet and 6 feet, directly above the borehole, using the wood sensor tower (raised four feet using metal scaffolding). The two remaining pressure sensors were placed 2 feet and 4 feet from the side of the block to capture gases venting from fractures. Due to

the high probably of damage from flying debris, no sensors were placed directly in front of the block.

Strain sensors were adhered to the concrete block surface in 1 foot intervals. Prior to adhering sensors to the block, the surface was smoothed using an electric grinder and then lightly scuffed using sandpaper. After analyzing data from the first test, the decision was made to no longer place a sensor at 4 feet, due to abnormal readings. The abnormal readings were likely caused by the sensor's close proximity to the back corner of the block. This position resulted in significant reflection of the waves. Figure 7.1 shows the position of the strain sensors relative to the borehole collar.

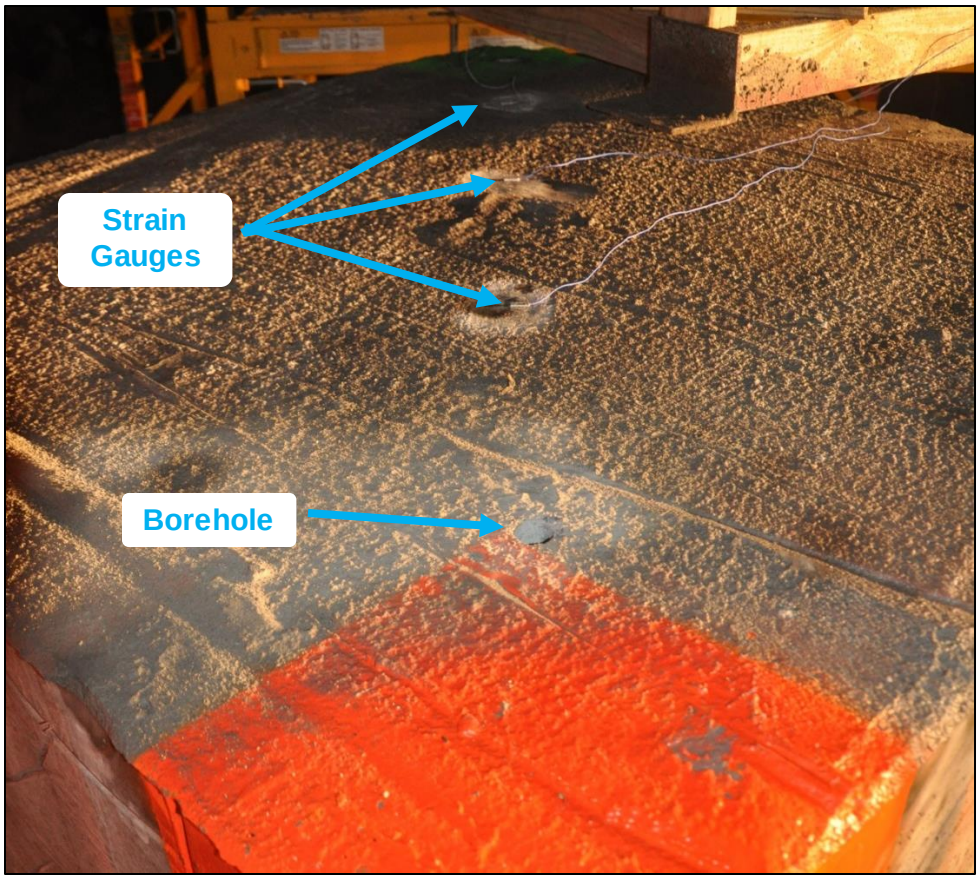

Figure 7.1: Strain sensor mounting locations

The velocity screen, containing a 1 foot by 1 foot grid, was placed parallel to the expected direction of fragment heave. The high speed camera was arranged perpendicular to the screen at a height of 4.5 feet. The corner of the block was painted with a grid and dots to aid in the tracking of fragments. Velocity screen positioning and the painted block corner are shown in Figure 7.2.

Figure 7.2: Velocity screen position for block testing

Figure 7.3 shows an overview of the testing setup, and Figure 7.4 shows the test setup in plan view.

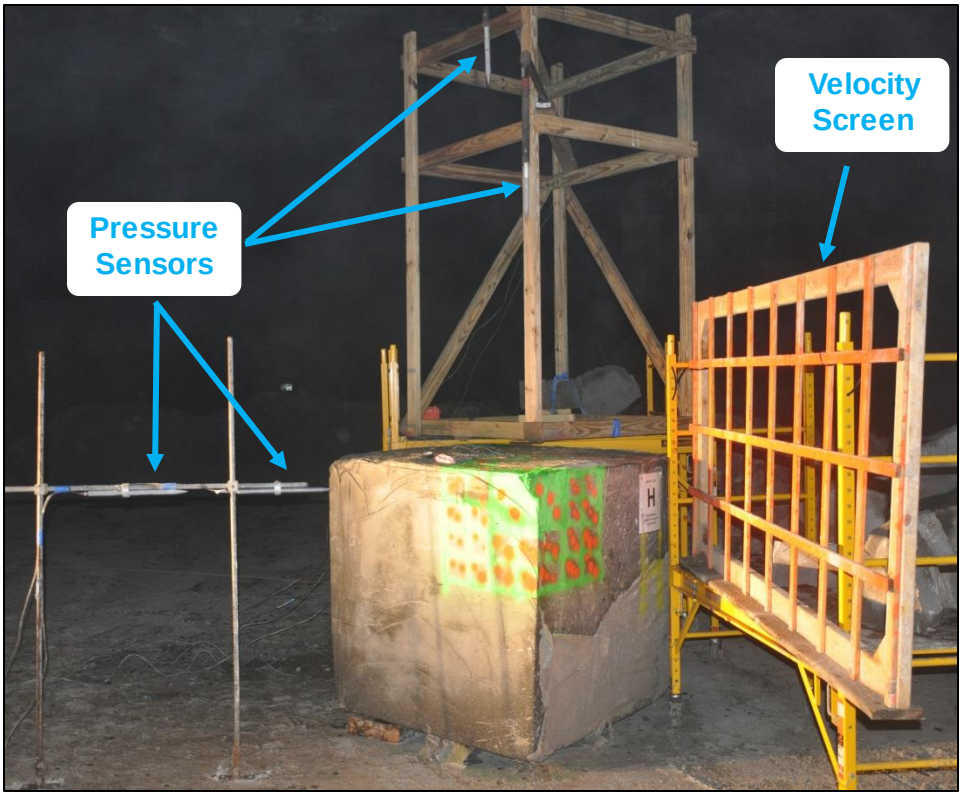

Figure 7.3: Overview of test setup for block testing

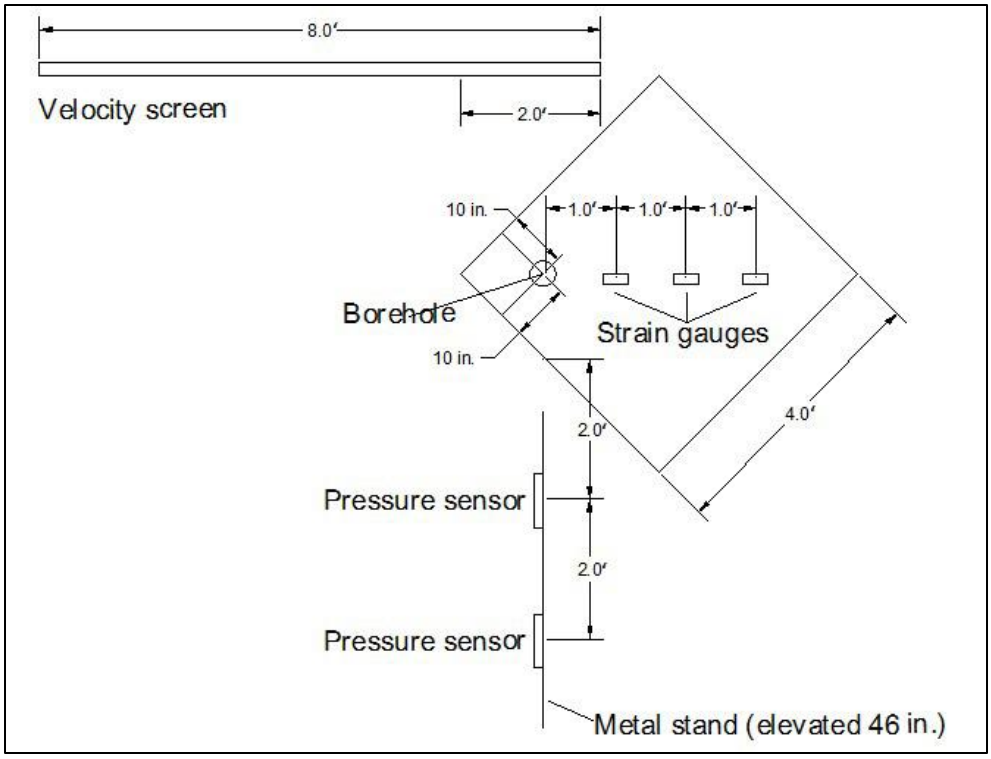

Figure 7.4: Plan view of block testing setup

7.3 Explosive Charge

The explosive charge remained consistent with the stemming and strain attenuation tests (four strands of 50 grain detonating cord cut to 4 inches in length) to allow for a direct comparison of energy component percentages. The borehole was 7/8 inch diameter and drilled to a depth of 10 inches for each of the three tests. The explosive charge was coupled with sand and then stemmed with 6 inches of sand.

The burden to both free faces and hole depth were chosen to be 10 inches to provide a powder factor of 0.5 lbs/yd^3. It was predicted that this powder factor would fragment the corner of the block without resulting in excessive material heave.

Referencing the published values, the total explosive energy expected for this test series is between 28.83 kJ.

7.4 Block Testing Results

7.4.1 Kinetic Energy

Kinetic energy of a moving fragment must be broken down into two components: translational kinetic energy and rotational kinetic energy. The determination of translation kinetic energy is straightforward and is found with the basic physics equation:

$$KE_{translational} = \frac{1}{2}mv^2 \tag{7.1}$$

where *m* is the mass of the object (kg) and *v* is velocity of the object (m/s). For these calculations, the mass of all sizeable fragments was recorded and summarized. Small fragments were placed in a bucket and weighed together. To account for the loss of fines and other unrecoverable fragments, 5% was added to the total weight. These results are summarized bellowed in Table 7.1. Test Blocks 1 and 3 had similar fragment masses of 125.00 kg and 117.21 kg, respectively. The mass of fragments from Test Block 2 was approximately 25% higher at 150.79 kg.

Table 7.1: Summary of fragment masses

	Fragment Mass (kg)		
Fragment Number	Block 1	Block 2	Block 3
Small	7.89	4.26	4.54
1	10.18	64.93	28.12
2	3.18	55.72	78.97
3	41.75	18.69	-
4	3.02	-	-
5	53.02	-	-
Total	119.05	143.61	111.63
Total * 1.05	125.00	150.79	117.21

The translational velocity of the fragments was calculated after reviewing the high speed video taken of each test. Each discernible fragment was tracked throughout the video and the number of frames it took for the center of the fragment to travel a distance of one foot was noted. All video was recorded at a rate of 500 frames per second, meaning that one frame was equivalent to a time of 2 milliseconds. With this information at hand, it was possible to calculate the fragment velocity in terms of feet per second (and then finally meters per second). There was little variability (±1 frame) in individual fragment velocity

within a given test. Therefore, it was possible to average the velocity of all the fragments to simplify the calculations. Both the average velocity and inflated total weight were used in the translational kinetic energy calculations. Table 7.2 summarizes the translational kinetic energy calculations. Figure 7.5 is a frame grab from the high speed video showing a large fragment from Test 1 as it moves past the velocity screen in the background.

Figure 7.5: Frame grab from high speed video

Table 7.2: Summary of Translational Kinetic Energy Calculations

Block	Mass (kg)	Velocity (m/s)	Translational Kinetic Energy (J)
1	125.00	5.08	1613
2	150.79	2.93	648
3	117.21	5.86	2014

Although block 3 had the lowest fragment mass, calculations showed that it had the highest amount of translational kinetic energy. Block 2 showed the opposite outcome, yielding the largest fragment mass, but the lowest velocity. As a result, block 2 possessed translational kinetic energy much lower than the other two tests.

Determination of the rotational kinetic energy for each test was not as straightforward. Unlike translational velocity which only requires two pieces of information that can be determined easily (mass and velocity), rotational kinetic energy requires the moment of inertia and angular velocity of each fragment. The formula used for calculating rotational kinetic energy is:

$$KE_{rotational} = \frac{1}{2} I\omega^2 \tag{7.2}$$

where I is moment of inertia about the rotational axis and ω is the angular velocity of the object. Due to the irregularity of the fragments in all three dimensions, hand calculation of the moment of inertia was impractical. Instead, fragments were transformed into a 3D point cloud using a Maptek laser scanner. This point cloud was meshed and imported into Creo 3D modeling software, where the moment of inertia for each fragment was calculated about its principal axes. A 3D rendering of the major fragments is shown in Figure 7.6. The output from Creo is shown in Figure 7.7.

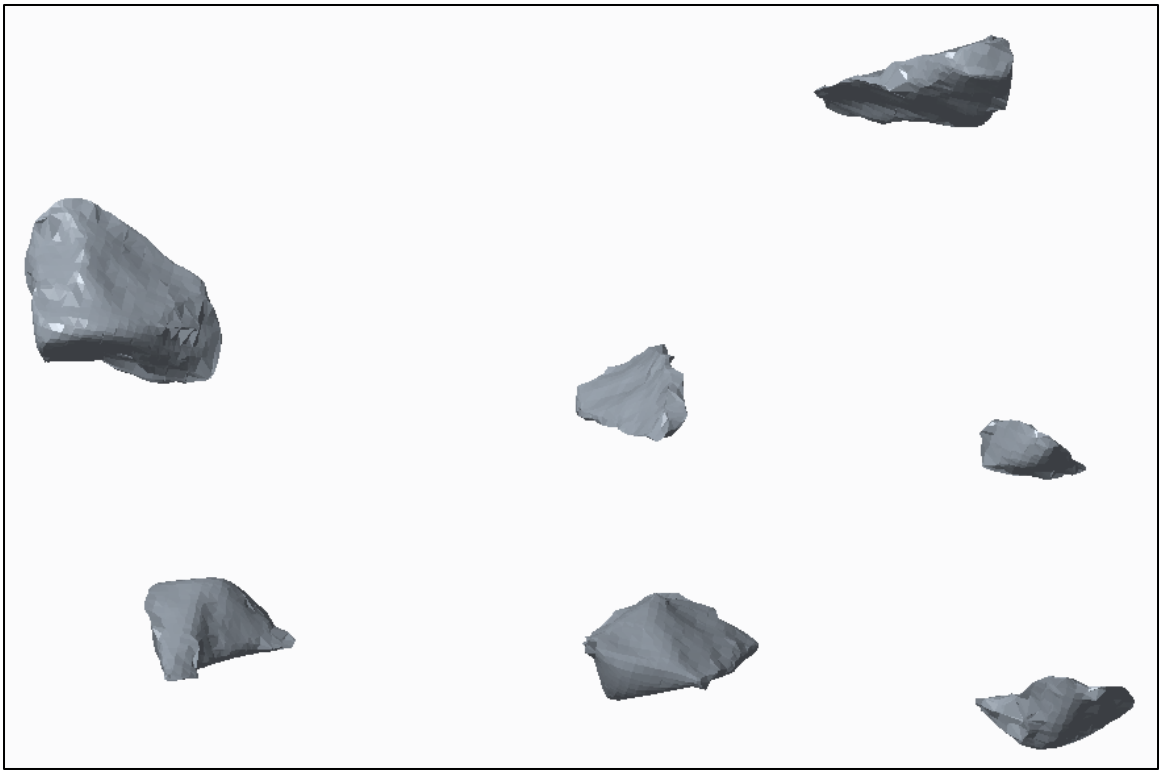

Figure 7.6: 3D rendering of major fragments

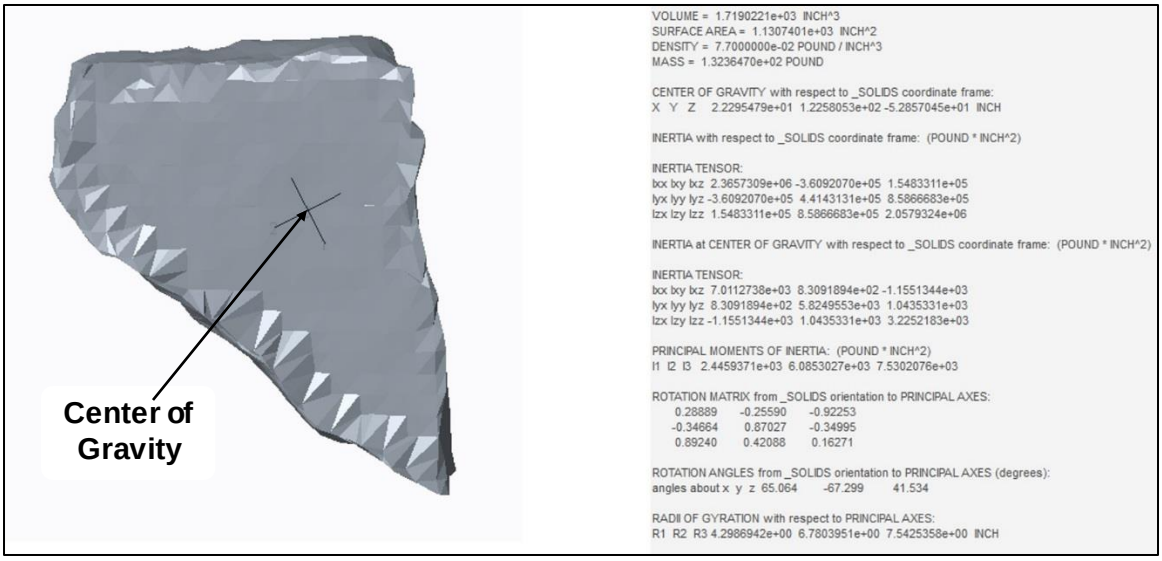

Figure 7.7: Detailed view of one major fragment and associated output from Creo

Without the aid of 3D motion tracking software, determination of angular velocity through the use a single high-speed video angle is subjective and inexact to an

extent. Like with any blast, the fragments in these tests tumbled about multiple axes, rather than rotating about a single axis. However, after carefully studying each high-speed video on a frame-by-frame basis the author feels confident that angular velocities presented are a good estimation of the true values.

In cases where a fragment was not rotating about a single primary axis, but rather between two primary axes, the average moment of inertia for these two axes was used in calculations. Tables 7.3 and 7.4 summarize the velocities, moments of inertia, and resulting rotational kinetic energy.

Table 7.3: Summary of Angular Velocities

	Angular Velocity (frames per 360)			Angular Velocity (radians / sec)		
Fragment #	Block 1	Block 2	Block 3	Block 1	Block 2	Block 3
1	216	376	184	133	76	156
2	--	468	320	--	49	89.5
3	400	164	--	72	112	--
4	--	--	--	--	--	--
5	300	--	--	95	--	--

Table 7.4: Summary of Moment of Inertia and Rotational Kinetic Energy

	Moment of Inertia (kg-m^2)			Rotational Kinetic Energy (J)		
Fragment #	Block 1	Block 2	Block 3	Block 1	Block 2	Block 3
1	0.0934	0.7155	0.3819*	821	4236	4629*
2	--	1.2449	1.6004	--	2332	6414
3	0.7819	0.0884	--	2005	1348	--
4	--	--	--	--	--	--
5	0.6792	--	--	3097	--	--

The moment of inertia and therefore rotational kinetic energy was not calculated for Fragments 2 and 4 from Block 1. Each of these fragments weighed less than 10 kg and were not easily trackable in the high speed video. Due to their relative

small mass it is assumed that their effect on the overall rotational kinetic energy is negligible. It should also be noted that Fragment 1 from Block 3 was sacrificed as part of the specific fracture energy determinations discussed in the next section. As a result, a 3D point cloud for this fragment was not created. Instead a rough approximation was created using 3D modeling software based on measurements gathered from studying the high-speed video. The moment of inertia for this model was used during calculations.

The rotational kinetic energy results follow the same basic trend as the translational kinetic energy with Block 3 having the highest energy results and Block 2 having the lowest. The total rotational energy for Block 1 was 5923 J or 21% of the total energy. Values for Blocks 2 and 3 were 7916 J (27.5%) and 11043 J (38.3%), respectively.

As is shown by these calculations, rotational kinetic energy represents a significant portion of the overall available energy and must not be ignored during future energy partitioning work.

In full-scale tests, it is probable that the translational kinetic energy to rotational kinetic energy balance will shift towards translational kinetic energy. With this test configuration, much of the energy was concentrated high in the block, which could significantly influence the rotation of the fragments. In full-scale testing the energy will be more evenly distributed about the test area, resulting in more translation and less rotation. Confinement of the material and timing sequence will also play a role in this balance and is discussed in the next chapter.

7.4.2 Fracture Energy

The biggest hurdle in calculating fracture energy is accurately determining the new surface area created. This holds true for full-scale blasts and for small-scale testing such as this. A number of different methods were used to calculate the new surface area for this testing. In each of the three tests, a large wedge shaped portion was broken off of the corner of the block, fragmenting into a number of pieces. The larger pieces were collected and the wedge was reassembled. The fracture lines were then labeled to prevent the same fracture plane from being measured twice. Figure 7.8 shows one of these wedges reassembled with the fractures labeled.

The surface area of each of these large fractures was measured as accurately as possible using a tape measure. To account for the surface roughness, the measured surface area was multiplied by an adjustment factor of 25%. Multiple fragments were spot checked using the Maptek 3D laser scanner and modeling software to ensure that the calculations completed using the tape measure and adjustment factor were accurate.

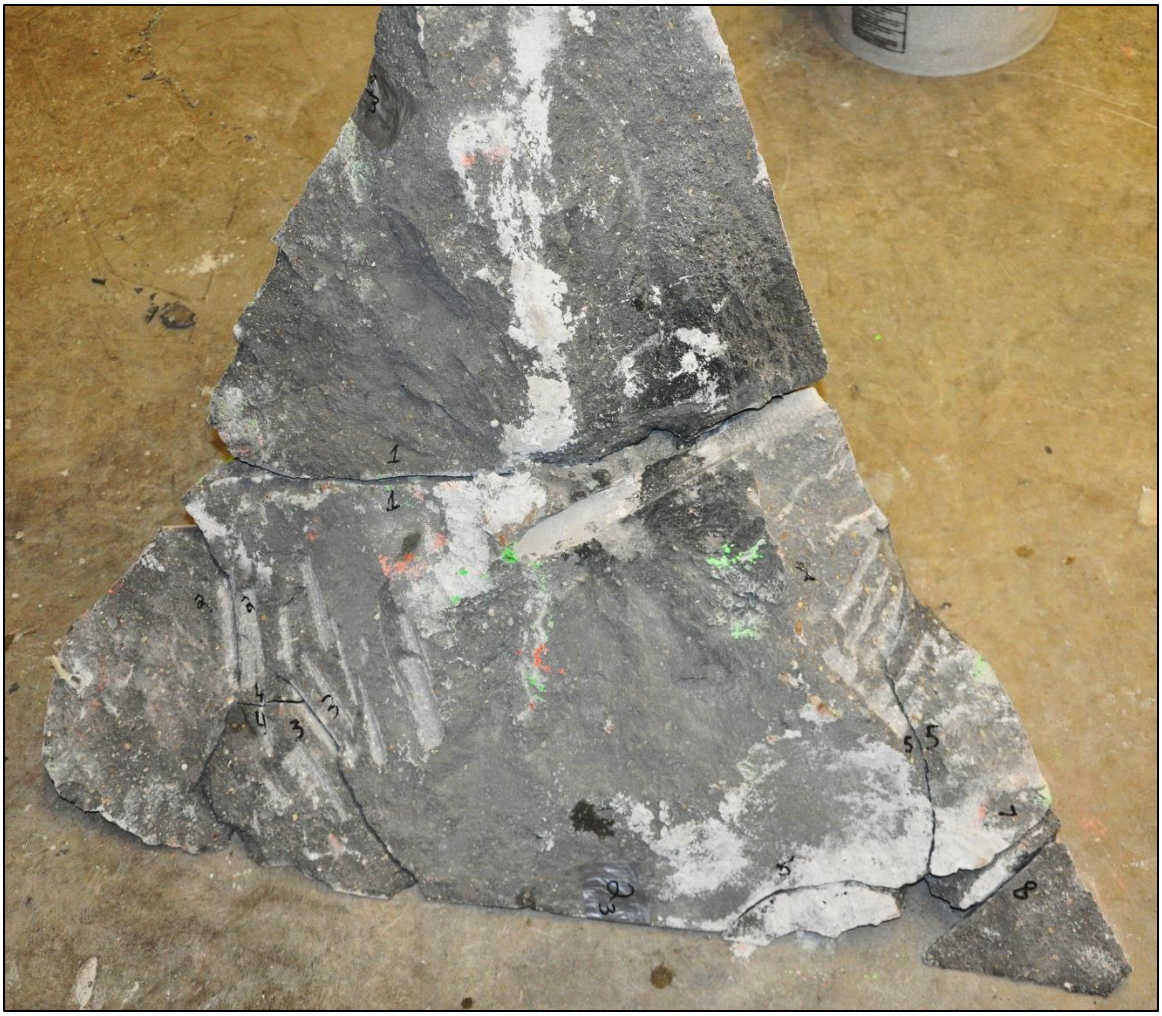

Figure 7.8: Fractured wedge reassembled with fractures labeled for measurement

Smaller fragments were spread out on a table for photographic analysis using WipFrag software. WipFrag is a commercially available fragmentation analysis software commonly used in the blasting industry to estimate particle size distribution within a muck pile. Using a standard tennis ball as a scale within each picture, the software was then used to determine the size of each particle. Figure 7.9 shows the small fragments collected from Test 2. The fines in the upper left-hand corner are a result of the fragments grinding against each other in a bucket and were not included in the surface area determination.

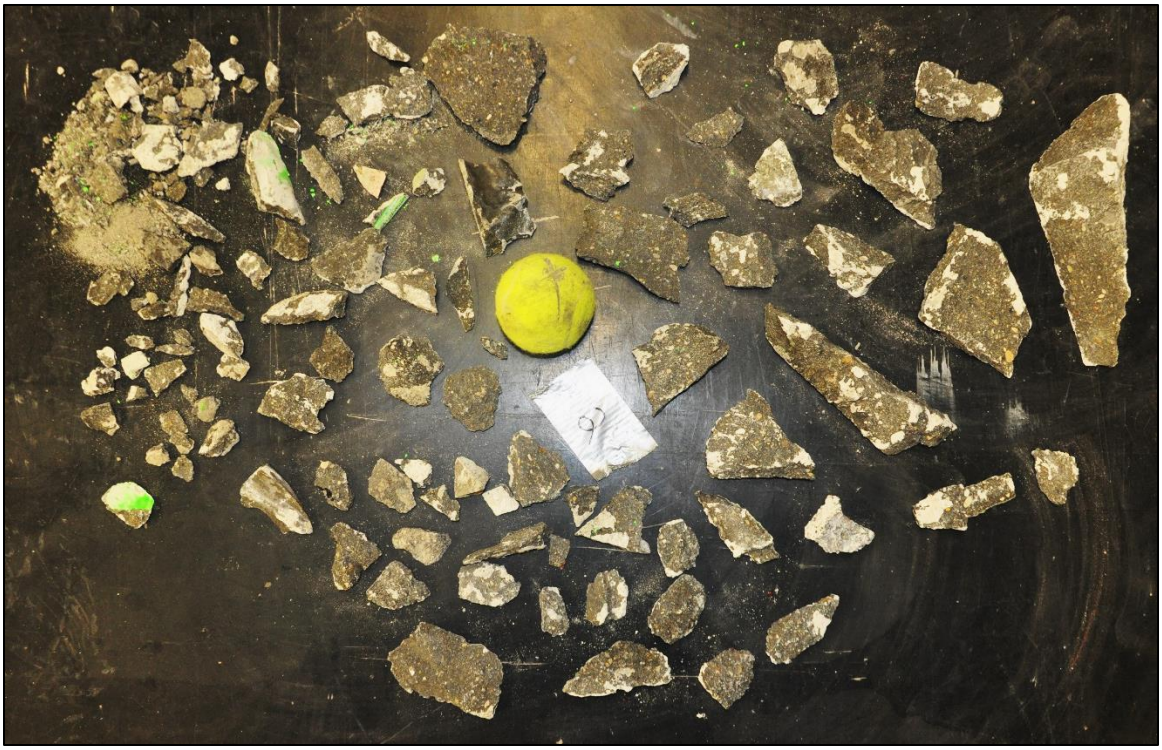

Figure 7.9: Small fragments from Test 2

Table 7.5: Summary of newly created surface area

Joint	Block 1 (in^2)	Block 2 (in^2)	Block 3 (in^2)
Wedge	2142	881	1050
1	152.5	14	110.25
2	45.5	117	38.5
3	20.25	214.75	26
4	92.5	23	9
5		21	18
6			17.5
7			13
8			13.5
9			22.75
10			6.5
Total	2452.75	1270.75	1325
Total*1.25	3066	1588	1656

The next piece of information required to determine energy partitioned to fragmentation is specific fracture energy. Use of the specific fracture energy was chosen over other methods such as the Rittinger coefficient used by Sanchidrian et al. (2007) because of the lack of fines and because it was possible to directly measure the new surface area created. Specific fracture energy is calculated using the following equation:

$$G_F = \frac{1}{(D-a)B}\int P d\delta \tag{7.3}$$

where G_F is specific fracture energy, D is depth of the sample beam, a is the starter notch depth, B is beam thickness, P is applied load, and δ is the displacement of the applied load.

To determine the specific fracture energy, multiple three-point bend tests were conducted on concrete samples. The test methodology took into consideration RILEM 50-FMC (1985) and ASTM C 293-02 (ASTM International, 2002) test standards as well as recent works published by Abdalla and Karihaloo (2003) and Karihallo et al. (2003). Six concrete beams with rectangular cross-sections of varying size were cut from the center of one of the larger fragments. ASTM C 293-02 (2002) recommends the depth of the sample be three times its span length for a standard three-point bend test and the RILEM (1982) document recommends the span be eight times its depth for samples with a maximum aggregate size less than 16mm. Revised recommendations by Karihallo et. al. (2003) suggest the sample span be four times greater than the depth. Based on these recommendations and the amount of intact material available, a span to

depth ratio of 3.5 was chosen. The starter notch in all samples was one half the depth. Table 7.6 summarizes the sample beam dimensions.

Table 7.6: Summary of beam dimensions for three-point bending tests

Sample	L (in)	B (in)	D (in)	a (in)	Span (in)
1	9.25	2.5	2.5	1.25	8.75
2	10.5	2.875	2.875	1.43	10
3	12	3.25	3.25	1.63	11.375
4	10.875	2.875	3	1.5	10.5
5	12	3.5	3.25	1.63	11.375
6	13	3.5	3.5	1.75	12.25

Each of the six samples were placed in a 300-ton compression testing machine outfitted with a three-point test apparatus. The samples were supported from the bottom at either end and loaded at mid-span from the top. This test setup is shown in Figure 7.10. The samples were loaded until a fracture extended from the starter notch to the upper most ligament and the sample was no longer able to resist any load. Figure 7.11 shows a fracture extending from the starter notch to the top of the beam just prior to complete failure.

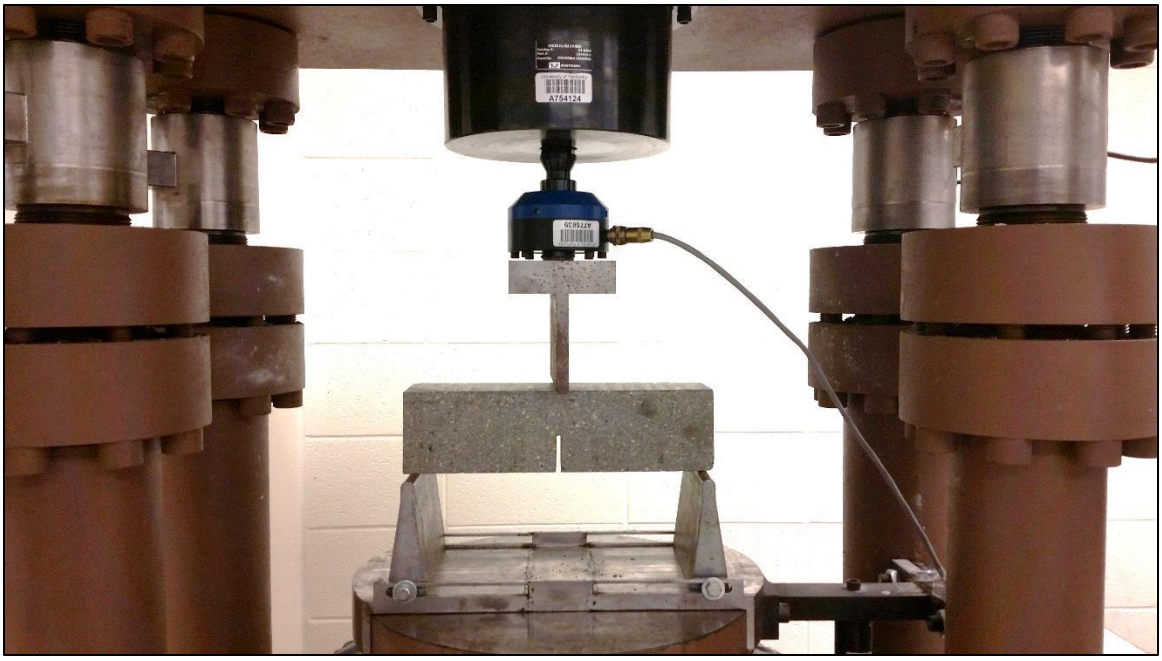

Figure 7.10: Three-point bending test setup

Figure 7.11: Sample beam with fracture extending from starter notch

For each test, a plot of the displacement versus measured applied load was created. This plot was integrated using DPlot and the maximum energy content

value found. One of these plots is shown in Figure 7.12. The plots for the other five sample can be found in Appendix G.

Table 7.7 provides a summary of the maximum sustained load for each sample, fracture area size, maximum energy content, and finally the energy required to create one square meter of new fracture area. In finding the average energy required to create new fracture area, results from Sample 1 were discarded. This sample was the smallest in size and showed small voids through the fracture plane which can explain the very low energy content value. Results from Sample 2-6 were used and an average energy of 74.30 J was found.

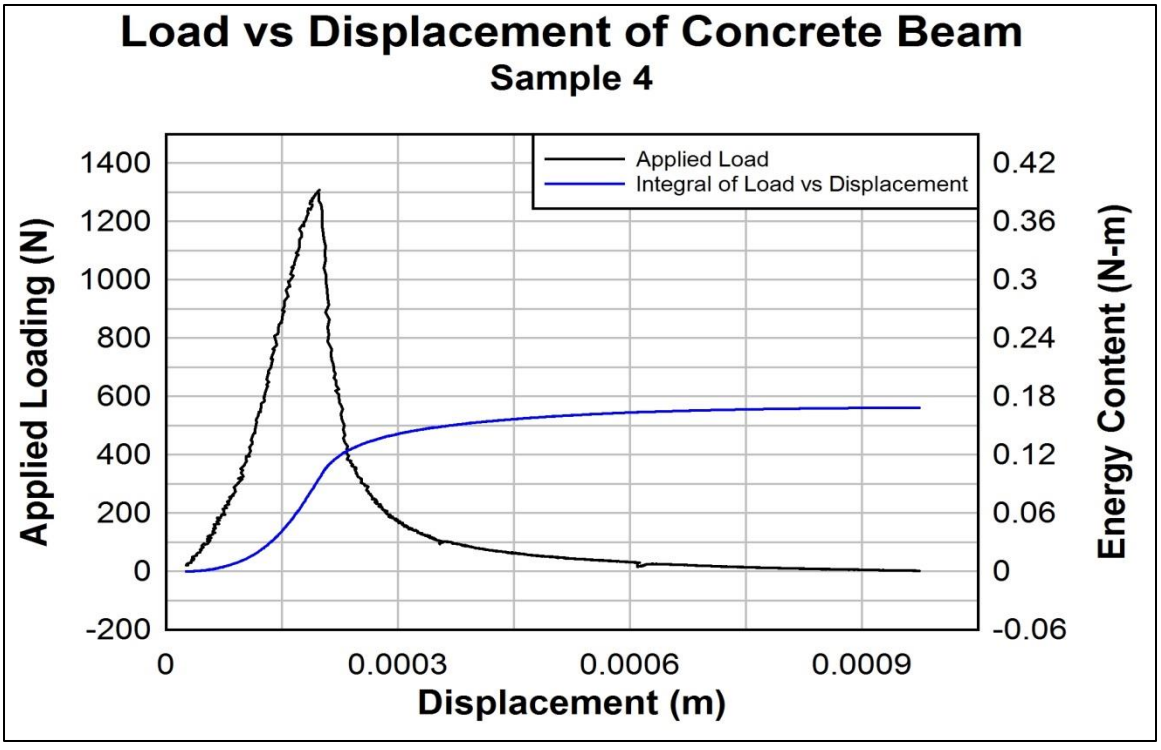

Figure 7.12: Load versus displacement for concrete beam sample

Table 7.7: Summary of specific fracture energy results

Sample	Max Load (lbf)	Fracture Area (in^2)	Fracture Area (m^2)	Energy Content (N-m)	Energy (J/m^2)
1	18.9	3.13	0.0020	0.0241	11.93
2	206	4.11	0.0027	0.1638	61.76
3	363	5.30	0.0034	0.3320	97.15
4	294	4.31	0.0028	0.1686	60.59
5	390	5.70	0.0037	0.2258	61.36
6	363	6.13	0.0040	0.3581	90.64

Table 7.8 summarizes the new surface area created during each of the three block tests along with the total portion of energy going to fracturing the block during the tests.

Table 7.8: Fracture energy determination for each block test

Test	New Surface Area (in^2)	New Surface Area (m^2)	Specific Fracture Energy (J/m^2)	Fracture Energy (J)
1	3066	1.978	74.30	147
2	1588	1.025		76
3	1656	1.069		79

Test block 1 had the largest amount of new surface area created at 1.98 m^2 and therefore saw the highest fracture energy component at 147 J. Test blocks 2 and 3 had roughly the same amount of new fracture area created and therefore similar fracture energy components of 76 J and 79 J, respectively. By comparison, fracture energy is small, ranging from 0.2% to 0.5% for this testing. These values are significantly lower than values reported by others. The cause

of this is not a result of the test methodology, but rather the configuration of the blast itself. It is expected that fractures will readily develop towards the free faces when there is little confinement, as is the case with this testing. Holes will more confinement will see fragmentation values higher than those recorded here.

7.4.3 Air Overpressure

Air overpressure energy for the block tests was calculated the same way for this test series as previous test series, with the exception of the surface area calculation. Rather than assuming the gases vented hemispherically from the borehole, the assumption was made that the gases vented along the primary fracture plane. This assumption was validated after reviewing high-speed video. In the video it was made clear by the dust being ejected from the top of the block and along the fracture lines on the side of the block, that gases were venting along the length of the fracture plane. Figure 7.13 is a frame grab from the high-speed video with the venting dust and gas highlighted within the blue ovals.

The primary fracture plane is the main fracture between the fragmented wedge portion and the remaining block. Figure 7.14 illustrates this primary fracture plane. The edge lengths (top, left side, and right side) of the fracture plane were measured for each block and multiplied by the edge length of an arch having a radius of curvature equal to the distance to the nearest pressure sensor (2 feet for the sides, and 4 feet for the top). This resulted in a pressure shell shaped like an arched tunnel along each fracture, rather than a single hemisphere. The primary fracture lengths and shell surface areas are summarized in Table 7.9.

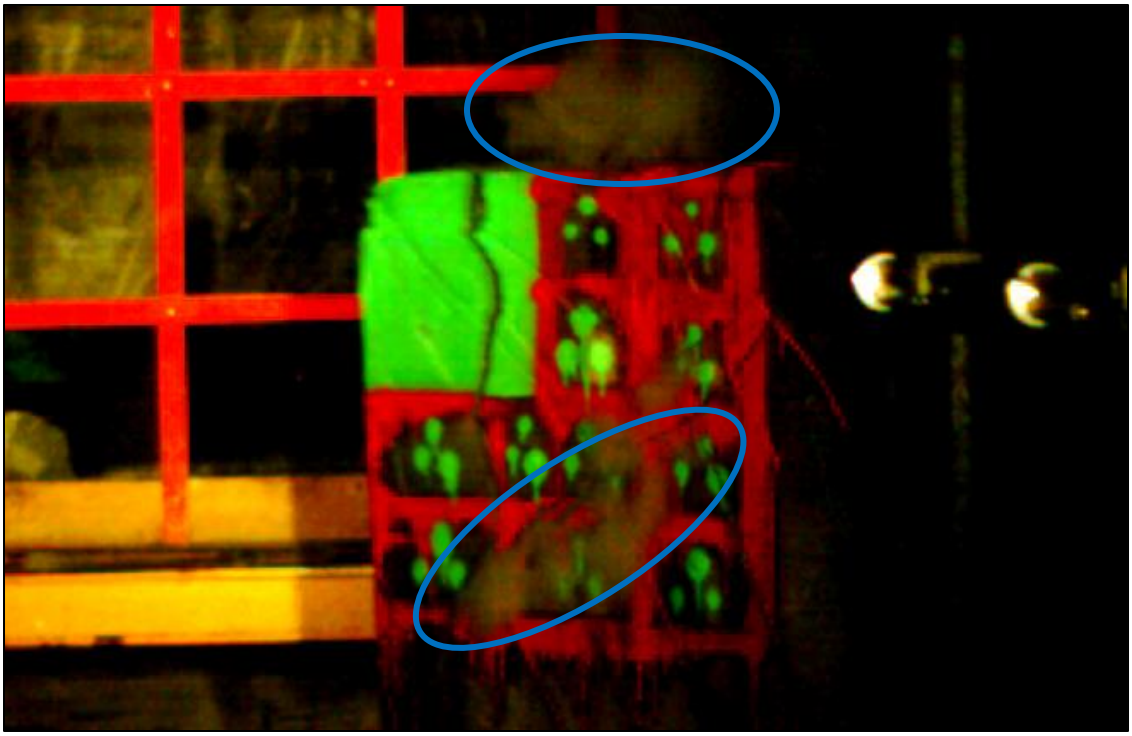

Figure 7.13: Dust and gases (highlighted) venting from primary fracture plane

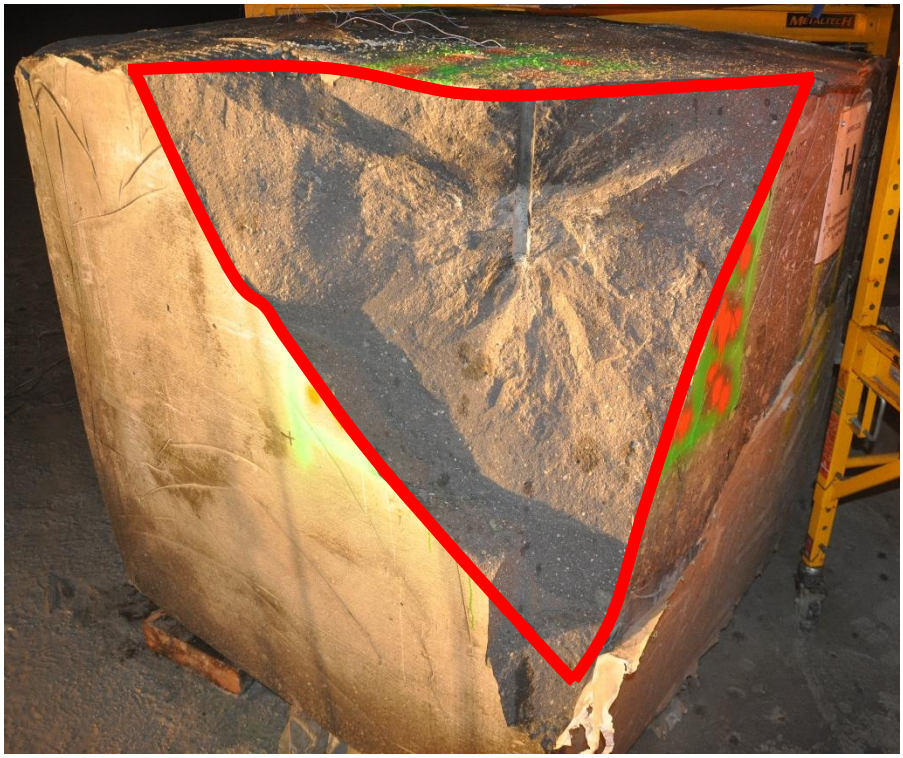

Figure 7.14: Primary fracture plane for block tests

Table 7.9: Block primary facture length and shell surface area

	Primary Fracture Lengths (in)		Surface Area of Shell (in^2)		Surface Area of Shell (m^2)	
Test	Top	Sides	Top	Sides	Top	Sides
1	34.0	61.5	10254	9274	6.62	5.98
2	41.0	92.0	12365	13873	7.39	8.59
3	39.0	75.5	11762	11385	7.59	7.35

Test 2 saw pressures significantly higher at all sensors in comparison to tests 1 and 3. This coupled with a primary fracture length of 133 inches, resulted in the total energy lost to air overpressure for test 2 equaling 11.62 kJ or 40.3% of the total available energy. The total energy lost to air overpressure for tests 1 and 3 was 8.151 kJ (28.3%) and 4.557 kJ (15.8%), respectively. Table 7.10 summarizes the pressure and peak pressure time of arrival (TOA) for each sensor along with the calculate wave velocity. Table 7.11 summarizes the values used for calculation of the air overpressure energy and the calculated air overpressure energy for each test.

Table 7.10: Summary of overpressure and wave velocity

	Sensor 1		Sensor 2		1 to 2
Test	Pressure (PSI)	TOA (ms)	Pressure (PSI)	TOA (ms)	Velocity (fps)
1	0.260	3.778	0.158	5.494	1166
2	0.787	3.640	0.554	5.402	1135
3	0.129	4.498	0.079	6.229	1155
	Sensor 3		Sensor 4		3 to 4
Test	Pressure (PSI)	TOA (ms)	Pressure (PSI)	TOA (ms)	Velocity (fps)
1	0.415	4.782	0.255	6.531	1144
2	1.576	4.163	0.875	5.894	1155
3	0.360	5.134	0.220	6.901	1132

Table 7.11: Calculated air overpressure energy

Test	Time Diff (ms)	Velocity (m/ms)	Top Area (m^2)	Top Energy (kJ)
1	1.749	0.3485	6.62	5.861
2	1.731	0.3522	7.39	7.825
3	1.767	0.3450	7.59	2.767
Test	Time Diff (ms)	Velocity (m/ms)	Side Area (m^2)	Side Energy (kJ)
1	1.716	0.3552	5.98	2.290
2	1.762	0.3460	8.56	3.799
3	1.731	0.3522	7.35	1.790

The average air overpressure energy for these tests was 8110 J or 28.1%. This value coincides well with the prediction made by Sanchidrian et al. (2007) of 30%.

7.4.4 Strain

Earlier chapters discussed the assumptions and care that must be taken to calculate strain energy using surface mounted strain gauges. Block tests introduce additional factors that must be considered. In the previous confined tests, the holes were drilled in massive limestone. Therefore, reflections were not an issue. In the case of these block tests, there were a total of six free faces in close proximity to the explosive charge and strain gauges. Extra care must be taken to isolate the primary wave values from the reflected wave values when analyzing the data. Due to the 4^{th} strain gauges close proximity to the back corner of the block (less than 6 inches), it was not possible to separate the primary wave values from the reflected wave value. The data from this sensor was not useable for analysis.

The data from the remaining three sensors is provides enough information to make a rough approximation of the strain energy for each test. Strain energy is again calculated using the following equation:

$$U = \frac{1}{2} V E \varepsilon^2 \tag{7.4}$$

where U is strain energy, V is volume, E is Young's Modulus, and ε is strain. For this approximation the Poisson's ratio is assumed to be 0.33, and therefore the strain levels are assumed to be equal in the transverse and z directions and three times greater in the axial direction. To determine the volume affected by a given strain level, the block was divided into three areas, one for each of the three strain gauges. Strain was assumed to be uniform throughout the depth of the block within each area. The volume influenced by values recorded at strain sensors 1 and 2 is 0.55 m^3 for each. The volume influenced by sensor 3 is 0.71 m^3. Based on laboratory tests, the Young's Modulus for the concrete is 15.18×10^9 N/m^2. Table 7.12 summarizes the maximum strain values recorded at each sensor location and energy calculated for the transverse component at that location. Finally Table 7.13 shows the transverse, axial, and vertical strain energy values, along with the total strain energy for each test.

Table 7.12: Summary of maximum transverse strain value and respective strain energy value

Strain Energy - Transverse Component							
Test	Strain 1 (με)	Energy 1 (J)	Strain 2 (με)	Energy 2 (J)	Strain 3 (με)	Energy 3 (J)	Total Energy (J)
1	46.34	8.97	36.90	5.69	31.35	5.30	19.95
2	41.37	7.15	36.30	5.50	29.87	4.81	17.46
3	39.28	6.44	32.72	4.47	26.43	3.77	14.68

Table 7.13: Strain energy values for block tests

Test	Transverse Energy (J)	Axial Energy (J)	Vertical Energy (J)	Total Energy (J)	Percentage of Total Available Energy
1	19.95	59.85	19.95	99.8	0.35
2	17.46	52.38	17.46	87.3	0.30
3	14.68	44.04	14.68	73.4	0.25

The strain energy is minimal for these block tests. Like the fragmentation energy, this is due to the nature of block testing and limited confinement, rather than the test methodology itself. Increased confinement would increase the total strain energy. This is shown clearly when comparing the values from these block tests to the values calculated in the confined test series. The average strain energy calculated during block testing was 86.8 J. The average strain energy calculated during the confined tests, using an identical charge, was eight times greater at 693.2 J.

7.5 Borehole Chambering

During each of the three block tests, the borehole was split vertically from top to bottom, leaving an intact cross-section in the un-fragmented portion of the block. This made measurement of the borehole chambering a straightforward process. The original borehole diameter was assumed to be constant at 0.880 inches from collar to bottom. The post-blast borehole was profiled in one inch increments from the collar to the bottom. The diameter of each of the boreholes remained constant for the first few inches before reaching the largest diameter 2 inches from the bottom of the borehole. This coincides with the midpoint of the 4 inch

explosive charge that was placed in the bottom of the borehole. Table 7.14 presents the borehole profiles along with the volume change for each hole.

Table 7.14: Block borehole chambering profiles

	Diameter (in)		
Depth (in)	Block 1	Block 2	Block 3
0	0.880	0.880	0.880
1	0.880	0.880	0.880
2	0.916	0.920	0.880
3	0.916	0.920	0.880
4	0.916	0.920	0.880
5	0.927	0.930	0.920
6	0.927	0.950	0.940
7	0.977	1.000	0.940
8	1.052	1.044	1.010
9	0.994	0.960	1.010
10	0.916	0.920	0.950
Volume Change (in^3)	0.8855	0.8983	0.8926
Volume Change (cm^3)	14.51	14.72	14.63

The volume change was consistent from block to block, ranging from 14.51 cm^3 to 14.72 cm^3. Unlike the borehole chambering tests conducted in massive limestone, the generalized assertion made by Ouchterlony et al. (2004) that 1 cm^3 change in volume requires 1 kJ of energy does not stand. The physical characteristics of the medium strength concrete used in this testing are considerably different than massive limestone. In addition to their generalized assertion, Ouchterlony et al. (2004) also stated that the cratering efficiency (the

energy required to increase the volume of the cavity) for rock is between 4.0 and 4.3 times its static unconfined compressive strength (UCS). The UCS of the concrete material used in this testing was 9059 psi or 0.0625 GPa. These test results can be found in Appendix F. Based on this information, the energy required to expand the borehole volume by 1 cm^3 is 0.25 kJ. Therefore, the energy transferred to borehole chambering in Block 1 was 3.638 kJ or 12.58% of the total available energy. Blocks 2 and 3 had similar results with 3.680 kJ (12.76%) and 3.658 kJ (12.61%) transferred to chambering, respectively.

7.6 Conclusions

Kinetic energy and air overpressure energy are the largest components in the energy partitioning equation. Based on the data collected, there is a direct correlation between kinetic energy and air overpressure. When air overpressure is lower, kinetic energy is higher and vice versa. Due to the limited number of fragments created during this testing, it is not possible to determine if there is a direct correlation between fragmentation energy and other components from this testing. The same can be said for strain energy. However, based on previous field experience, the author believes that as air overpressure energy increases, fragmentation and strain energies tend to decrease.

Table 7.15 summarizes the calculated values the energy partitioning components measured for each test along with the average value. Figures 7.15 – 7.17 summarize the data for blocks 1 – 3 as a percentage of the total explosive energy available, conservatively estimated to be 28.83 kJ. Figure 7.18 illustrates the average values from the three tests.

Table 7.15: Summary of calculated explosive energy partition values in Joules

	Block 1	Block 2	Block 3	Average
Translational	1613	648	2014	1425
Rotational	5923	4128	11042	7031
Fracture	114	59	61	78
Air overpressure	8151	11624	4557	8111
Strain	100	87	74	87
Borehole chambering	3638	3680	3658	3659
Unaccounted	9291	8604	7424	8439
Total	28830	28830	28830	28830

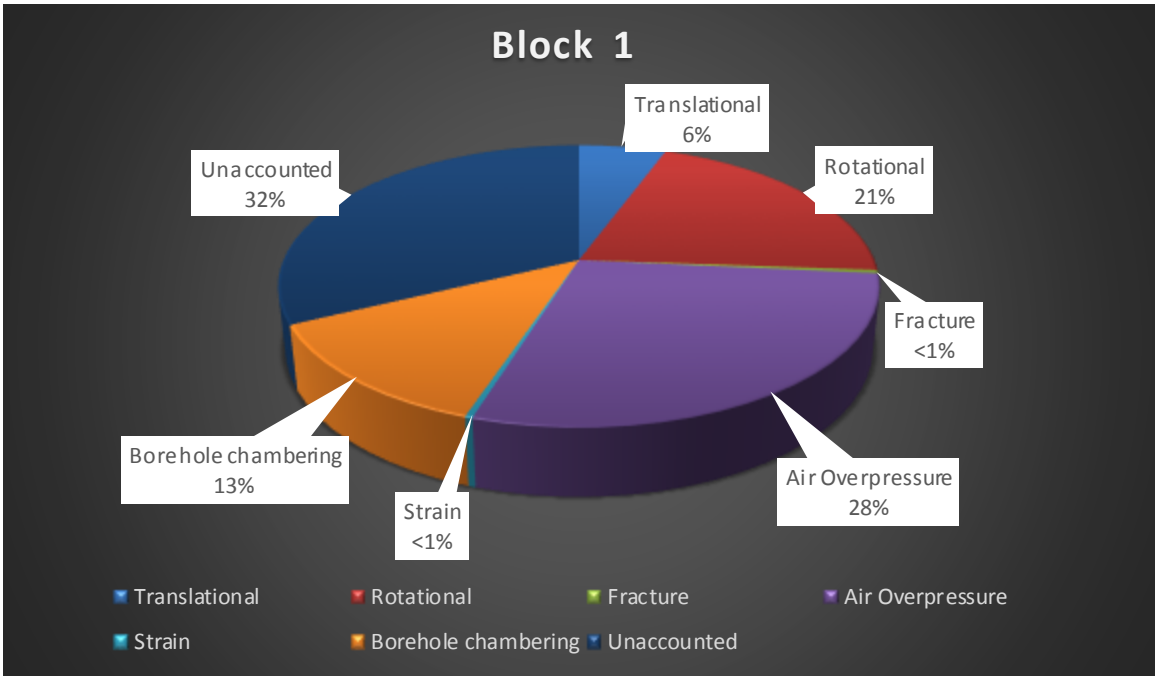

Figure 7.15: Summary of Block 1 energy partitioning percentages

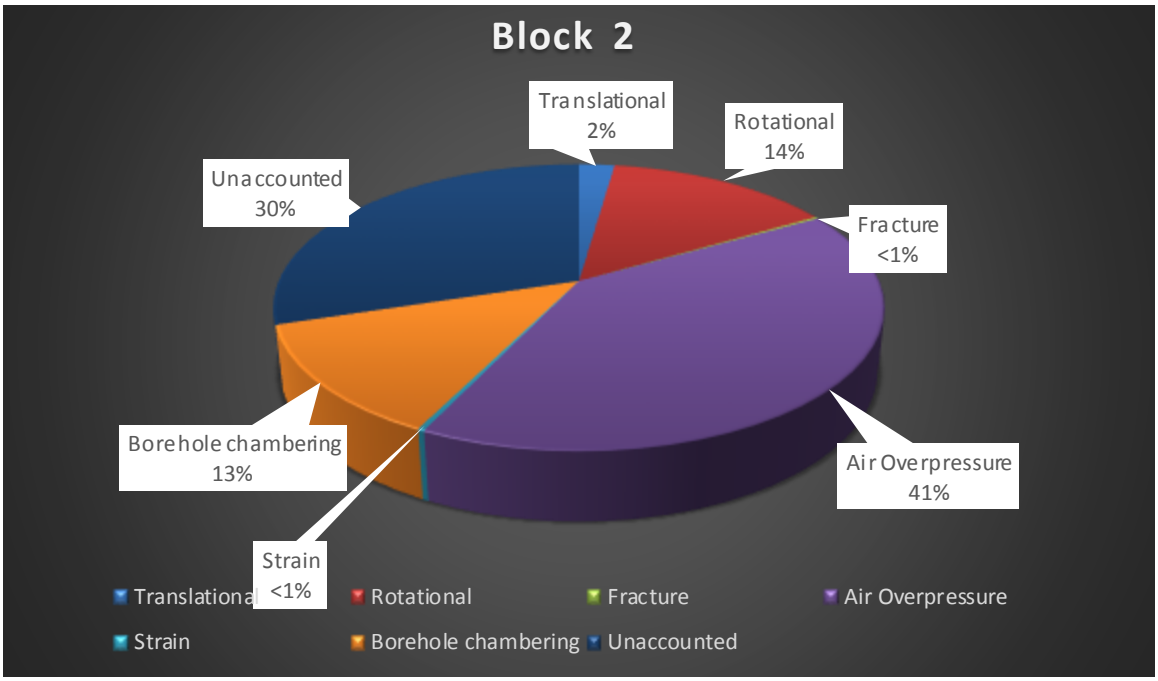

Figure 7.16: Summary of Block 2 energy partitioning percentages

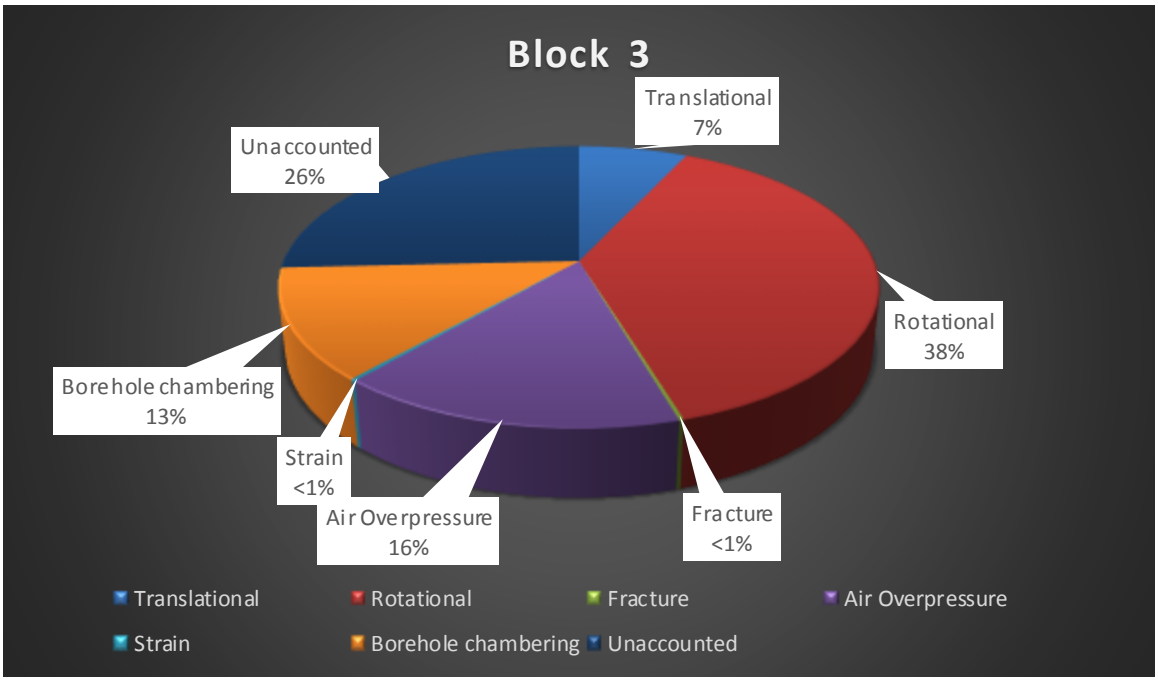

Figure 7.17: Summary of Block 3 energy partitioning percentages

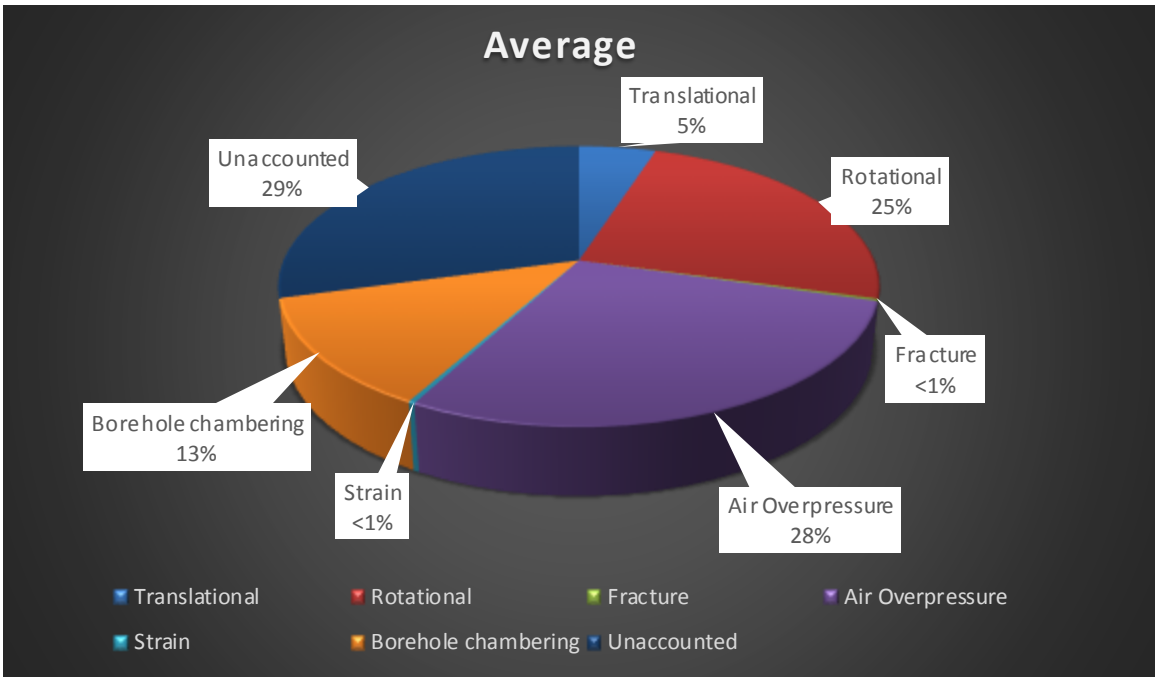

Figure 7.18: Summary of average energy partitioning percentages for block tests

These results show that slightly over one quarter (28%) of the total explosive energy was lost to air overpressure. Slightly less than one third of the energy was transmitted to kinetic energy (5% translational and 25% rotational). 13% of the energy was transferred to enlargement of the borehole. The remainder of the energy went into elastic deformation (<1%), fragmentation (<1%), or was not accounted for (39%). The portion not accounted for includes, but is not limited to: heat, fume formation, and micro-cracks.

Chapter 8. Goal Programming Framework

The primary objective of most mining operations is to minimize overall operating costs. It is important to optimize blasting practices because blasting directly effects all of the downstream processes include loading, hauling, and processing of the material. Generally, as drilling and blasting costs increase, loading, hauling, and processing costs decrease as a result of increased fragmentation. This generalization is based on site specific conditions and goals of the final use of the fragmented material.

Drilling and blasting costs are largely dependent on the parameters of the shot including burden, spacing, hole depth and diameter, and physical properties of the rock. These parameters dictate the amount of drilling and explosive product required. The type of explosive product and initiation system also effect the blasting cost. Loading costs are affected by fragmentation and heave. Material that is poorly fragmented and "tight" results in excessive equipment wear (both for the loaders and haul trucks) and digs slower. From a blasting perspective, haulage is most heavily affected by fragmentation. A decrease in mean particle size results in higher volume and tonnage per truck load. Site specific conditions such as haul road topography, haul distance, and maximum truck payload must also be considered. Like haulage costs, processing costs are most affected by fragmentation, but are very site specific and the end product must be taken into account.

Based on the conclusions reached in earlier chapters of this dissertation, a significant portion of the total explosive energy can be lost to air overpressure.

By decreasing the amount of energy lost to overpressure, more energy is shifted to other beneficial partitions, specifically: heave, and fragmentation. However, this shift may also send additional energy to ground vibration which must be balanced.

Air overpressure levels are a function of confinement and are primarily impacted by the amount of burden and the effectiveness of the stemming material. Rotational and translational kinetic energy are affected by the geometry of the shot (effective burden and timing). Slowing timing and lack of confinement will favor rotational kinetic energy. Faster timing and greater confinement will favor translational kinetic energy. Fragmentation and elastic deformation are influenced by burden, stemming effectiveness, physical properties of the rock, and timing sequence. Expansion of the borehole is controlled by confinement and physical properties of the rock. Energy lost to heat is assumed to be a property of the explosive and not influenced by the design of the blast in most cases. However, poor performance and low order detonation can occur with loss of confinement, resulting in less efficient use of the explosive energy and production of toxic byproducts. Energy not measured includes any components that currently cannot be accounted for including friction and fume creation.

A basic goal programming framework can be created with the objective of lowering overall operating costs. The framework must take into the factors just discussed. The objective function with respect to blast design and energy partitioning is therefore expressed as:

$$Min\ Z = C_d(B,S,H,D,RS) + C_b(W,P) + C_l(E_F,E_{TK}) + C_h(E_F) + C_m(E_F) \quad (8.1)$$

where $C_d$is drilling cost, C_b is blasting cost, C_l is loading cost, C_h is haulage cost, C_m is processing cost, B is burden, D is borehole diameter, H is borehole depth, S is spacing, T is stemming height, RS is rock strength, and TS is timing sequence

such that:

$$E_E = E_{AO}(B,T) + E_{RK}(B,TS) + E_{TK}(B,TS) + E_F(B,T,RS,TS) + E_{ED}(B,T,RS,TS) + E_{CE}(B,T,RS) + E_H + E_{NM} \quad (8.2)$$

E_E is total explosive heat of detonation which can be calculated from the explosive load, E_{AO} is air overpressure energy, E_{RK} is rotational kinetic energy, E_{TK} is translation kinetic energy, E_F is fragmentation energy, E_{ED} is elastic deformation, E_{CE} is cavity expansion, E_H is energy lost to heat, and $E_{NM}$is energy not measured.

Drilling and blasting costs are directly impacted by the shot layout. Tighter patterns result in higher costs because more holes are required to blast a given amount of material and the amount of explosive product increases. However, this increase in drilling and blasting cost can be more than offset by a decrease in downstream operating costs.

An example of this is shown in the powder factor comparison study conducted by the University of Kentucky Explosives Research Team. In this study, drilling and blasting costs increased by \$0.18/yd^3 after tightening the drill pattern from 26’ x 26’ to 22’ x 22’. This cost increase was caused by the need for more boreholes,

increased explosives consumption, and hauling in gravel to use as stemming material instead of drilling cuttings. The tighter pattern increased the total amount of explosive energy and the more effective stemming reduced air overpressure, resulting in improved fragmentation. The average particle size (D_{50}) decreased from 24” to 17”.

These changes decreased load cycle times and increased tonnage per truck load, allowing more material to be moved per shift. As a result, loading and haulage costs were decreased by \$0.21/yd^3, yielding a \$0.03/yd^3 decrease in overall operating costs. This study was conducted at an open-pit coal mine where the overburden was removed and taken to a dumpsite. Had this been a mine where the blasted material was processed further, additional cost savings would likely be noticed.

Improved performance can be seen through increasing the total amount explosive energy (i.e. increasing the powder factor by changing the shot layout). However, if the energy is partitioned poorly, a significant amount of the useful energy is going to wasteful byproducts. An alternative is to tailor the blast parameters and site conditions to better utilize the explosive energy available. This includes using best practices to stem the holes, cleaning up benches to prevent excessive toe burden, and selecting a timing sequence that results in acceptable fragmentation and heave, but limits ground vibration.

Chapter 9. Conclusions and Future Work

9.1 Conclusions

The focus of this dissertation was to further the understanding of explosive energy partitioning, through small-scale testing of various independent energy components. An innovative test methodology was constructed that has not been previously used in explosive energy partition testing. This methodology accounted for significantly more of the available energy than previous research efforts.

The confined borehole chambering test series values ranged from an average of 9.4% of the total explosive energy for the small PETN charge to 17.9% for the larger emulsion charge.

The stemming tests proved that different types of stemming do in fact affect the amount of energy transferred to air overpressure and elastic deformation components. When these two components were isolated, there was a definitive correlation between the two. As air overpressures increased, the measured strain levels decreased, and vice versa. Following the abnormal results recorded at the strain gauges nearest the borehole, additional strain mapping tests were conducted. During these tests, it was discovered that the tension and compression waves travel primarily in the vertical direction until they reach a distance greater than the borehole depth, making surface mounted strain gauges ineffective in this zone. Instead, surface mounted triaxial accelerometers or strain gauges mounted vertically in an adjacent borehole are recommended.

Outside of this zone, surface mounted strain gauges positioned transversely and longitudinally may be used to calculate strain energy. Using a strain attenuation curve developed during the strain mapping tests, the strain energy was calculated to be 2% of the total available explosive energy. Also during the course of these tests, black gases escaping the borehole were evident on the high-speed video, a sign of incomplete detonation. Only 28.5% of the total available energy was measured during this testing versus the 58% measured during the block testing using similar methodology. Therefore, the conclusion was reached that a substantial portion of the explosive energy was not transferred to measurable work due to incomplete detonation in this test series.

The concrete block tests reintroduced heave and fragmentation into the test matrix and sought to replicate a full-scale blast as closely as possible. During this test series values for air overpressure, rotational and translational kinetic, fragmentation, elastic deformation, and borehole chambering energies were calculated. It was determined that, although it has largely been ignored before, rotational kinetic energy can account for a significant portion of the total available energy; 25% in the case of this testing. During the concrete block testing, air overpressure energy was calculated at 28% of the available energy. This coincides closely with the prediction made by Sanchidrian et al. (2007) of 30%. The direct correlation between air overpressure and kinetic energy was clearly shown during this testing. As one component increased, the other decreased. Also, this testing showed increased confinement does have a significant impact on measured strain energy. Strain energy measured during the concrete block

tests was one sixth the value measured during the strain mapping tests. Finally, through this test series it was determined that borehole chambering accounts for 13% of the total available energy. This value falls within the range previously determined in the confined borehole chambering tests.

Figure 9.1 summarizes the values found for each of the components studied over the course of this research. In total, 71% of the explosive energy was accounted for. This is substantially more than previous research efforts.

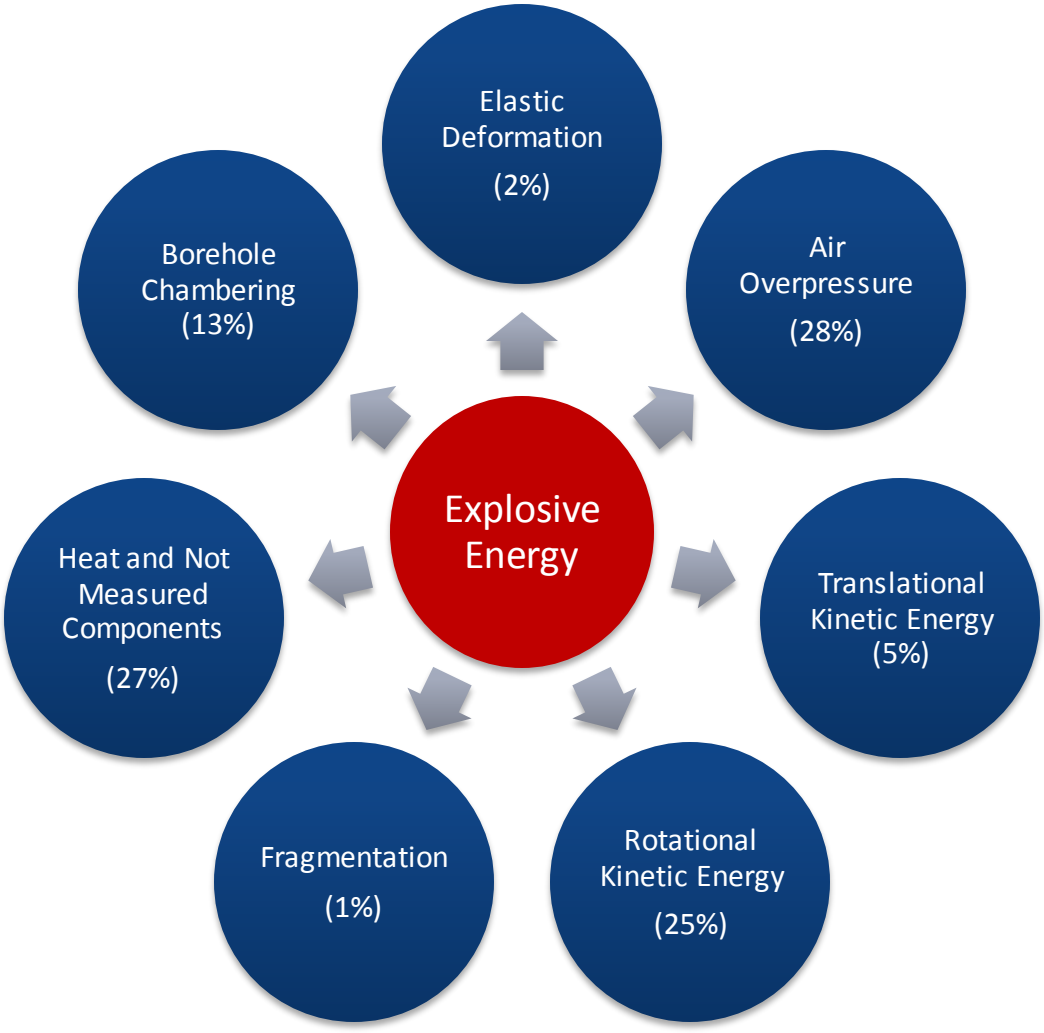

Figure 9.1: Summary of explosive energy components and respective values

9.2 Summary of Novel Contributions

The following is a summary of novel contributions provided by this dissertation research.

- Determined that energy absorbed by borehole chambering accounts for approximately 13% of the explosive's heat of detonation
- Proposed and implemented an alternative method for measuring ground vibration energy by using strain gauges to measure elastic deformation
- Determined that air overpressure energy accounts for 28% of the explosive's heat of detonation
- Showed that rotational kinetic energy can be a significant component of energy partitioning and must be considered
- Expanded upon the energy balance equation and applied this equation to goal programming

9.3 Future Work

It is recommended that additional full-scale testing be conducted to further the understanding of energy partitioning in blasting and continue building upon the current energy balance equation and goal programming objective function for optimizing blasting to decrease overall operating costs.

Ideally, gaining a complete data set for each blast in a test series is preferred. A data set consists of a pre-blast survey to gain an understanding of the geological conditions and the blast design parameters, blast data collection to capture ground vibration and elastic deformation, air overpressure, and fragment velocity,

and finally a post-blast survey to document fragmentation. Due to the complexity of the problem at hand, a complete data set is not likely, especially when considering that a borehole must not be destroyed in order to accurately calculate the energy lost to cratering and the crush zone. An alternative is to conduct multiple tests using samples from a single rock mass.

The first step in the testing process is to complete a very detailed site survey to fully characterize the rock mass being blasted. Until a better methodology is proven, estimation of energy lost to fragmentation is calculated based on the evaluation of new surface area created. This requires a thorough understanding of the current geological conditions to calculate the surface area of the discontinuities already present in the rock mass. A couple of methods come to mind; the first being the use of the SIMBLOC discontinuities network simulation program that is used to model the rock mass. This method requires field measurement of discontinuities, azimuth of the dip vectors, the dip angle, the half-trace, and the spacing (Hamdi, 2007). The second being the use of a 3D laser profiler and associated processing software, in this case a Maptek 8800 scanner and i-Site Studio software. Using the 3D laser profiler, a high resolution point cloud is created and processed via spherical triangulation. Strike and dip can then be determined. From this, joint systems can be analyzed (Maptek, 2011, 2014). Laboratory tests will be needed to determine rock strength properties including Young's Modulus, compressive strength, tensile strength, and specific fracture energy.

A detailed blast design survey must be conducted to accurately gauge the blast parameters. Simply assuming the shot is laid out per the blast design is not acceptable. Burden, spacing, hole depth, bench height, powder column, and stemming height must all be measured and recorded. It is important to record the type of stemming, the explosive products, initiation system, and timing. Due to the variation in timing associated with nonel detonators, it is highly recommended to use an electronic detonation system (Lusk, 2012). This will remove unknowns associated with the variation in timing delay. Slight variations in blast design may very well likely provide insight to differences in energy partition results from test to test.

High-speed photography is a crucial part of blast instrumentation because multiple variables can be analyzed using a single video. The video is used to calculate fragment velocity, size, and trajectory, all of which are used to calculate energy transferred to movement. Video is also used to verify timing and calculate duration of confinement prior to venting as a result of stemming ejection or cracks opening to the free-face. This information is used to aid in the approximation of energy transmitted to the rock versus vented to the atmosphere.

There is some debate as to the velocity profile from the face to the borehole. Sanchidrian et al. (2007) assumes the velocity is constant from the face to the borehole while Ouchterlony et al. (2004) proposes a range from highest at the face to almost zero at the borehole. High-speed photography can be used to solve this problem by mounting a protected high-speed camera over a borehole.

The biggest challenge with this methodology is scale. It would be difficult to safely mount a high-speed camera above a production hole and as shown by this dissertation research, small-scale testing may not yield the number of fragments necessary to accurately determine the velocity gradient.

Seismographs can provide valuable data for blasting operations granted they are properly calibrated, this test series being no different. One problem encountered with seismographs, is that even when properly calibrated, two seismographs still may not provide the same results. As discussed previously, an alternative is to use triaxial accelerometers attached to a data acquisition device. To date, there is no widely accepted way of calculating energy lost to ground vibration or elastic deformation. Previous authors on the subject who have proposed methods for measuring this energy admit that their attempts require refinement before providing accurate results.

A widely known short-coming of fragmentation analysis using imaging techniques is the lack of fines determination. This presents a significant problem because it is believed that up to 90% of the new surface area created may be from fines (Ouchterlony et al., 2004). To overcome this problem, three solutions are available. The first is to conduct a detailed imaging analysis throughout the muckpile as is traditionally done with extra efforts being made to capture the fines. The second method is to perform a sieve analysis of the muckpile. This method is time and cost prohibitive in a production environment. The third solution is a combination of the previous two. Pairing imaging analysis, and data collected from sieving representative muckpile samples, it may be possible to

derive a correlation between mean particle size and the amount of fines generated for a specific blast.

These recommendations, coupled with the present knowledge base will provide the information needed to begin creating a goal programming model that can be implemented in the blasting industry. This model will not only optimize explosive energy use, but also minimize overall operating costs by tailoring the blast parameters to meet the specific needs of the mine, reducing downstream costs.

APPENDIX A

BOREHOLE CHAMBERING TEST SERIES – MAXIMUM VALUES

Peak pressure and strain values for borehole chambering test series

	Sensor 1		Sensor 2		Wave		Sensor 3	Sensor4
Test	Pressure (PSI)	TOA (ms)	Pressure (PSI)	TOA (ms)	Time Diff (ms)	Velocity (fps)	Strain (με)	Strain (με)
1	2.13	3.78	0.76	5.68	1.90	1052	49.82	23.62
2	4.86	2.90	2.55	4.56	1.66	1208	71.70	16.68
3	4.35	4.82	1.88	6.68	1.86	1075	99.46	26.29
4	3.28	4.76	1.53	6.46	1.71	1171	90.89	29.36

APPENDIX B

BOREHOLE CHAMBERING TEST SERIES – AIR OVERPRESSURE ENERGY PLOTS

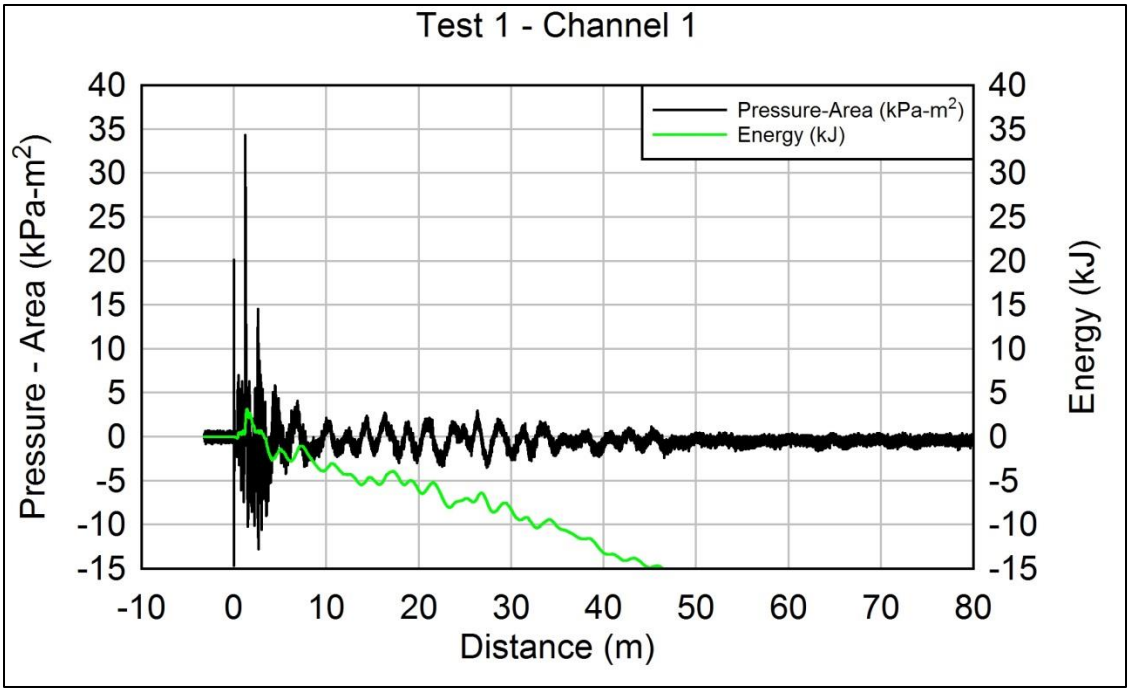
Test 1 - Channel 1
Pressure-Area (kPa-m2)
Energy (kJ)
Pressure - Area (kPa-m2)
Energy (kJ)
Distance (m)
40
35
30
25
20
15
10
5
0
-5
-10
-15
-10
0
10
20
30
40
50
60
70
80

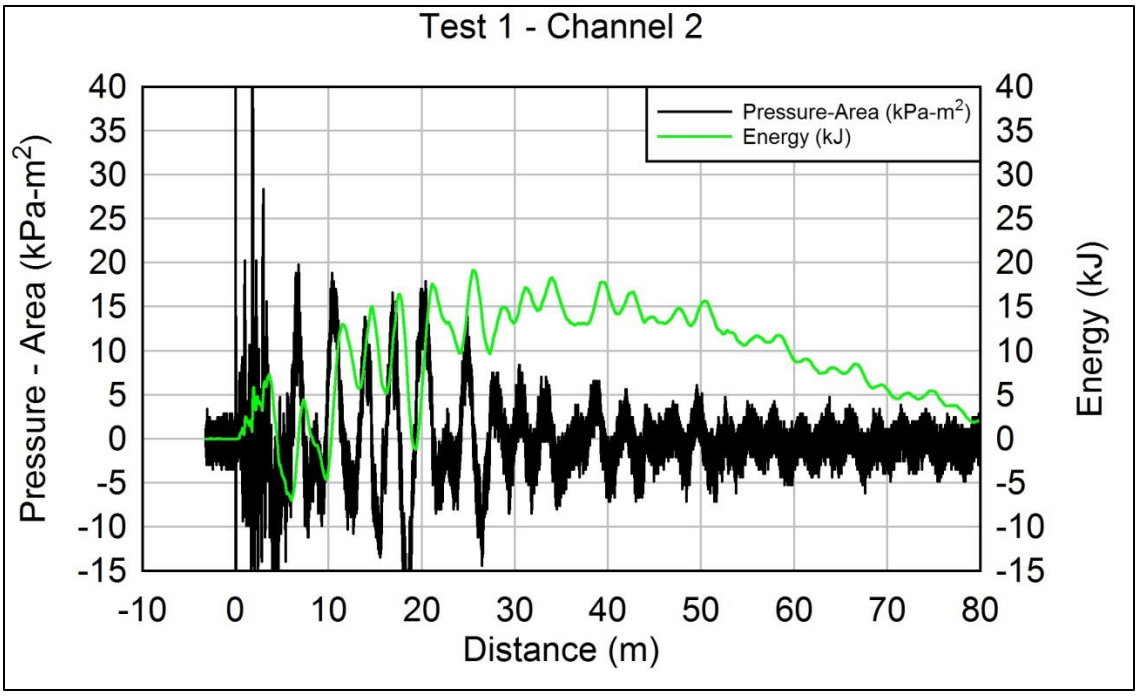
Test 1 - Channel 2
Pressure-Area (kPa-m2)
Energy (kJ)
Pressure - Area (kPa-m2)
Energy (kJ)
Distance (m)
40
35
30
25
20
15
10
5
0
-5
-10
-15
-10
0
10
20
30
40
50
60
70
80

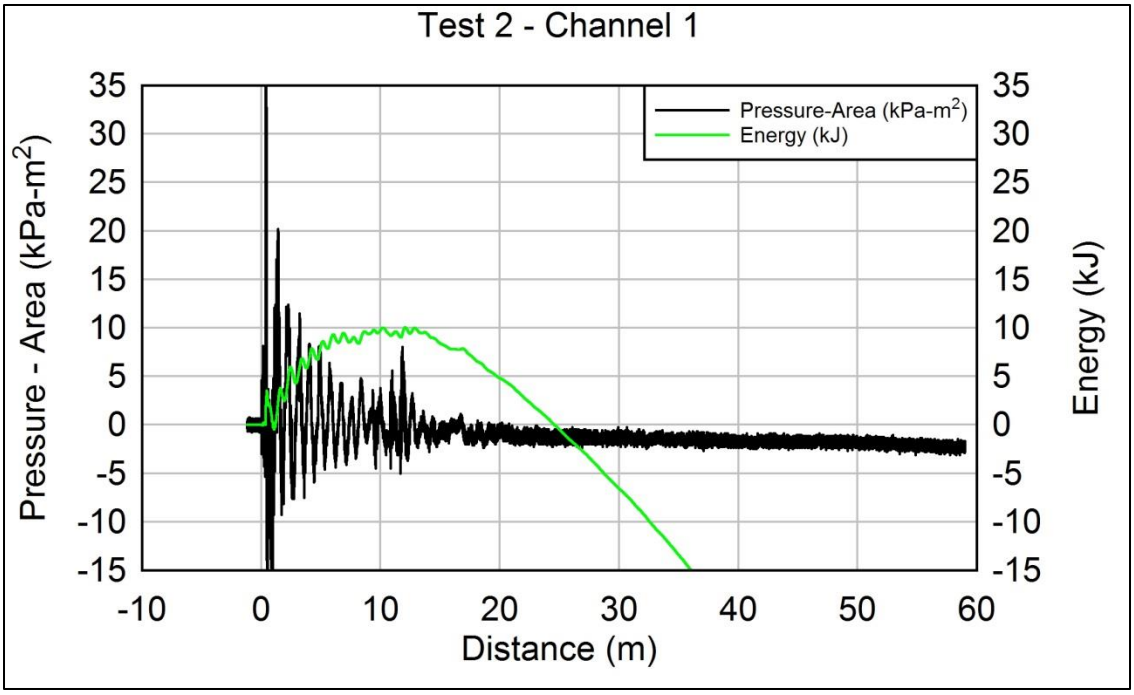
Test 2 - Channel 1
Pressure-Area (kPa-m2)
Energy (kJ)
Pressure - Area (kPa-m2)
Energy (kJ)
Distance (m)
35
30
25
20
15
10
5
0
-5
-10
-15
-10
0
10
20
30
40
50
60

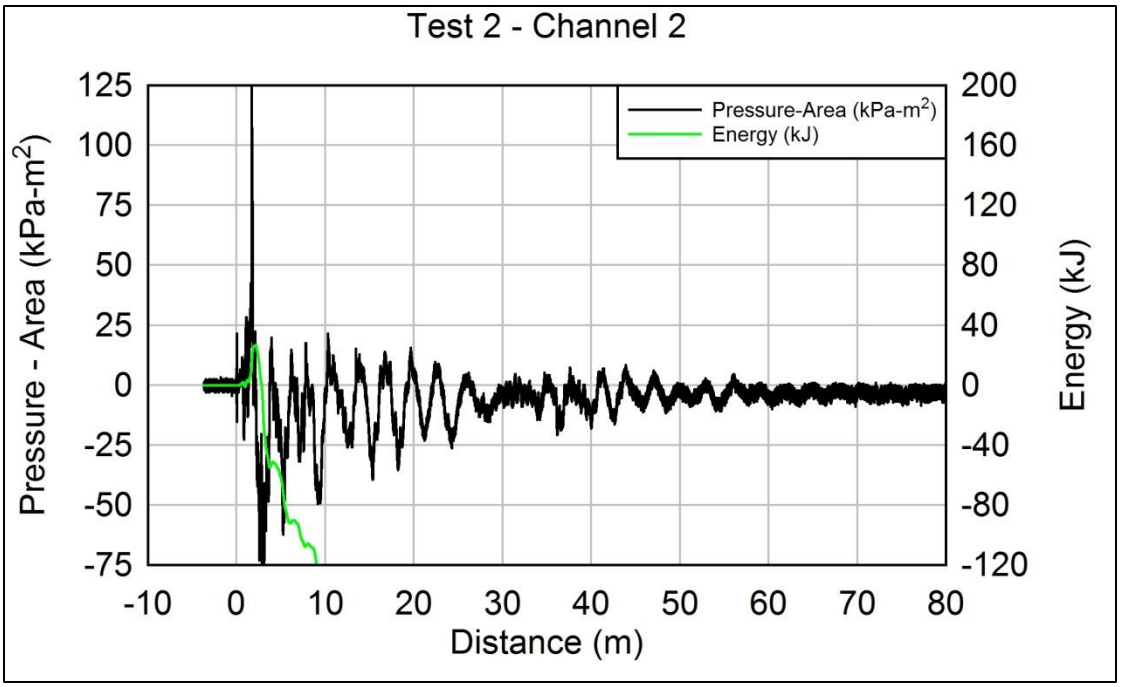
Test 2 - Channel 2
Pressure-Area (kPa-m2)
Energy (kJ)
Pressure - Area (kPa-m2)
Energy (kJ)
Distance (m)
125
100
75
50
25
0
-25
-50
-75
200
160
120
80
40
0
-40
-80
-120
-10
0
10
20
30
40
50
60
70
80

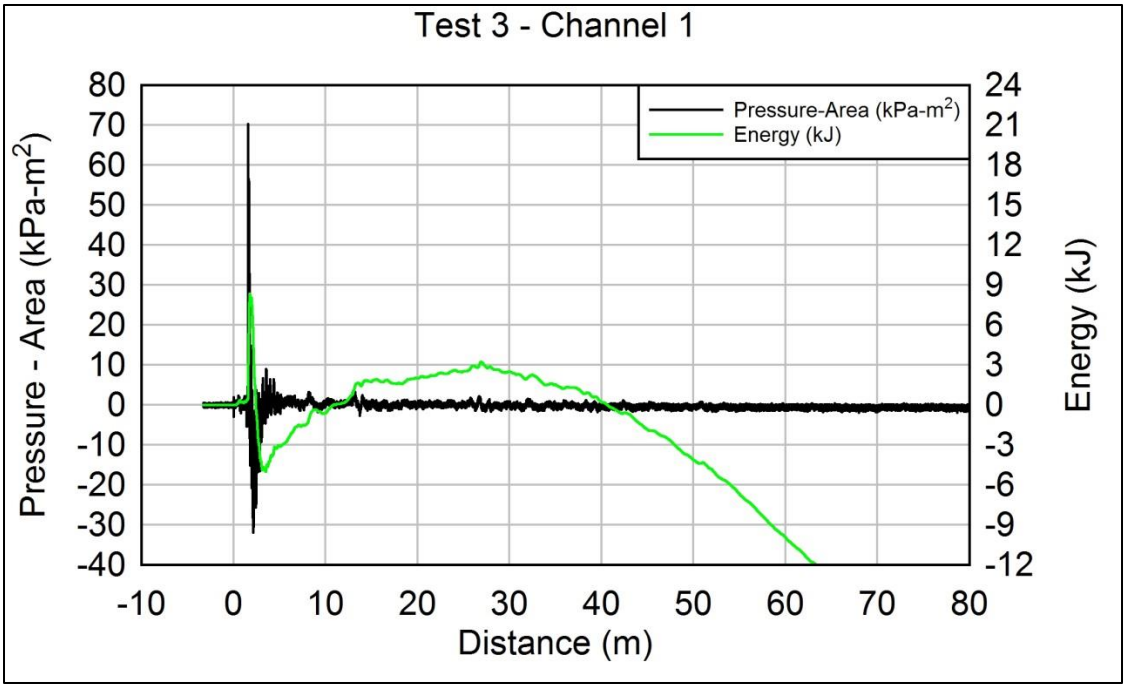
Test 3 - Channel 1
Pressure-Area (kPa-m2)
Energy (kJ)
Pressure - Area (kPa-m2)
Energy (kJ)
Distance (m)
80
70
60
50
40
30
20
10
0
-10
-20
-30
-40
24
21
18
15
12
9
6
3
0
-3
-6
-9
-12
-10
0
10
20
30
40
50
60
70
80

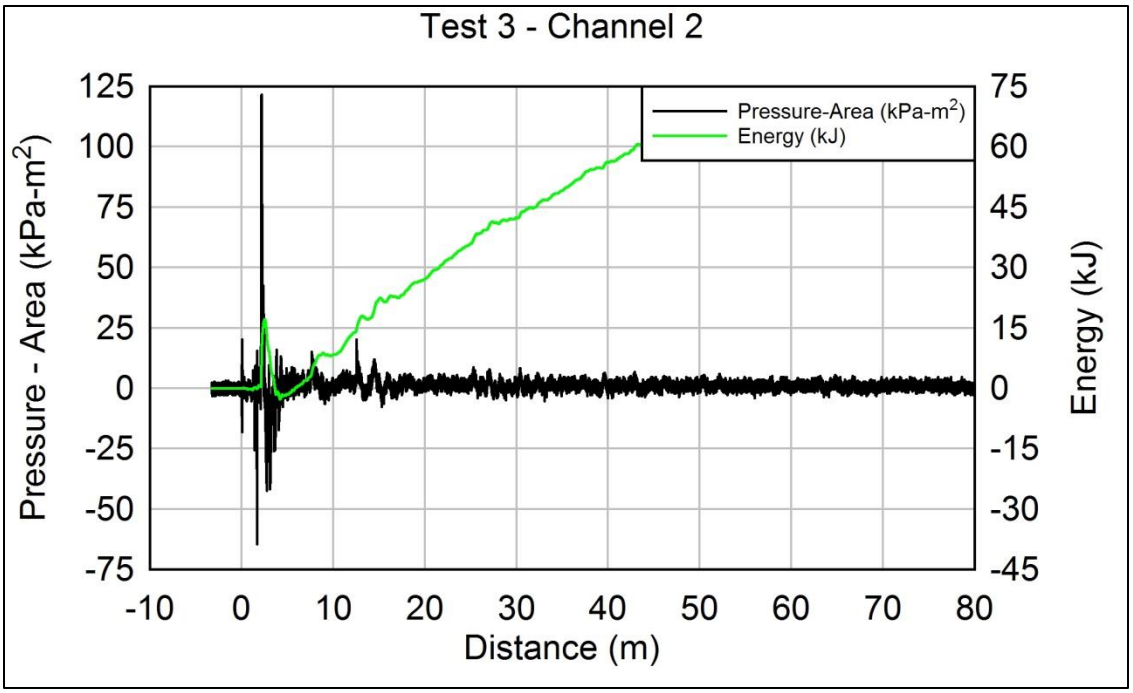
Test 3 - Channel 2
Pressure-Area (kPa-m2)
Energy (kJ)
Pressure - Area (kPa-m2)
Energy (kJ)
Distance (m)
125
100
75
50
25
0
-25
-50
-75
75
60
45
30
15
0
-15
-30
-45
-10
0
10
20
30
40
50
60
70
80

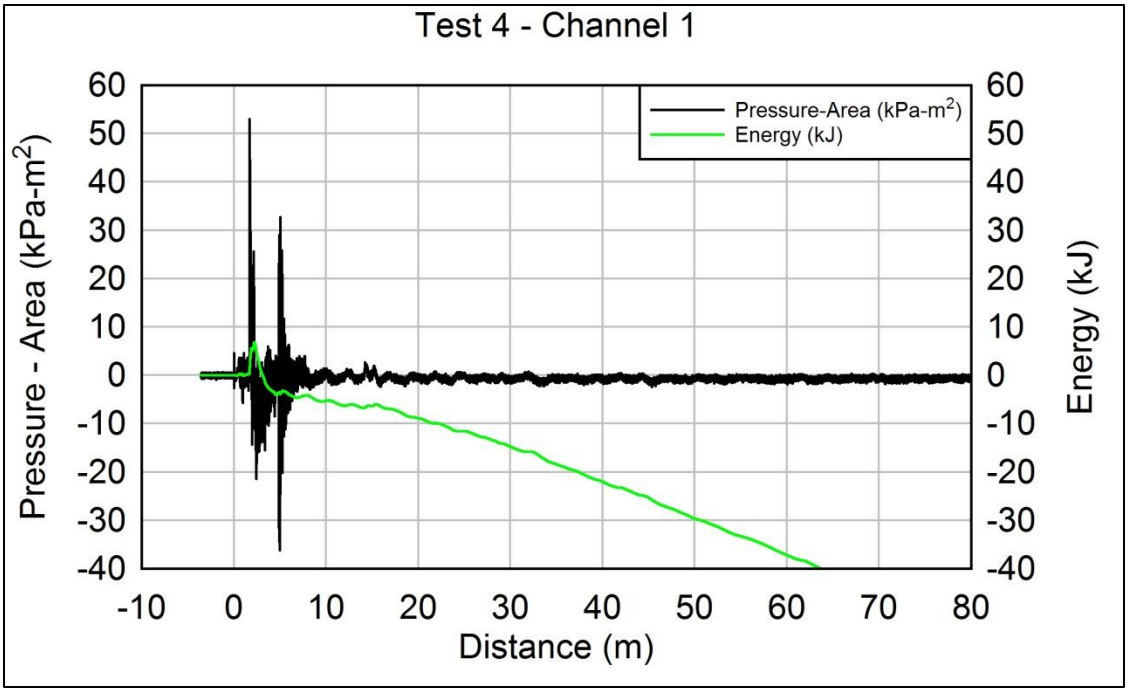
Test 4 - Channel 1
Pressure-Area (kPa-m2)
Energy (kJ)
Pressure - Area (kPa-m2)
Energy (kJ)
Distance (m)
60
50
40
30
20
10
0
-10
-20
-30
-40
-10
0
10
20
30
40
50
60
70
80

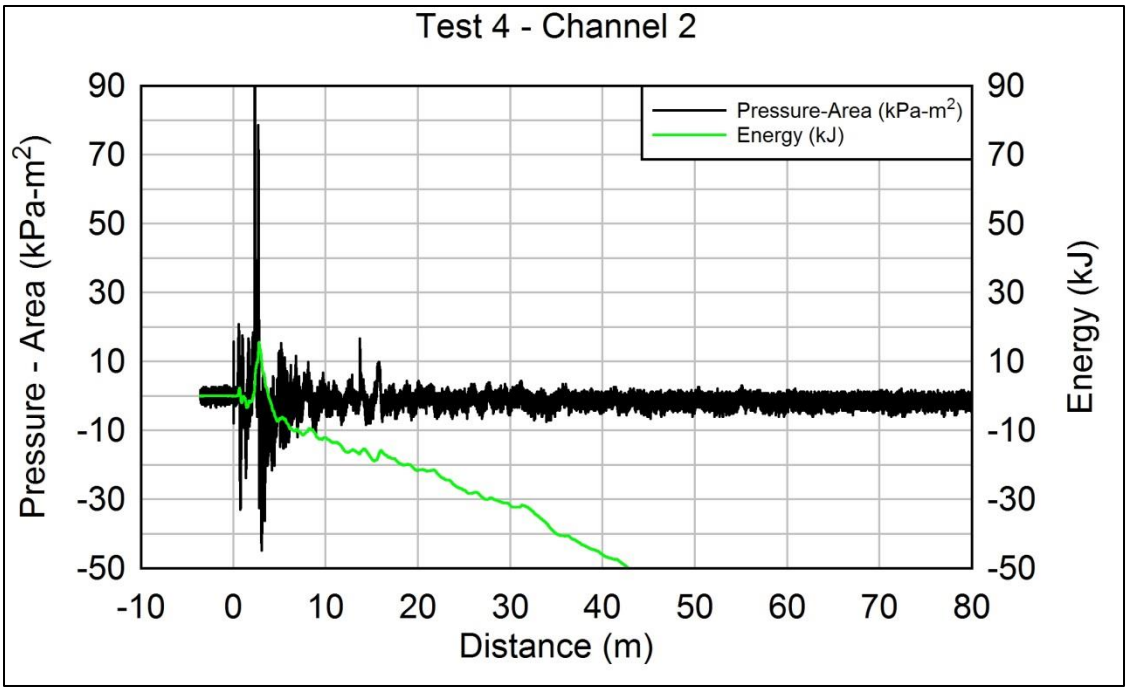
Test 4 - Channel 2
Pressure-Area (kPa-m2)
Energy (kJ)
Pressure - Area (kPa-m2)
Energy (kJ)
Distance (m)
90
70
50
30
10
-10
-30
-50
-10
0
10
20
30
40
50
60
70
80

APPENDIX C

STEMMING TEST SERIES – MAXIMUM VALUES

Sand/Cornstarch

	1	2	3	4	5	6	7	8	Seismograph			
Test	Pressure (PSI)	Pressure (PSI)	Pressure (PSI)	Pressure (PSI)	Strain (με)	Strain (με)	Trans (με)	Long (με)	Acoustic (dB)	Radial (in/s)	Vert (in/s)	Trans (in/s)
1	1.224	0.687	2.284	1.411	16.28	4.04	62.36	69.309	138	0.01	0.01	0
2	0.891	0.496	1.536	1.590	15.03	2.64	159.36	154.79	139	0.005	0.005	0.005
3	0.551	0.277	1.391	0.385	7.32	1.96	295.63	336.15	141	0	0.005	0.005
Avg	**0.889**	**0.487**	**1.737**	**1.129**	**12.88**	**2.88**	**172.45**	**186.75**	**139.33**	**0.005**	**0.007**	**0.003**

Air/Sand

	1	2	3	4	5	6	7	8	Seismograph			
Test	Pressure (PSI)	Pressure (PSI)	Pressure (PSI)	Pressure (PSI)	Strain (με)	Strain (με)	Trans (με)	Long (με)	Acoustic (dB)	Radial (in/s)	Vert (in/s)	Trans (in/s)
1	1.709	0.759	2.442	0.812	21.42	2.06	93.54	88.946	145	0	0.01	0.01
2	0.069	0.412	1.783	1.638	13.39	2.48	70.444	65.843	137	0.005	0.005	0.005
3	0.524	0.256	2.331	1.405	7.68	1.87	159.36	154.79	142	0	0.005	0.005
Avg	**0.767**	**0.476**	**2.185**	**1.285**	**14.16**	**2.14**	**107.78**	**103.19**	**141.33**	**0.002**	**0.007**	**0.007**

Sand

	1	2	3	4	5	6	7	8	Seismograph			
Test	Pressure (PSI)	Pressure (PSI)	Pressure (PSI)	Pressure (PSI)	Strain (με)	Strain (με)	Trans (με)	Long (με)	Acoustic (dB)	Radial (in/s)	Vert (in/s)	Trans (in/s)
1	0.516	0.306	1.212	1.425	34.34	3.17	69.289	101.65	128	0	0	0
2	0.419	1.345	1.803	1.445	7.53	2.27	147.82	159.41	137	0.005	0.005	0.005
3	0.780	0.356	3.925	1.873	6.54	1.80	64.67	79.705	133	0.005	0.005	0.005
Avg	**0.572**	**0.669**	**2.314**	**1.581**	**16.13**	**2.41**	**93.93**	**113.59**	**132.67**	**0.003**	**0.003**	**0.003**

Cornstarch

	1	2	3	4	5	6	7	8	Seismograph			
Test	Pressure (PSI)	Pressure (PSI)	Pressure (PSI)	Pressure (PSI)	Strain (με)	Strain (με)	Trans (με)	Long (με)	Acoustic (dB)	Radial (in/s)	Vert (in/s)	Trans (in/s)
1	0.288	0.356	0.395	0.558	57.03	10.10	92.385	152.48	133	0.01	0.04	0.02
2	0.322	0.306	0.374	0.227	55.56	8.66	105.09	138.62	130	0.005	0.055	0.01
3	0.233	0.284	0.306	0.413	50.17	13.51	180.15	192.91	127	0.01	0.045	0.01
Avg	**0.281**	**0.315**	**0.358**	**0.399**	**54.25**	**10.75**	**125.88**	**161.34**	**130.00**	**0.008**	**0.047**	**0.013**

Air

	1	2	3	4	5	6	7	8	Seismograph			
Test	Pressure (PSI)	Pressure (PSI)	Pressure (PSI)	Pressure (PSI)	Strain (με)	Strain (με)	Trans (με)	Long (με)	Acoustic (dB)	Radial (in/s)	Vert (in/s)	Trans (in/s)
1	2.000	1.013	3.019	1.431	12.10	1.78	168.6	248.36	146	0.01	0.01	0.01
2	2.375	0.957	1.830	1.025	6.47	1.59	321.04	274.92	147	0.005	0.015	0.005
3	4.440	1.664	3.074	1.618	7.58	1.24	218.26	222.94	145	0.005	0.015	0.005
Avg	**2.938**	**1.211**	**2.641**	**1.358**	**8.72**	**1.54**	**235.97**	**248.74**	**146.00**	**0.007**	**0.013**	**0.007**

Cornstarch/Sand

	1	2	3	4	5	6
Test	Pressure (PSI)	Pressure (PSI)	Pressure (PSI)	Pressure (PSI)	Strain (με)	Strain (με)
1	0.094	0.136	0.079	0.068	49.67	28.23
2	0.066	0.115	0.079	0.075	42.26	15.40
3	0.072	0.129	0.072	0.083	39.13	14.44
Avg	**0.077**	**0.127**	**0.077**	**0.076**	**43.69**	**19.36**

APPENDIX D

STRAIN MAPPING TEST SERIES – AVERAGE ELASTIC DEFORMATION ENERGY CALCULATIONS

Distance (ft)	Affected Area (ft3)	Affected Area (m3)	Strain (με)	Strain (ε)	Young's Modulus	Transverse Energy (J)	Axial Energy (J)	Vertical Energy (J)
0.1	0.079	0.00	590.40	0.00059	5.99E+10	23.36	70.08	23.36
0.25	0.411	0.01	185.76	0.000186	5.99E+10	12.03	36.09	12.03
0.5	1.47	0.04	77.45	7.75E-05	5.99E+10	7.48	22.44	7.48
0.75	2.46	0.07	46.43	4.64E-05	5.99E+10	4.50	13.50	4.50
1	3.43	0.10	32.30	3.23E-05	5.99E+10	3.03	9.10	3.03
2	23.57	0.67	13.47	1.35E-05	5.99E+10	3.63	10.88	3.63
3	39.27	1.11	8.07	8.07E-06	5.99E+10	2.17	6.51	2.17
4	63.35	1.79	5.61	5.61E-06	5.99E+10	1.69	5.08	1.69
5	127.76	3.62	4.24	4.24E-06	5.99E+10	1.95	5.84	1.95
6	190.59	5.40	3.37	3.37E-06	5.99E+10	1.83	5.50	1.83
7	265.99	7.53	2.77	2.77E-06	5.99E+10	1.73	5.20	1.73
8	353.95	10.02	2.34	2.34E-06	5.99E+10	1.65	4.94	1.65
9	454.48	12.87	2.02	2.02E-06	5.99E+10	1.57	4.71	1.57
10	567.59	16.07	1.77	1.77E-06	5.99E+10	1.50	4.51	1.50
15	4974.18	140.85	1.06	1.06E-06	5.99E+10	4.73	14.20	4.73
20	9686.62	274.29	0.74	7.37E-07	5.99E+10	4.46	13.38	4.46
25	15969.7	452.21	0.56	5.56E-07	5.99E+10	4.19	12.56	4.19
30	23823.8	674.61	0.44	4.42E-07	5.99E+10	3.94	11.82	3.94
40	77492.3	2194.33	0.31	3.07E-07	5.99E+10	6.20	18.61	6.20
50	127758	3617.70	0.23	2.32E-07	5.99E+10	5.82	17.46	5.82
60	190590	5396.90	0.18	1.84E-07	5.99E+10	5.48	16.44	5.48
					SUM	**102.95**	**308.85**	**102.95**

APPENDIX E

STRAIN MAPPING TEST SERIES – AIR OVERPRESSURE ENERGY PLOTS

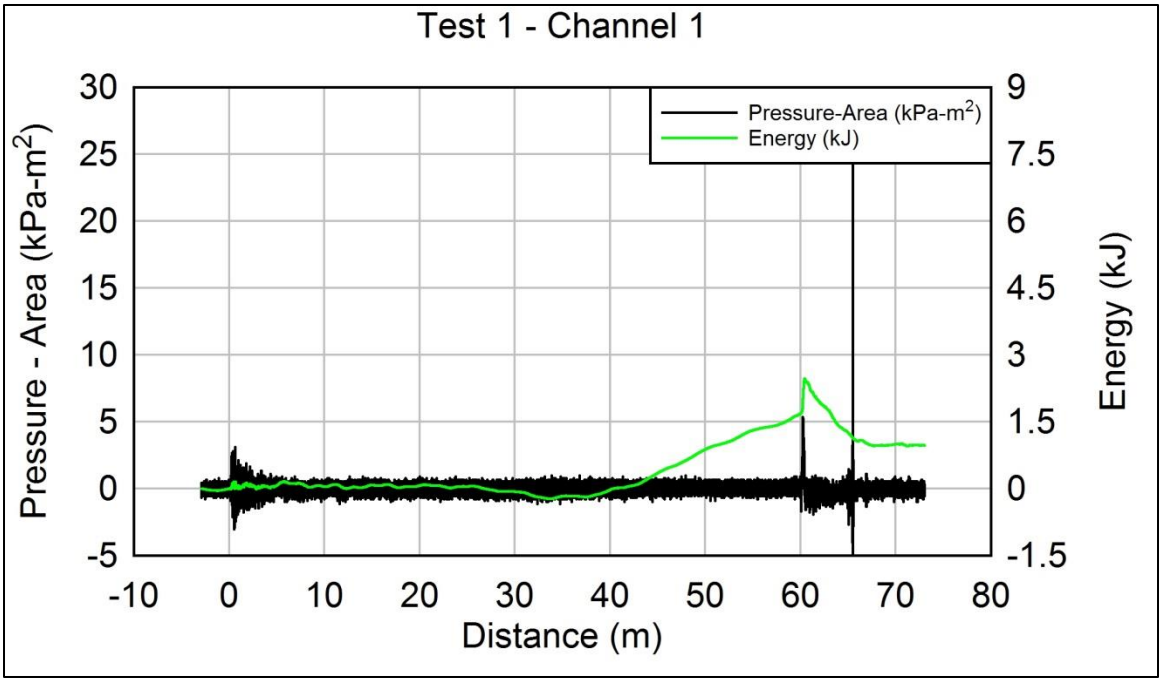
Test 1 - Channel 1
Pressure-Area (kPa-m2)
Energy (kJ)
Pressure - Area (kPa-m2)
Energy (kJ)
Distance (m)
30
25
20
15
10
5
0
-5
9
7.5
6
4.5
3
1.5
0
-1.5
-10
0
10
20
30
40
50
60
70
80

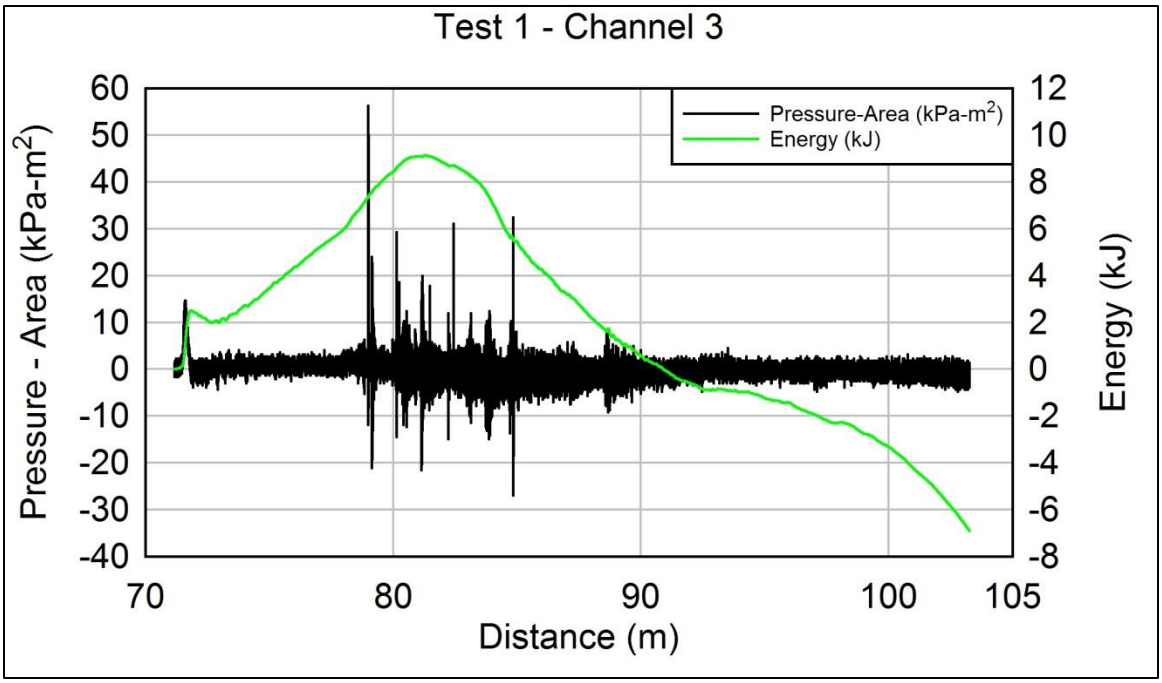
Test 1 - Channel 3
Pressure-Area (kPa-m2)
Energy (kJ)
Pressure - Area (kPa-m2)
Energy (kJ)
Distance (m)
60
50
40
30
20
10
0
-10
-20
-30
-40
12
10
8
6
4
2
0
-2
-4
-6
-8
70
80
90
100
105

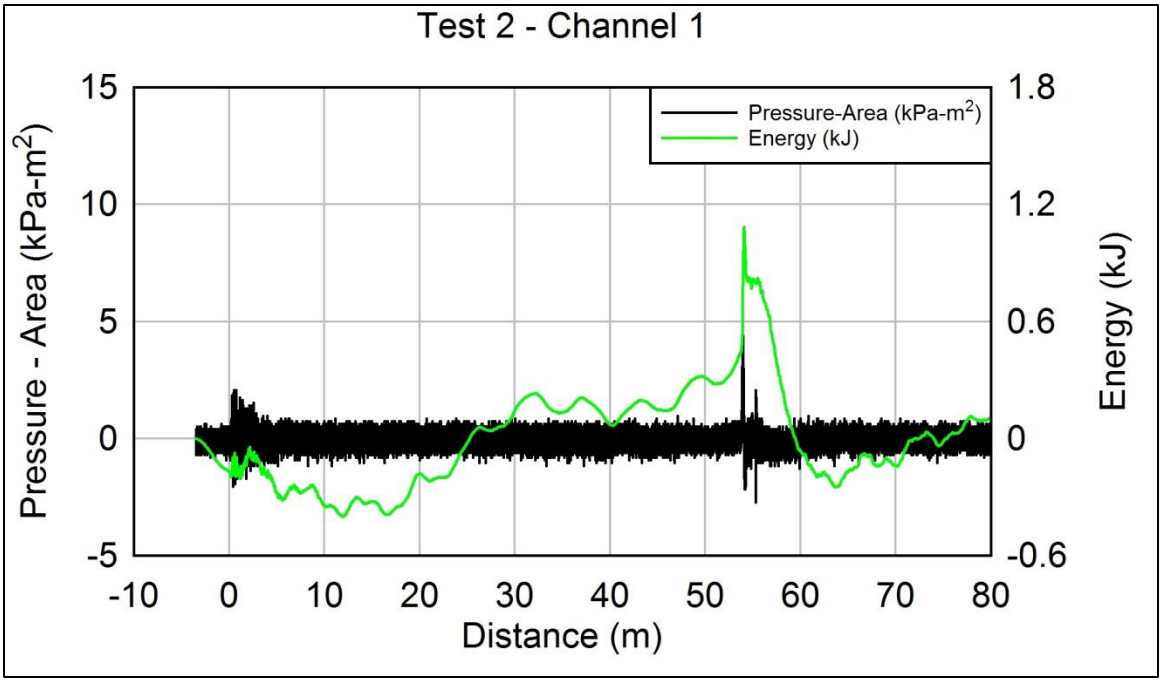
Test 2 - Channel 1
Pressure-Area (kPa-m2)
Energy (kJ)
Pressure - Area (kPa-m2)
Energy (kJ)
Distance (m)
15
10
5
0
-5
1.8
1.2
0.6
0
-0.6
-10
0
10
20
30
40
50
60
70
80

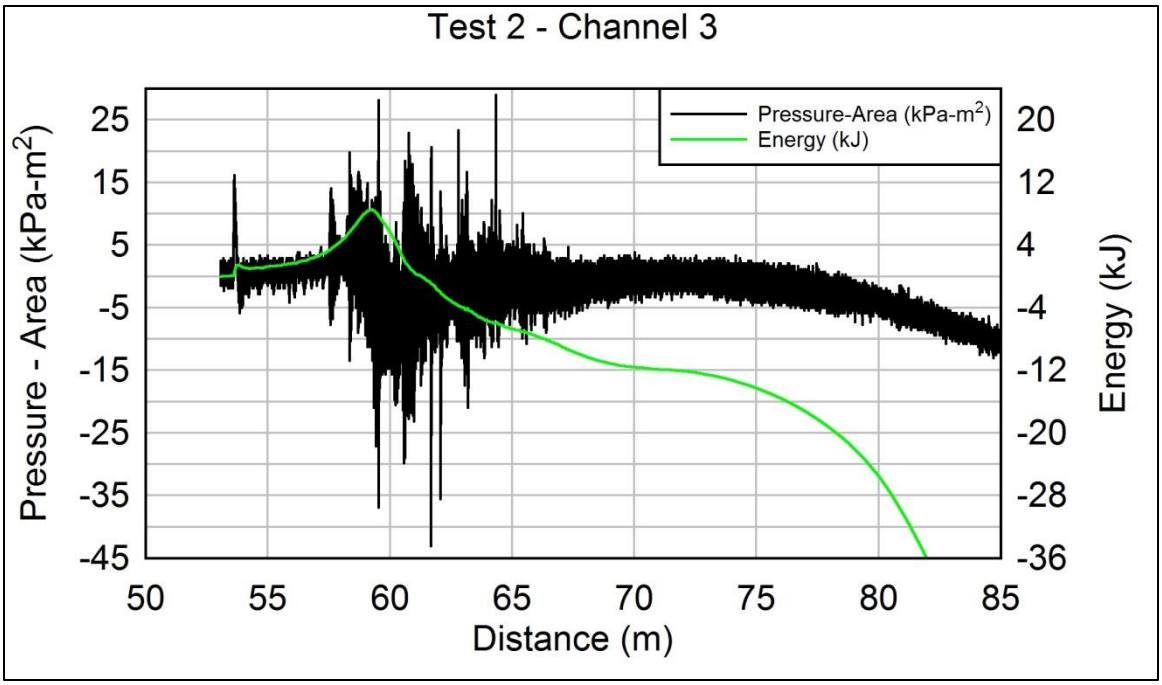
Test 2 - Channel 3
Pressure-Area (kPa-m2)
Energy (kJ)
Pressure - Area (kPa-m2)
Energy (kJ)
Distance (m)
25
15
5
-5
-15
-25
-35
-45
20
12
4
-4
-12
-20
-28
-36
50
55
60
65
70
75
80
85

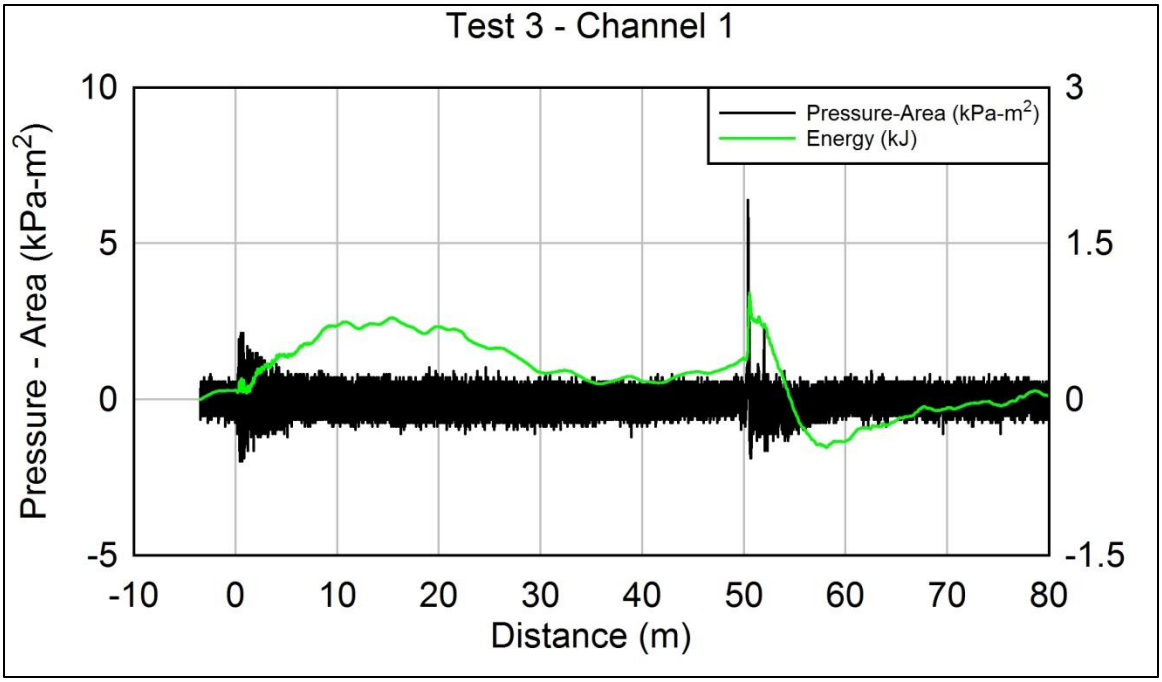
Test 3 - Channel 1
Pressure-Area (kPa-m2)
Energy (kJ)
Pressure - Area (kPa-m2)
Distance (m)
10
5
0
-5
3
1.5
0
-1.5
-10
0
10
20
30
40
50
60
70
80

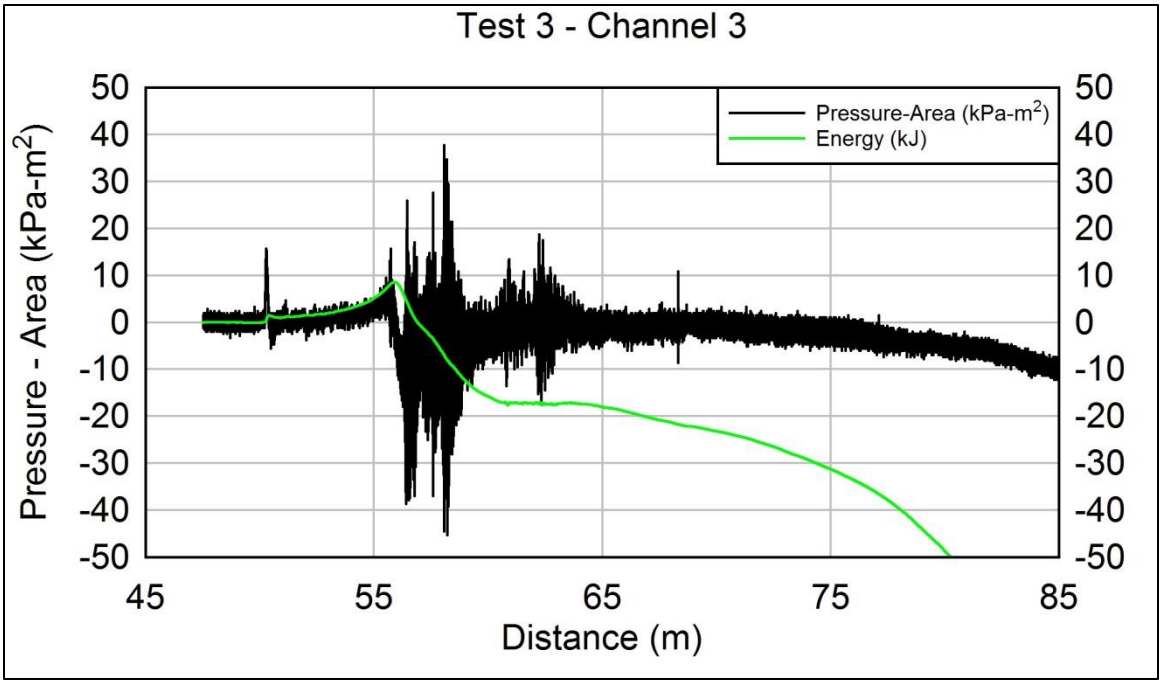
Test 3 - Channel 3
Pressure-Area (kPa-m2)
Energy (kJ)
Pressure - Area (kPa-m2)
Distance (m)
50
40
30
20
10
0
-10
-20
-30
-40
-50
45
55
65
75
85

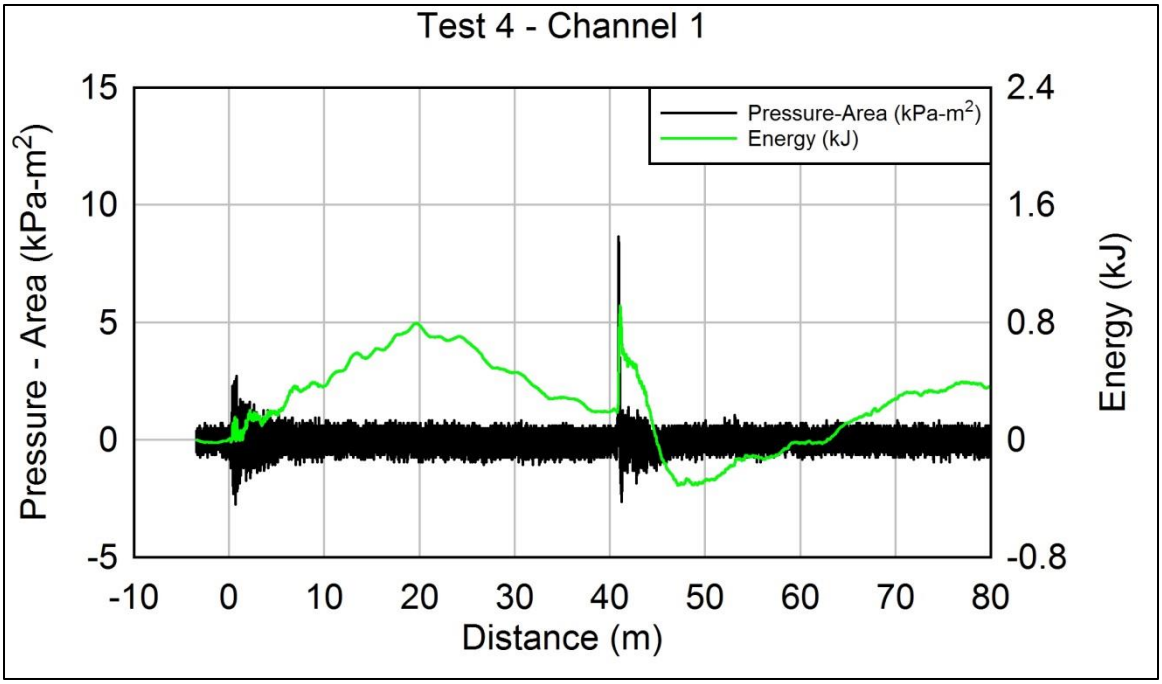
Test 4 - Channel 1
Pressure-Area (kPa-m2)
Energy (kJ)
Pressure - Area (kPa-m2)
Energy (kJ)
Distance (m)
15
10
5
0
-5
2.4
1.6
0.8
0
-0.8
-10
0
10
20
30
40
50
60
70
80

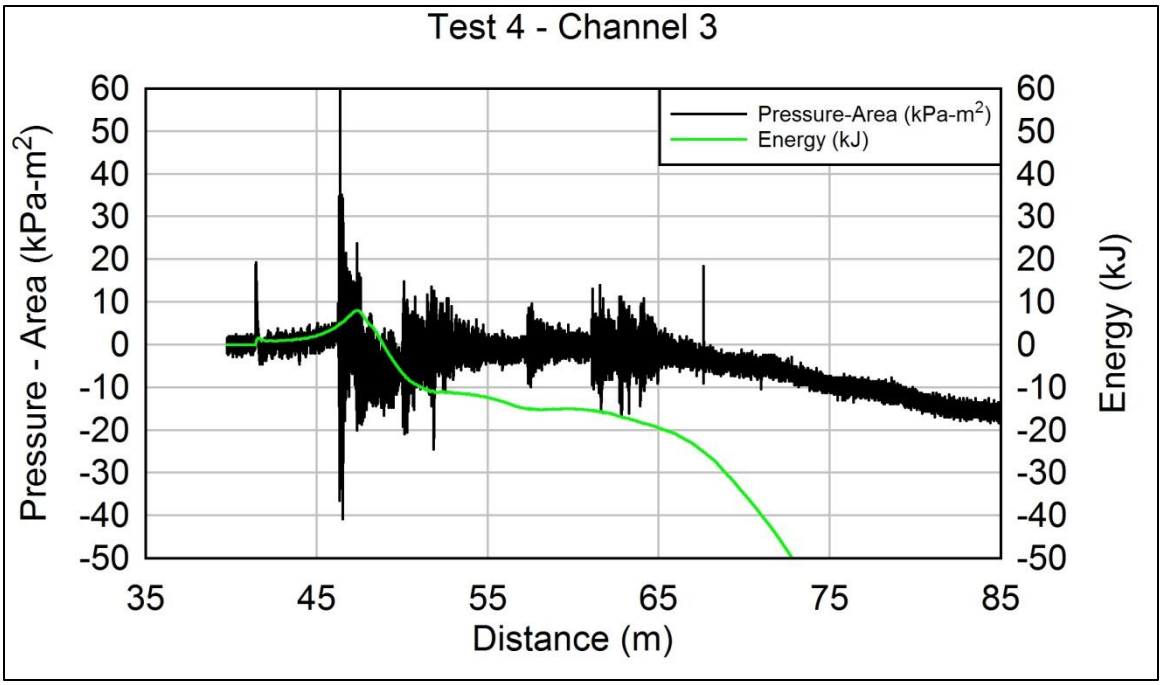
Test 4 - Channel 3
Pressure-Area (kPa-m2)
Energy (kJ)
Pressure - Area (kPa-m2)
Energy (kJ)
Distance (m)
60
50
40
30
20
10
0
-10
-20
-30
-40
-50
35
45
55
65
75
85

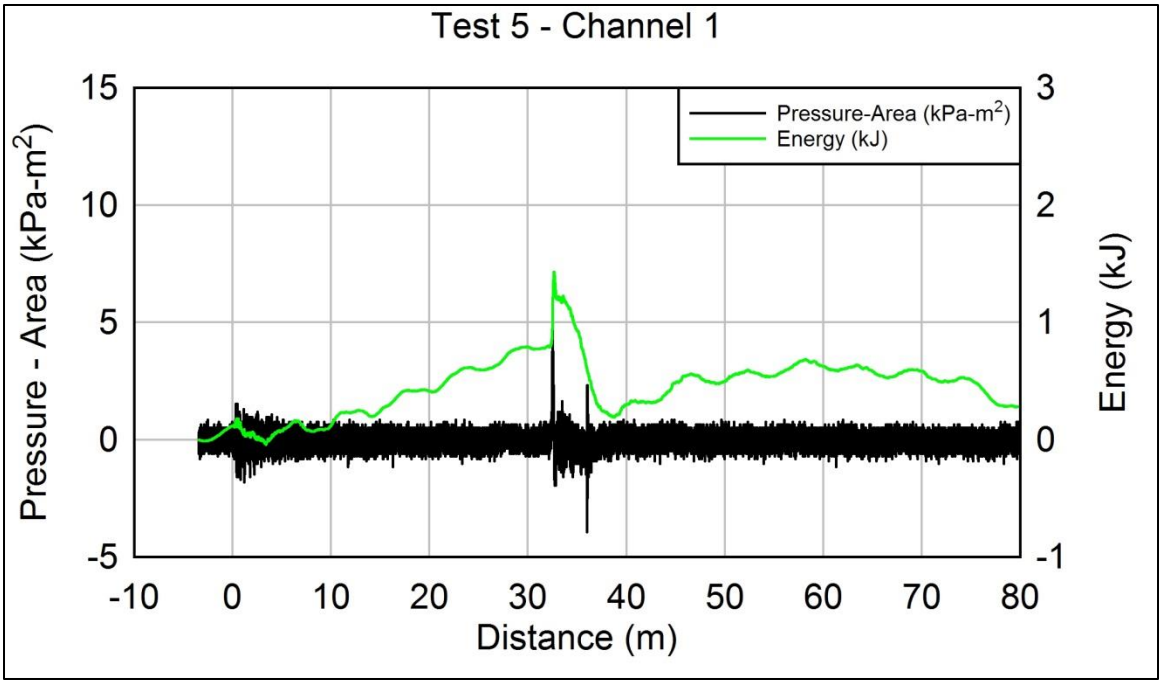
Test 5 - Channel 1
Pressure-Area (kPa-m2)
Energy (kJ)
Pressure - Area (kPa-m2)
Energy (kJ)
Distance (m)
15
10
5
0
-5
3
2
1
0
-1
-10
0
10
20
30
40
50
60
70
80

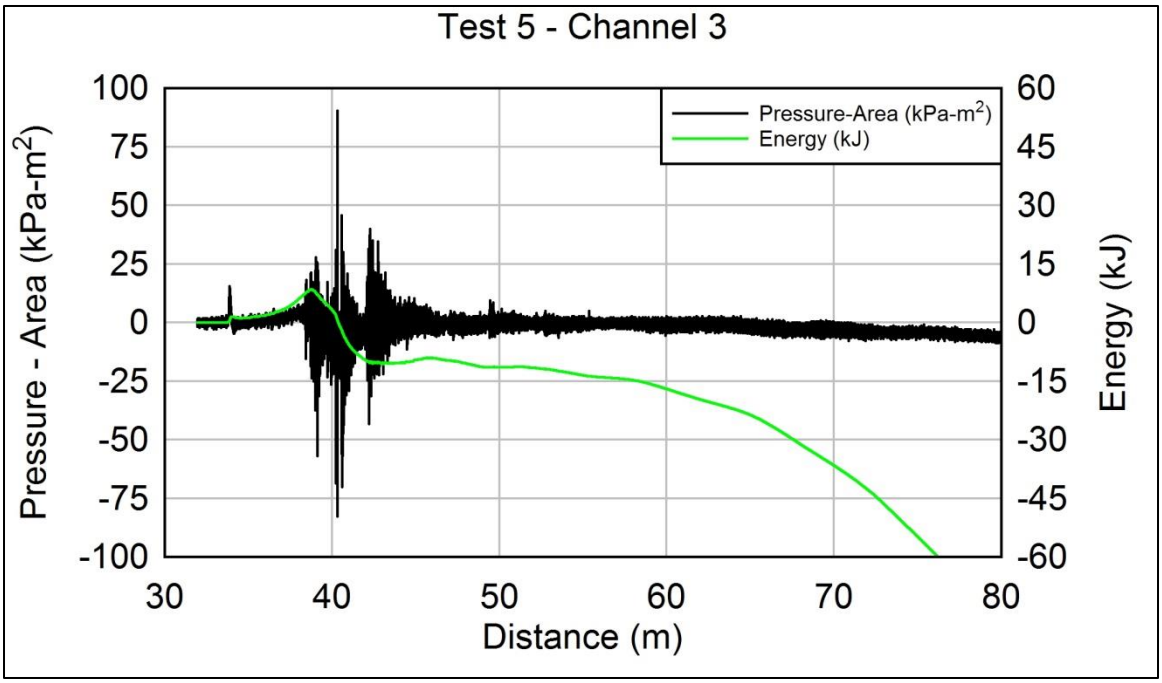
Test 5 - Channel 3
Pressure-Area (kPa-m2)
Energy (kJ)
Pressure - Area (kPa-m2)
Energy (kJ)
Distance (m)
100
75
50
25
0
-25
-50
-75
-100
60
45
30
15
0
-15
-30
-45
-60
30
40
50
60
70
80

APPENDIX F

CONCRETE BLOCK TEST SERIES – UNCONFINED COMPRESSIVE STRENGTH FOR CONCRETE BLOCK

ASTM D7012-10. Standard Test Method for Compressive Strength and Elastic Moduli of Intact Rock Core Specimens under Vayring States of Stress and Temperatures. 2 Inch Core Sample

Name of Client	Calnan
Hole Number	1

Graph 1

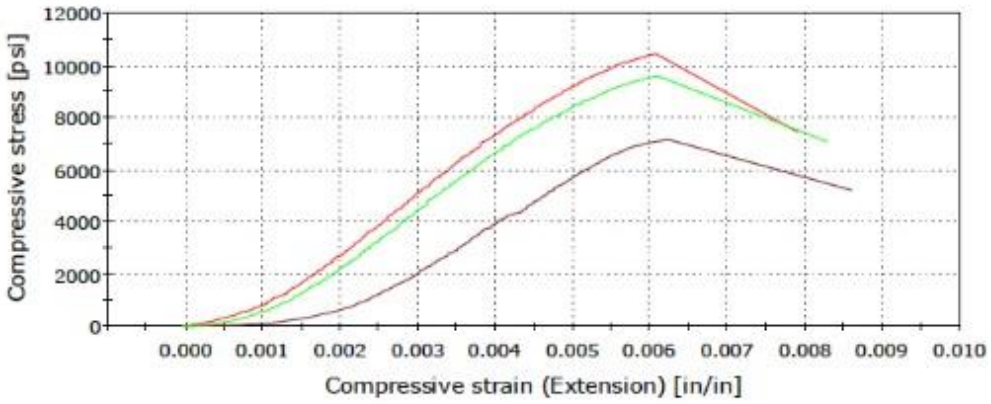

	Depth [ft]	Diameter [in]	Specimen Length [in]	Density (lb/ft^3) [lbf/ft^3]
1	1	2.080	4.180	136.3
2	3	2.085	4.215	136.9
3	2	2.085	4.185	137.9
Mean	2	2.083	4.193	137.0
Standard deviation	1.00000	0.00289	0.01893	0.80861
Maximum	3	2.085	4.215	137.9
Range	2	0.005	0.035	1.6

	Maximum Load [lbf]	Compressive Strength [psi]	Modulus (Automatic Young's) [psi]
1	35,455.0	10,434.2	2,383,883.5
2	24,431.5	7,155.6	1,940,332.5
3	32,734.9	9,587.6	2,282,456.2
Mean	30,873.8	9,059.1	2,202,224.1
Standard deviation	5,742.57446	1,701.98295	232,405.41862
Maximum	35,455.0	10,434.2	2,383,883.5
Range	11,023.5	3,278.6	443,551.0

APPENDIX G

CONCRETE BLOCK TEST SERIES – CONCRETE THREE POINT BENDING TEST / FRACTURE ENERGY PLOTS

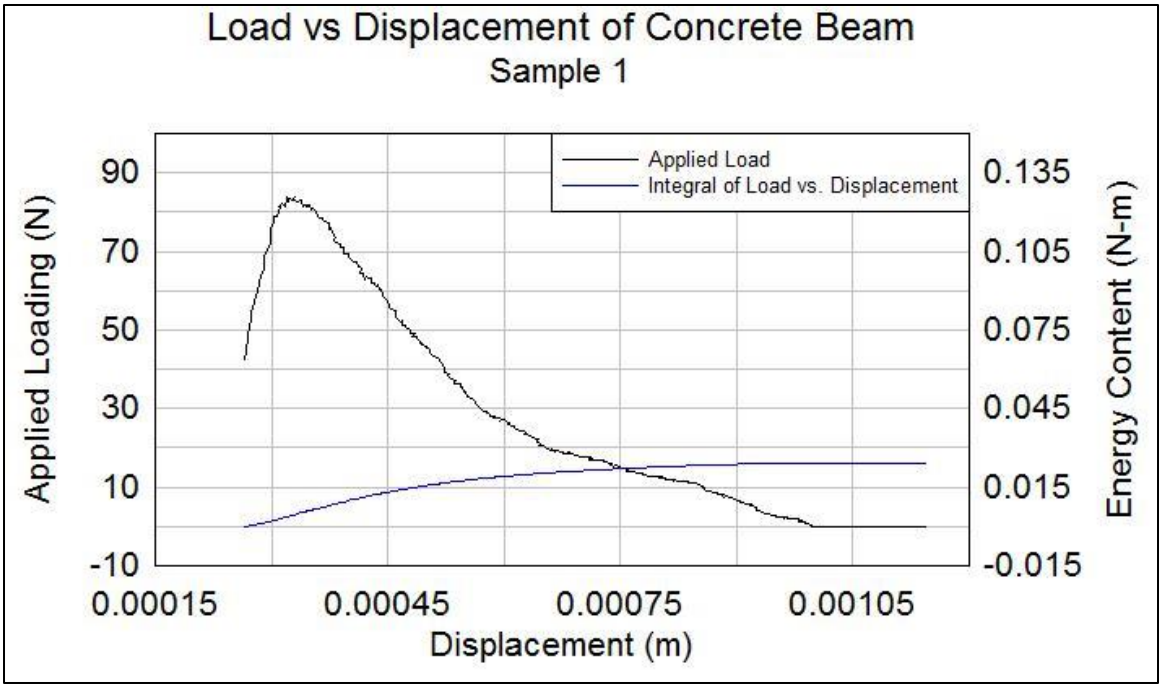
Load vs Displacement of Concrete Beam
Sample 1
Applied Load
Integral of Load vs. Displacement
Applied Loading (N)
Energy Content (N-m)
Displacement (m)
90
70
50
30
10
-10
0.135
0.105
0.075
0.045
0.015
-0.015
0.00015
0.00045
0.00075
0.00105

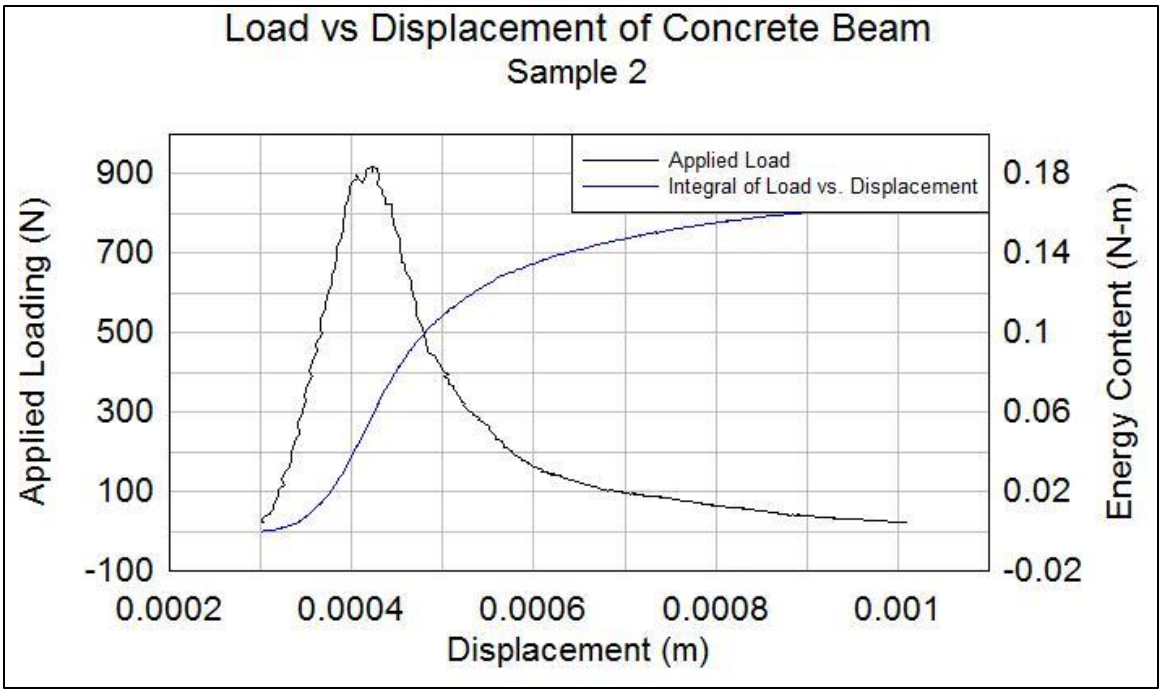
Load vs Displacement of Concrete Beam
Sample 2
Applied Load
Integral of Load vs. Displacement
Applied Loading (N)
Energy Content (N-m)
Displacement (m)
900
700
500
300
100
-100
0.18
0.14
0.1
0.06
0.02
-0.02
0.0002
0.0004
0.0006
0.0008
0.001

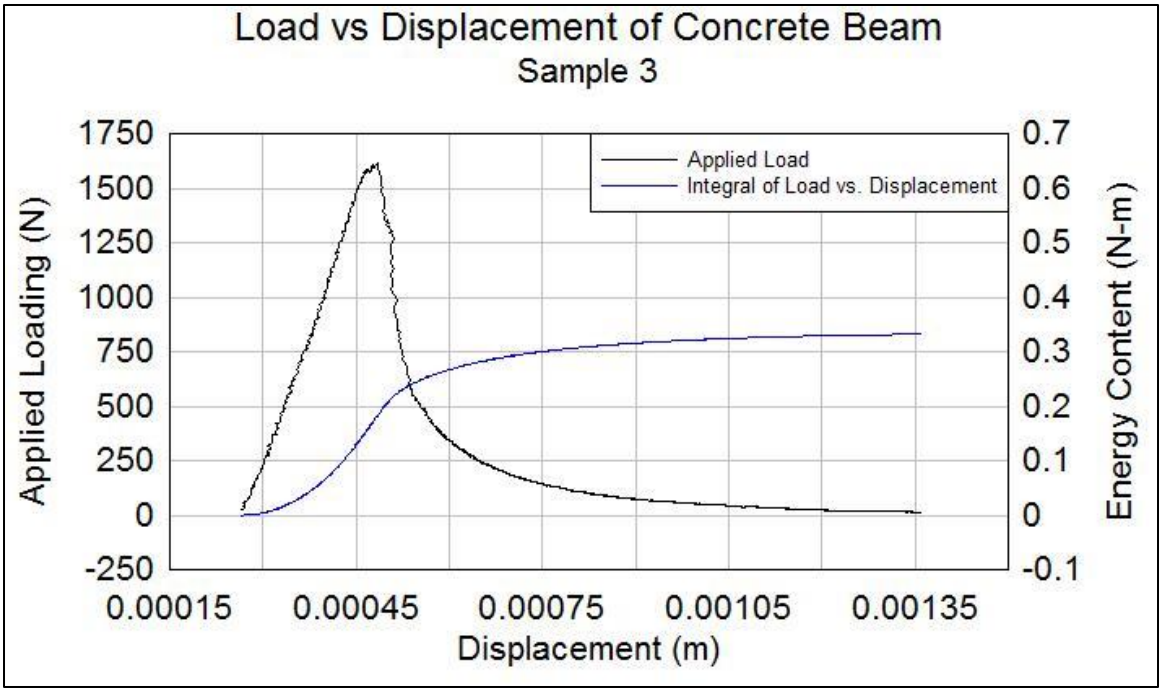
Load vs Displacement of Concrete Beam
Sample 3
Applied Load
Integral of Load vs. Displacement
Applied Loading (N)
Energy Content (N-m)
Displacement (m)
1750
1500
1250
1000
750
500
250
0
-250
0.7
0.6
0.5
0.4
0.3
0.2
0.1
0
-0.1
0.00015
0.00045
0.00075
0.00105
0.00135

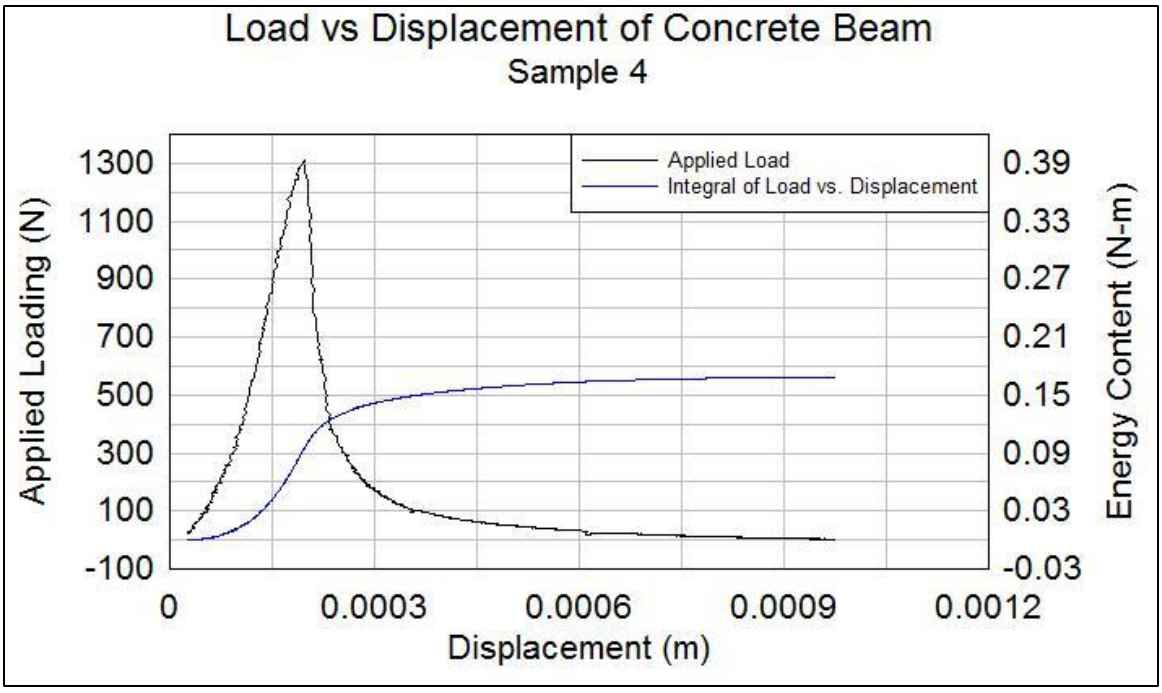
Load vs Displacement of Concrete Beam
Sample 4
Applied Load
Integral of Load vs. Displacement
Applied Loading (N)
Energy Content (N-m)
Displacement (m)
1300
1100
900
700
500
300
100
-100
0.39
0.33
0.27
0.21
0.15
0.09
0.03
-0.03
0
0.0003
0.0006
0.0009
0.0012

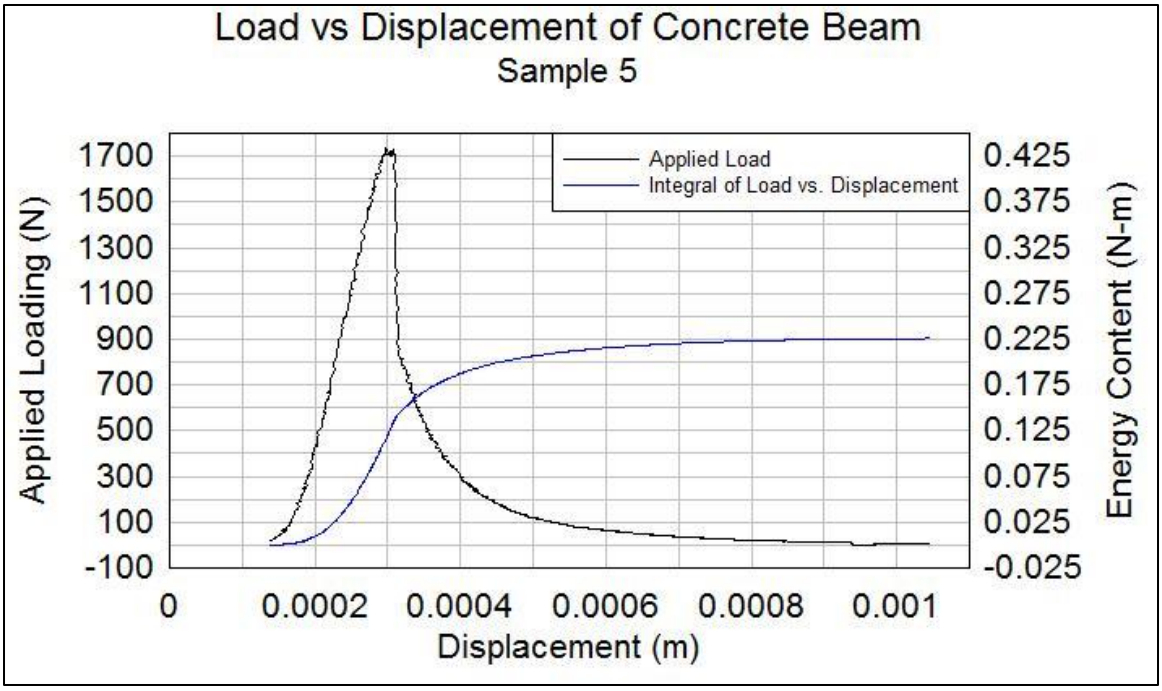
Load vs Displacement of Concrete Beam
Sample 5
Applied Load
Integral of Load vs. Displacement
Applied Loading (N)
Energy Content (N-m)
Displacement (m)
1700
1500
1300
1100
900
700
500
300
100
-100
0.425
0.375
0.325
0.275
0.225
0.175
0.125
0.075
0.025
-0.025
0
0.0002
0.0004
0.0006
0.0008
0.001

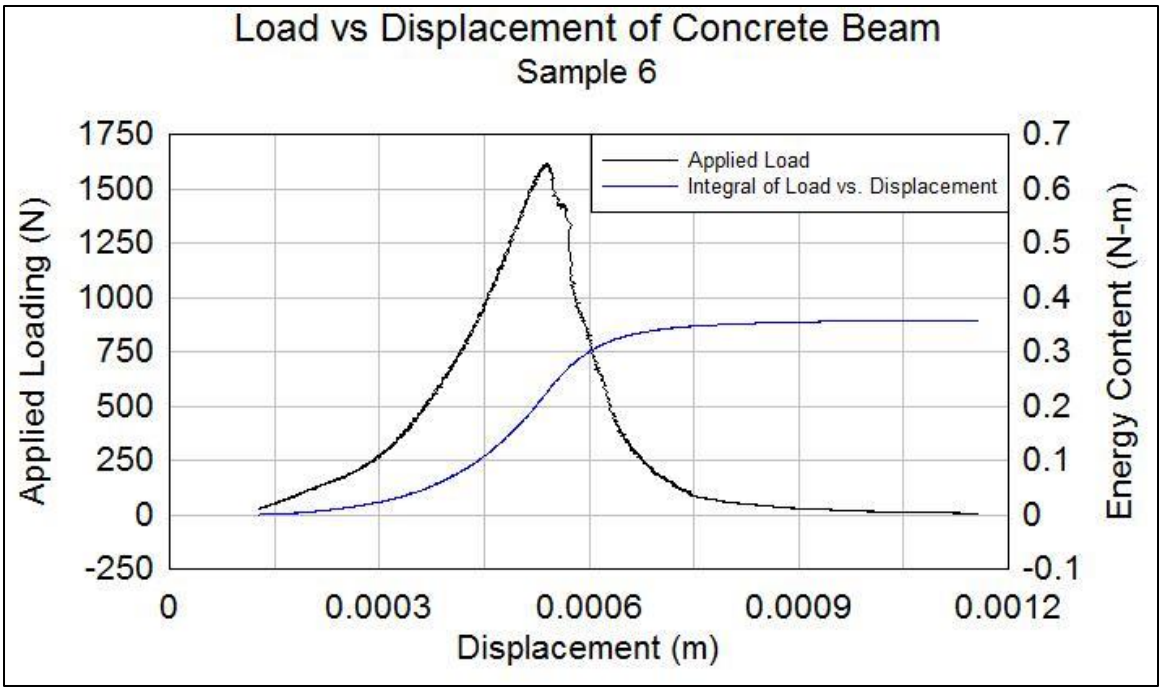
Load vs Displacement of Concrete Beam
Sample 6
Applied Load
Integral of Load vs. Displacement
Applied Loading (N)
Energy Content (N-m)
Displacement (m)
1750
1500
1250
1000
750
500
250
0
-250
0.7
0.6
0.5
0.4
0.3
0.2
0.1
0
-0.1
0
0.0003
0.0006
0.0009
0.0012

Bibliography

Abdalla, H., & Karihaloo, B. (2003). Determination of size-independent specific fracture energy of concrete from three-point bend and wedge splitting tests. *Magazine of Concrete Research*, 133-141.

Adel, G., Smith, B., Kojovic, T., Thornton, D., & Richardson, J. M. (2005). Mine-to-Mill Optimization of Aggregate Production. *2005 SME Annual Meeting.* Salt Lake City, UT: SME.

Adel, G., Smith, B., Kojovic, T., Thornton, D., & Richardson, J. M. (2006). Application of Mine-to-Mill Optimization to the Aggregate Industry. *2006 SME Annual Meeting.* St. Louis, MO: SME.

Albach, H. (1967). Long Range Planning in Open-Pit Mining. *Management Science*, B549-568.

Amador, F., & Romero, C. (1989). Redundancy in lexicographical goal programming: An emperical approach. *European Journal of Operational Research*, 347-354.

ASTM International. (2002). C 293 - 02 Standard Test Method for Flexural Strength of Concrete (Using Simple Beam with Center-Point Loading).

Atasoy, Y., Valery, W., & Skalski, A. (2001). Primary Versus Secondary Crushing at St. Ives (WMC) SAG Mill Circuit. *SAG 2001* (pp. 248-261). Vancouver, Canada: University of British Columbia.

Berta, G. L. (1990). L'esplosivo strumento di lavoro. *Italesplosivi*, 31-64.

Blasting Analysis International. (2001). *Motion Tracker 2D Program User's Manual.* Allentown, Pennsylvania: Blasting Analysis International.

Bronson, R., & Naadimuthu, G. (1997). *Schuam's Outline of Theory and Problems of Operations Research* (2nd ed.). New York: McGraw-Hill.

Buczkowski, D., & Zygmunt, B. (2011). Detonation Properties of Mixtures of Ammonium Nitrate Based Fertilizers and Fuels. *Central European Journal of Energetic Materials*, 99-106.

Charnes, A., & Cooper, W. W. (1961). *Management Models and Industrial Applications of Linear Programming.* New York: Wiley.

Charnes, A., & Cooper, W. W. (1977). Goal programming and multiple objective optimizations. *European Journal of Operational Research*, 39-54.

Charnes, A., Cooper, W. W., & Furguson, R. (1955). Optimal estimation of executive compensation by linear programming. *Management Science*, 138-151.

Cunningham, C. (1991). *The assessment of detonation codes for blast engineering.* San Diego, CA: International Society of Explosives Engineers.

Cunningham, C. (2001). The Energy of Detonation: A Fresh Look at Pressure in the Blasthole. *Proceedings EXPLO 2001* (pp. 105-110). Melbourne: The Australasian Institute of Mining and Metallurgy.

Cunningham, C. (2003). Breakthrough in the portrayal of explosive energy. *International Society of Explosives Engineers*.

Cunningham, C. (2005). The Kuz-Ram fragmentation model - 20 years on. *Brighton Conference Proceedings, R. Holmber et al* (pp. 201-210). European Federation of Explosives Engineers.

Cunningham, C. (2006). Blasthole Pressure: What it really means and how we should use it. *Journal of Explosives Engineering*.

Cunningham, C., & Szendrei, T. (2004). Cavity expansion by hypervelocity impact applied to blasthole expansion by detonation. *Journal of Explosives Engineering*.

Cunningham, C., Sellers, E., & Szendrei, T. (2007). Cavity expansion energy applied to rock blasting. *Vienna Conference Proceedings* (pp. 27-38). European Federation of Explosvies Engineers.

Flavell, R. B. (1976). A new goal programming formulation. *Omega*, 731-732.

Gershon, M. (1981). *Model Choice in Multiobjective Decision Making in Water and Mineral Resource Systems.* Tucson, Arizona: Dept. of Hydrology and Water Resources, University of Arizona.

Gershon, M. (1982). A Linear Programming Approach to Mine Scheduling Optimization. *17th Application of Computers and Operations Research in the Mineral Industry* (pp. 483-492). Colorado: APCOM.

Gheibie, S., Aghababaei, H., Hoseinie, S. H., & Pourrahimian, Y. (2009). Modified Kuz-Ram fragmentation model and its use at the Sungun Copper Mine. *International Journal of Rock Mechanics and Mining Sciences 46*, 967-973.

Grayson, R. L. (2005). *Mi Eng 403 Lecture Optimization Applications in Mining.* Rolla, Missouri: University of Missouri-Rolla Department of Mining Engineering.

Grundstrom, C., Kanchibotla, S. S., Jankovic, A., & Thornton, D. M. (2001). Blast Fragmentation for Maximizing the SAG Mill Throughput at Porgera Gold Mine. *27th Annual Conference of Explosives and Blasting Techniques* (pp. 383-399). Orlando, FL: ISEE.

Gurney, R. (1943). The Initial Velocities of Fragments from Bombs, Shells, and Grenades. In *BRL Report No. 405.*

Hamdi, E. e. (2008). Fragmentation Energy in Rock Blasting. *Geotech. Geol. Eng.*, 133-146.

Hamdi, E., Mouza, J. d., & Fleurisson, J. A. (2001). Evaluation of the part of blasting energy used for rock mass fragmentation. *Fragblast*, 180-193.

Hannan, E. L. (1980). Nondominance in goal programming. *Canadian Journal of Operation Research and Information Processing*, 300-309.

Hart, S., Valery, W., Clements, B., Reed, M., Song, M., & Dunne, R. (2001). Optimization of the Cadia Hill SAG Mill Circuit. *SAG 2001* (pp. 11-30). Vancouver, Canada: Univeristy of British Columbia.

Hewlett, R. F. (1961). Mathematical Models and Their Application to Production Problems. *1st Computers and Computer Applications in the Mineral Industry* (pp. 1-23). Tuscon, Arizona: APCOM.

Hoffman, J., Lusk, B., & Perry, K. (2009). Investigations of shock tunnel dynamics and energy realization. *Blasting and Fragmentation*, 207-226.

Hoffman, J., Lusk, B., & Perry, K. (2009). Investigations of shock tunnel dynamics and energy realization. *Blasting and Fragmentation*, 207-226.

Hooban, M., & Camozzo, R. (1981). Blending of Coal With a Small Computer. *Coal Age*, 102-104.

Ignizio, J. P. (1976). *Goal Programming and Extensions.* Lexington, MA: Lexington Books.

Johnson, C., Lusk, B., Hoffman, J., & Rathbun, J. (2013). Surface Coal Mine Blasting Optimization and Mitigation of Environmental Impacts: Mine to Fill. *Environmental Considerations in Energy Production.* Littleton, CO: SME.

Johnson, T. B. (1969). Optimum Production Scheduling. *8th Internation Symposium on Computers and Operations Research*, (pp. 539-562). Salt Lake City, Utah.

Jordi, K. C., & Currin, D. C. (1979). Goal Programming for Strategic Planning. *16th Application of Computers and Operations Research in the Mineral Industry* (pp. 269-303). Tucson, Arizona: APCOM.

Kanchibotla, S. S., Valery, W., & Morrell, S. (1999). Modeling fines in blast fragmentation and its impact on curshing and grinding. *Proceedings of Explo'99 - A Conference on Rock Breaking* (pp. 137-144). Kalgoorlie, Australia: The Australasian Institute of Mining and Metallurgy.

Karageorgos, J., Skrypniuk, J., Valery, W., & Ovens, G. (2001). SAG Milling at the Fimiston Plant (KCGM). *SAG 2001* (pp. 109-124). Vancouver, Canada: University of British Columbia.

Karihaloo, B., Abdalla, H., & Imjai, T. (2003). A simple method for determining the true specific fracture energy of concrete. *Magazine of Concrete Research*, 471-481.

Kim, Y. C., Knudsen, H. P., & Baafi, E. Y. (1981). Goal Programming for Strategic Planning. *16th Application of Computers and Operations Research in the Mineral Industry* (pp. 269-303). Tuscon, Arizona: APCOM.

Kristiansen, J., Kure, K., Vestre, J., & Bergqvist, I. (1990). An Investigation of Heave and Fragmentation Related to Explosive Properties. *Proceedings FRAGBLAST '90*, (pp. 83-90). Brisbane.

La Rosa, D., & Thornton, D. (2011). Blast Movement Modelling and Measurement. *Proceedings 35th APCOM Symposium* (pp. 297-309). Wollongong, NSW: APCOM.

Lee, S. M. (1972). *Goal Programming for Decision Analysis.* Philidelphia: Auerbach.

Lewis, C. (2008). *Linear Programming: Theory and Application.* Walla Walla, WA: Whitman College Mathematics Department.

Lilly, P. A. (1986). An Emperical Method of Assessing Rock Mass Blastability. *Large Open Pit Mining Conference.* Parkville, Vic: The AusIMM/IE Aust Newman Combined Group.

Lopez, L. M. (2002). On explosive useful work and rock mass fragmentation energy. *Journal of Explosives Engineering*, 175.

Lusk, B. (2011, Fall). Blast Design Basics. In *MNG 331.* Lexington, KY: University of Kentucky Mining Engineering Dept.

Lusk, B. (2014, September). Personal Discussion.

Meyer, M. (1969). Applying Linear Programming to the Design of Ultimate Pit Limits. *Management Science*, B121-135.

Meyer, R. (1987). *Explosives 3rd Edition.* Weinheim, Germany: VCH-Verlag.

Miller, S. J. (2007). *An Introduction to Linear Programming.* Providence, RI: Mathematics Department, Brown University.

Mohanty, B. (1999). Explosives Performance - The Underwater Test Revisited. *Proceedings Explo '99* (pp. 131-137). Kalgoorlie: The Australasian Institute of Mining and Metallurgy.

Nelle, P. B. (1962). Ore Blending and Process Control. *2nd Mathematical Techniques and ComputerApplications in Mining*, (pp. 02-016). Tucson, Arizona.

Nyberg, U., Arvanitidis, I., Olsson, M., & Ouchterlony, F. (2003). Large Size Cylinder Expansion Tests on ANFO and Gassed Bulk Emulsion Explosives. *Proceedings of the Second World Conference on Explosives and Blasting Techniques* (pp. 181-191). Prague: Balkema.

Olsson, M., Nie, S., Bergqvist, I., & Ouchterlony, F. (2001). What Causes Cracks in Rock Blasting. *Proceedings EXPLO 2001* (pp. 191-196). Melbourne: The Australasian Institute of Mining and Metallurgy.

Onederra, I., Esen, S., & Jankovic, A. (2004). Estimation of fines generated by blasting - application for the mininbg and quarrying industries. *Mining Technology*.

Ouchterlony, F. (2004). Where does the explosive energy in rock blasting rounds go? *Lulea University of Technology*.

Ouchterlony, F., Nyberg, U., & Olsson, M. (2003). The Energy Balance of Production Blasts at Norkalk's Klinthagen Quarry. *Proceedings of the Second World Conference on Explosives and Blasting* (pp. 193-203). Prague: Balkema.

Paley, N., & Kojovic, T. (2001). Adjusting blasting to increase SAG mill throughput at the Red Dog mine. *27th ISEE Annual Conference* (pp. 65-80). Orlando, FL: ISEE.

RILEM Committee FMC-50. (1985). Determination of the fracture energy of mortar and concrete by means of the three-point bend tests on notched beams. *Materials and Structures*, 285-290.

Romero, C. (1991). *Handbook of Critical Issues in Goal Programming.* Oxford: Pergamon Press.

Rudenno, V. (1979). Determination of Optimum Cutoff Grades. *16th Application of Computers and Operations Research in the Mineral Industry* (pp. 261-268). Tucson, Arizona: APCOM.

Saharan, M. R., Mitri, H. S., & Jethwa, J. L. (2006). Rock fracturing by explosive energy: review of state-of-the-art. *Fragblast*, 61-81.

Sanchidrian, J. A., & Lopez, L. M. (2006). Calculation of the Energy of Explosives with a Partial Reaction Model. Comparison with Cylinder Test Data. *Propellants, Explosives, Pyrotechnics 31, No.1*, 25-32.

Sanchidrian, J. A., Segarra, P., & Lopez, L. M. (2007). Energy components in rock blasting. *International Journal of Rock Mechanics and Mining Sciences 44*, 130-147.

Sanchidrian, J. A., Segarra, P., & Lopez, L. M. (2007). Energy Components in Rock Blasting. *International Journal of Rock Mechanics & Mining Sciences*, 130-147.

Sanchidrian, J. A., Segarra, P., & Lopez, L. M. (2007). On specific surface and fragmentation energy of blasted rock. *Vienna Conference Proceedings* (pp. 63-73). European Federation of Explosives Engineers.

Sarmiento, D., & Delgado, G. (1979). A Mathematical Model for a Refinery Process - Centromin's Plant of Zinc. *16th Application of Computers and Operations Research in the Mineral Industry* (pp. 261-268). Tucson, Arizona: APCOM.

Satapathy, S., & Bless, S. (1995). *Cavity Expansion Analysis of Brittle Materials.* Austin, TX: Institute for Advanced Technology The University of Texas at Austin.

Satapathy, S., & Bless, S. (2000). Cavity Expansion Resistance of Brittle Materials Obeying a Two-Curve Pressure-Shear Behavior. *Journal of Applied Physics*, 4004-4012.

Schleifer, J., & Tessier, B. (2000). Fragmentation Assessment Using the Fragscan System: Quality of a Blast. *Proceedings of the First World Conference on Explosives and Blasting Technique* (pp. 111-115). Munich: Balkema.

Scilly, N. (1995). Measurement of the Explosive Performance of High Explosives. *Journal of Loss Prevention in the Process Industries*, 265-273.

Sellers, E. e. (2013). What Broke the Burden? Improving our understanding of burden breakout. International Society of Explosives Engineers.

Silva, J. (2015). *Personal Discussion.*

Singh, S. e. (2006). A comparison between seived, predicted and measured blast fragmentation results. *Journal of Explosives Engineering*.

Smith, M., & Hautala, R. (1991). A Coupled Expert System Approach to Blast Optimization and Fragmentation Modeling. *1991 SME Annual Meeting.* Denver, Colorado: SME.

Spathis, A. (2013). Innovations in blast measurement: Reinventing the past. *Rock Fragmentation by Blasting*, 23-39.

Spathis, A. T. (1999). On the energy efficiency of blasting. *Proceedings of the Sixth International Symposium on Rock Fragmentation by Blasting* (pp. 81-90). Johannesburg: The South African Institute of Mining and Metallurgy.

Split Engineering. (2001). *Split-Desktop Software Manual.* Tucson, Arizona: Split Engineering, LLC.

Tamiz, M., & Jones, D. F. (1996). Goal programming and pareto efficiency. *Journal of Information and Optimization Sciences*, 291-307.

Tamiz, M., Jones, D., & Romero, C. (1998). Goal programming for decision making: An overview of the current state-of-the-art. *European Journal of Operation Research*, 569-581.

Udy, L., & Lownds, C. M. (1990). The Partition of Energy in Blasting with Non-Ideal Explosives. *FRAGBLAST*, 37-43.

Valery, W., Morrell, S., Kojovic, T., Kanchibotla, S. S., & Thornton, D. M. (2001). Modeling and Simulation Techniques Applied for Optimization of Mine to Mill Operations and Case Studies. *VI Southern Hemisphere Meeting on Mineral Technology* (pp. 107-116). Rio de Janeiro, Brazil: CETEM/MCT.

Zimmerman, H. J. (1983). Using fuzzy sets in operational research. *European Journal of Operational Research*, 201-206.

Vita

Joshua Thomas Calnan was born in Oneida, New York and moved to Statesville, North Carolina at the age of 13. After finishing high school in 2006, he attended Mitchell Community College (MCC) in Statesville, NC, where he received his Associate of Science degree. During his time at MCC he held two summer internships with the NASA Robotics Academy and was a key member in the foundation of the college's rocketry team. He received his B.S. in Civil Engineering from the University of Kentucky in December 2010 and M.S. in Mining Engineering from the University of Kentucky in May 2013. While in graduate school, he has been a research assistant for Dr. Braden Lusk and a member of the University of Kentucky Explosives Research Team (UKERT). He has been a student member of ISEE and SME since 2011. In addition to his research duties with UKERT, he has been a subject matter expert for the Bureau of Alcohol, Tobacco, Firearms, and Explosives (ATF). He has also co-authored numerous local and international conference papers.

Joshua Thomas Calnan